Development of Diffusion Weighted Magnetic Resonance Acquisition Techniques
for Hyperpolarized Carbon-13 Metabolites and
Applications to Cancer Detection and Characterization

by

Bertram Lorenz Koelsch

DISSERTATION

Submitted in partial satisfaction of the requirements for the degree of

DOCTORATE OF PHILOSOPHY

in

Bioengineering

in the

GRADUATE DIVISION

of the

UNIVERSITY OF CALIFORNIA, SAN FRANCISCO

AND

UNIVERSITY OF CALIFORNIA, BERKELEY

[redacted]

*Daß ich erkenne, was die Welt*
*Im Innersten zusammenhält*

Johann Wolfgang von Goethe

*Faust I*, Verse 382 f.

# Acknowledgments

First and foremost, I would like to graciously acknowledge my dissertation advisor, John Kurhanewicz. Regardless of his busy schedule, John always made time for me, whether it was to chat about the new experimental results or about the bigger picture story. John also took great care to ensure my professional development, sending me to present at multiple conferences that often were on the other side of the globe. Thanks to you, John, I have grown immensely as a scientist and engineer these past years.

Next, I would like to thank the others in the Kurhanewicz Lab...

Kayvan Keshari, the postdoc in the lab during my first several years, spent countless days teaching me about NMR, dissolution DNP and bioreactors.

Renuka Sriram, for the great times troubleshooting bioreactor experiments together, for your support in diffusion experiments and for chatting about anything and everything over lunch.

Mark Van Criekinge taught me about the inner workings of the NMR spectrometers and the polarizers. The same goes for the bioreactors. Without him, the infrastructure to do these experiments would not exist. It was a pleasure listening to stories from your days traveling the world for Varian.

Lynn DeLosSantos is the cornerstone of the lab. Without her, the Kurhanewicz lab wouldn't be fully functional. I am thankful for her unwavering willingness to help with anything, at any time.

Subramaniam Sukumar taught me everything I know about pulse programming on the Varian magnets.

Bob Bok always was available to explain the intricacies cancer biology to me.

Vickie Zhang, my fellow graduate student in John's lab. We trotted this path together.

Barbara Green, for always sharing a smile and helping out.

The seamless integration of John and Dan Vigernon's labs made the experience even greater...

Dan Vigneron made sure there was enough time on the 3T scanner for our ADC mapping projects to progress.

I want to particularly thank Galen Reed. The flurry of late night experiments with you on the 3T scanner before it went out of commission were some of my most enjoyable and successful. Here's to coffee breaks at Front, dinner at Hard Knox and travels throughout the world, where discussions about science and life flowed freely.

Peder Larson, thank you for always making time to chat when I had questions, whether it was about the details of a simulation, an imaging experiment or about how to present a concept in a paper.

Christine Leon Swisher's drive and inquisitive approach were contagious. Thank you for your eagerness to help out.

Cornelius von Morze, for helped with questions about imaging or preps for the polarizers. You were a great roommate and travel companion at the many ISMRM meetings.

Other faculty members also played an important role in my dissertation work...

Jane Wang was directly involved with all projects relating to renal cell carcinoma, and more broadly provided excellent feedback for all projects in this dissertation.

Dave Wilson answered any questions related to the chemistry of the polarizer preps.

Steve Conolly provided a much appreciated outside perspective, whether related to the projects in this dissertation or career decisions.

We had several European students rotate through the Kurhanewicz Lab...

Debbie Hill and I shared many laughs during her short stay in the lab.

Tom Peeters put much time and effort into helping with the early diffusion projects. It was a pleasure sailing with you and grabbing beers.

I got to practice my Swedish a bit with Ailin Hansen, who visited us from Trondheim, Norway. I appreciate your help with cell culture during my last few months in the lab.

The younger generations of graduate students in the lab challenged me by asking great questions about how things worked. I wish you – Dave Korenchan, Jessie Lee, Hong Shang, Hsin-Yu Chen, Eugene Milshteyn – all the best with your dissertation work.

SarahJane Taylor also deserves a heartfelt acknowledgement. She always had time to answer various administrative questions and made sure I was on path to graduating.

There were many others at UC Berkeley and UCSF who contributed to this work in their own way – and for this I'm grateful.

Outside of the lab, I would like to thank my family for their continued support over these years. My father and I had great chats on the phone during my morning commutes with the F bus over the Bay Bridge. My mother supplied me with heartfelt care packages and always provided words of encouragement. My brother Tilman called often to check-in and, being a radiologist himself, is the only person in my family who was able to really appreciate the details of my dissertation work.

Last, but also first if you count from the bottom up, I would like to thank my newly wedded wife, Lina Nilsson. Having completed her PhD in 2007, her help in maneuvering through my PhD work these past years has been invaluable, from joyous times after accepted papers to frustrating times after late nights in the lab with failed experiments. For your support, I acknowledge you with an unofficial, honorary doctorate, Frau Dr. "Dr." Nilsson.

# Abstract

Development of Diffusion Weighted Magnetic Resonance Acquisition Techniques
for Hyperpolarized Carbon-13 Metabolites and
Applications to Cancer Detection and Characterization

*by*

*Bertram Lorenz Koelsch*

Hyperpolarized $^{13}$C magnetic resonance (MR) is a molecular imaging technique that allows for real-time measurements of *in vivo* metabolism. Exploiting one of the hallmarks of cancer, an increased glycolytic metabolism, hyperpolarized $^{13}$C pyruvate can be used to better characterize cancer aggressiveness and response to therapy by monitoring the production of hyperpolarized $^{13}$C lactate. In the work described herein, we look to not only measure the overall production of hyperpolarized $^{13}$C lactate, but also measure its extra- and intracellular distribution. Understanding this distribution elucidates a second cancer hallmark, the acidification of the extracellular space. This process, in which protons are co-transported out of cytoplasm with lactate, is characteristic of aggressive, metastatic cancers. Thus, measuring the production and the distribution of hyperpolarized $^{13}$C lactate may allow for the differentiation of benign and metastatic cancers.

We present bioreactor studies of two renal cell carcinoma (RCC) cell lines that show the efflux of hyperpolarized $^{13}$C lactate play a significant role in the acquired signal and thus cannot be ignored. To study this distribution, we use a diffusion weighted pulsed gradient double spin echo sequence and a novel acquisition scheme for hyperpolarized $^{13}$C metabolites. Given the highly dynamic signal changes characteristic of hyperpolarized $^{13}$C, we first verify the quantitative accuracy of the technique by measuring the diffusion coefficients of various hyperpolarized $^{13}$C molecules in solution. Next, equipped with this technique, we measured the extra- and intracellular diffusion coefficients of various hyperpolarized $^{13}$C metabolites in bioreactor studies with the same two RCC cell lines. We also assess the dynamic extra- and intracellular distribution of these hyperpolairzed $^{13}$C metabolites in these cells and show that an inhibitor of the monocarboxylate transporter 4 (MCT4), which is responsible for the efflux of lactate and protons from the cytoplasm, increases the relative intracellular hyperpolarized $^{13}$C lactate signal. Finally, we develop a methodology for diffusion weighted imaging and making apparent diffusion coefficient (ADC) maps of hyperpolarized $^{13}$C metabolites on a clinical MR scanner. Using two novel acquisition techniques, we improve the accuracy and precision of these measurements. The work presented here will play an important role in assessing the tissue distribution of hyperpolarized $^{13}$C metabolites, which will aid in the detection and characterization of cancer.

# Contents

# List of Figures

# List of Tables

# Chapter 1

# Introduction

Magnetic resonance imaging (MRI) plays a key role in modern medical imaging. It is the technique's unique ability to generate a wide array of different contrasts that make it unmatched in studying the body, both in its healthy and diseased state. While the discovery of MRI dates back to the 1970s and its broad clinical implementation began in the 1980s, the continued growth of MRI research today, developing techniques such as that presented in this dissertation, confirms the prominent place MRI holds amongst other medical imaging modalities.

Oncology is one area in which MRI provides a variety of specialized techniques to diagnose, characterize and monitor tumors. In its most basic implementation, MRI images highlight tumors by exploiting differences in the tissue-dependent relaxation rates ($T_1$ and $T_2$) of water protons. Magnetic resonance spectroscopic imaging (MRSI) measures local metabolites concentrations, where deviations from "normal" can be used to characterize disease aggressiveness. Diffusion weighted imaging (DWI) scans are sensitive to molecular motion and are most commonly implemented to measure changes in the diffusion coefficients of water that arise due to pathologic changes of the tissue microstructure. While protons are mostly observed in these studies, other magnetically sensitive nuclei, such as $^{13}$C, $^{31}$P and $^{15}$N, can also be used for many of these techniques and provide additional information. Hyperpolarization is a technique that increases the polarization of these nuclei by several orders of magnitude, in turn also increasing the MR signal, and thereby allows for measurements that previously would have been time consuming or impossible.

The work presented in this dissertation is based on a combination of the aforementioned MR techniques. In doing so, we develop techniques for diffusion weighting of hyperpolarized $^{13}$C metabolites in order to study their tissue localization, as determined by their extra- and intracellular distribution, and how this changes with disease. In regards to tumors, these techniques may provide a means for distinguishing aggressive, metastatic from localized, indolent tumors.

The first part of this dissertation, Chapters 2 and 3, provide a technical background. The intention of this chapter is to provide the reader with enough technical information to understand the novel advances made in this dissertation, and not to serve as a comprehensive review of these topics. Chapter 2 introduces the principles of MR and extends this discussion to hyperpolarized $^{13}$C MR. Next, we present a section on the fundamentals of diffusion and their relation to diffusion weighted MR. Chapter 3 discusses the hallmarks of cancer and focuses on those that are important for hyperpolarized $^{13}$C studies, namely increased glycolitic rate and the acidification of the extracellular space.

In Chapter 4, we investigate the dynamic metabolic flux in living renal cell carcinoma (RCC) cells of hyperpolarized $^{13}$C pyruvate to hyperpolarized $^{13}$C lactate within a bioreactor platform, a perfusion system. In agreement with prior studies, we show that RCC cells have significantly higher pyruvate-to-lactate flux than the normal renal tubule cells. Interestingly, we also show that the metastatic RCC cells have significantly higher lactate efflux as a result of their higher expression of the monocarboxylate transporter 4 (MCT4). A key feature distinguishing the localized from the metastatic RCC cells is the overexpression of MCT4, which is essential for maintaining a high rate of glycolysis. Ultimately, these studies show that such differential cellular transporter expression and associated metabolic phenotype can be noninvasively assessed via real-time monitoring of hyperpolarized $^{13}$C pyruvate-to-lactate flux. Given this, these findings motivate the development of diffusion weighted techniques for hyperpolarized $^{13}$C metabolites and thereby characterizing cancers not only with flux measurements, but also an understanding of the extra- and intracellular distribution of these hyperpolarized $^{13}$C metabolites.

Chapter 5 lays the foundation of diffusion weighted acquisition techniques of hyperpolarized $^{13}$C molecules. We use a pulsed gradient double spin echo diffusion MR sequence to rapidly and accurately measure the diffusion coefficients of various hyperpolarized $^{13}$C molecules in solution. While hyperpolarized experiments can measure rapid, non-equilibrium processes by avoiding signal averaging, continuous signal loss due to longitudinal relaxation ($T_1$) complicates quantification. By correcting for this signal loss, we demonstrate the feasibility of using hyperpolarized $^{13}$C diffusion weighted MR to accurately measure real-time (seconds) molecular transport phenomena, such as diffusion. We also demonstrate the ability to generate apparent diffusion coefficient (ADC) maps of multiple hyperpolarized metabolites simultaneously using diffusion weighted imaging.

In Chapter 6 we use diffusion weighting to completely separate the extra- and intracelluar hyperpolarized $^{13}$C metabolite signals. Using this, we can both measure the intracellular diffusion coefficients of these hyperpolarized $^{13}$C metabolites and dynamically assess the real-time changes in the extra- and intracellular pools of these hyperpolarized $^{13}$C metabolites. Studies with the highly aggressive, metastatic RCC cell line with overexpressed MCT4 show clearly that these cells rapidly transport the hyperpolarized $^{13}$C out of the cells. Inhibition of MCT4 with a small molecule inhibitor shows both a decrease in the hyperpolarized

$^{13}$C pyruvate to lactate flux and a increase in the relative intracellular hyperpolarized $^{13}$C lactate. Considering that these MCT4s are cotransporters with protons that acidify the extracellular space, diffusion weighting of hyperpolarized $^{13}$C metabolites could facilitate with differentiating between indolent and metastatic tumors.

Finally, Chapter 7 presents an acquisition methodology that enables diffusion weighted imaging and ADC mapping of hyperpolarized $^{13}$C metabolites on a clinical MRI scanner. Briefly, a bipolar pulsed gradient double spin echo sequence can achieve sufficiently high diffusion weightings with the limited maximum gradient amplitudes of a clinical MRI. Acquisition techniques are presented to improve both the accuracy and precision of these ADC measurements. These ADC maps can be used by future studies to investigate the tissue microenvironemnts in which hyperpolarized $^{13}$C metabolite reside, where for tumors changes in the ADC of hyperpolarized $^{13}$C lactate may facilitate in characterizing its metastatic potential. Ultimately, the goal of the work presented in this chapter will facilitate the clinical translation of the DW techniques for hyperpolarized $^{13}$C metabolites.

Chapter 8 summarizes the work presented in this dissertation and provides a future outlook on further developments diffusion weighting of hyperpolarized $^{13}$C metabolites and their ability to aid in tumor characterization.

# Chapter 2

# Technical Background: Magnetic Resonance and Diffusion

## 2.1 Chapter Overview

Nuclear magnetic resonance (NMR) is a powerful analytical tool that has been used for significant advances in the fields of physics, chemistry and biology. Isidor Rabi's 1938 publication described the first NMR measurements using radio frequency pulses applied as weak oscillating magnetic fields close to the Larmor frequency of LiCl molecules in a molecular beam [Rabi *et al.*, 1938]. In 1946, Felix Bloch and Edward Purcell independently described NMR experiments in bulk liquid and solid samples [Bloch, 1946; Purcell *et al.*, 1946]. These experiments became the foundation for modern NMR and magnetic resonance imaging (MRI) experiments [Lauterbur, 1973]. With Edward Hahn's 1950 description of the spin-echo, it was immediately recognized that self-diffusion measurements could be made using the technique [Hahn, 1950]. The pulsed gradient spin echo experiments by Stejskal and Tanner in 1965 greatly improved the sensitivity of diffusion MR experiments [Stejskal and

Tanner, 1965], which had been using static gradients. A few years later, Stejskal and Tanner used their technique to measure both extracellular and intracellular diffusion coefficients and found a correlation between diffusion coefficients and tissue structure [Tanner and Stejskal, 1968]. In the mid 1980s, Denis Le Bihan published the first diffusion weighted magnetic resonance imaging (DWI) results in the brain, showing differences in water's apparent diffusion coefficients (ADCs) between normal and pathologic tissues [Le Bihan *et al.*, 1986]. Since these initial *in vivo* diffusion weighted imaging measurements, clinical oncology has embraced DWI to detect and characterize tumors, initially in the brain [Le Bihan *et al.*, 1986] but now also for cancers within the body [Koh *et al.*, 2007].

In this chapter, we discuss the concepts essential for understanding the scientific work presented in later in this dissertation. We begin with an overview of the fundamental concepts of MR and extend these concepts to understand hyperpolarized $^{13}$C MR. Next, we review the essential concepts of diffusion, followed by an overview of diffusion weighted MR.

## 2.2 Nuclear Magnetic Resonance

Fundamentally, the NMR experiment is made possible by the quantum mechanical property "spin," which is a form of angular momentum that all elementary particles have. Protons and neutrons are composed of a various elementary particle and so they too have spin. When an atomic nucleus is composed of an odd number of protons and/or neutrons they posses spin. Most NMR experiments only use spin-1/2 nuclei, such as $^{1}$H, $^{13}$C, and $^{31}$P. Also inherent to non-zero spin nuclei is a magnetic dipole moment. The ratio of the magnetic dipole moment to the angular momentum for a nucleus is defined as its gyromagnetic ratio ($\gamma$).

Nuclear Zeeman splitting occurs upon the application of an external magnetic field to nuclei with non-zero spin, where for spin-1/2 nuclei the ground state splits into two sublevels.

Table 2.1: A selection spin-1/2 particles and their gyromagnetic ratios

| Isotope | Natural abundance [%] | Gyromagnetic ratio $\gamma/2\pi$ [MHz T$^{-1}$] | NMR frequency at 3 T $\omega_0/2\pi$ [MHz] |
|---|---|---|---|
| $e^-$ | – | $2.8024\times10^4$ | $8.4060\times10^4$ |
| $^1$H | 100 | 42.576 | 127.728 |
| $^{13}$C | 1.1 | 10.705 | 32.115 |
| $^{31}$P | 100 | 17.235 | 51.705 |
| $^{15}$N | 0.37 | -4.316 | 12.948 |

The energy difference between these two sublevels is given by

$$E = -\mu \cdot \mathbf{B} \tag{2.1}$$

where $\mu$ is the magnetic dipole moment of a spin and $\mathbf{B}$ is the magnetic field vector. For a spin-1/2 nuclei, this can be rewritten as

$$\Delta E = -\hbar\,\gamma\,B_0 = -\hbar\,\omega_0 \tag{2.2}$$

where $\hbar$ is Planck's constant (J s$^{-1}$ rad$^{-1}$), $\gamma$ is the gyromagnetic ratio for a nucleus (rad s$^{-1}$ T$^{-1}$) and $B_0$ is the magnetic field (T) along the z-axis, as is normal convention in MR. The angular frequency $\omega_0$ (rad s$^{-1}$) of the nuclear spin about the magnetic field is known as the Larmor frequency:

$$\omega_0 = \gamma\,B_0 \tag{2.3}$$

MR experiments are performed on large populations of spins. In the external magnetic field, each of these spins will align either parallel ("up" or $N_+$) or antiparallel ("down" or $N_-$)

with $B_0$. The ratio of spins between these populations follows the Boltzmann distribution:

$$\frac{N_-}{N_+} = \exp\left(\frac{-\Delta E}{k_b\,T}\right) = \exp\left(\frac{-\hbar\,\gamma\,B_0}{k_b\,T}\right) \tag{2.4}$$

where $k_b$ is Boltzmanns constant (J $K^{-1}$) and T is the absolute temperature (K). The polarization (P) for population of spins is defined as

$$P = \left|\frac{N_+ \; - \; N_-}{N_+ \; + \; N_-}\right| \tag{2.5}$$

Combining equations 2.4 and 2.5, gives

$$P = \frac{\exp\left(\frac{-\hbar\,\gamma\,B_0}{k_b\,T}\right) - 1}{\exp\left(\frac{-\hbar\,\gamma\,B_0}{k_b\,T}\right) + 1} = \tanh\left(\frac{-\hbar\,\gamma\,B_0}{2\,k_b\,T}\right) \tag{2.6}$$

The polarization, or difference between the "up" ($N_+$) and "down" ($N_+$) energy levels, at thermal equilibrium is very small. Nevertheless, this small population difference forms the net magnetization that becomes our NMR signal. For example, for protons at body temperature (310 K) and in a 3 T magnet, the thermal equilibrium polarization is merely $9.9 \times 10^{-6}$. Conveniently, the concentration of water in the body is about 55 M, producing enough signal for $^1$H MRI. Yet, for nuclei with lower gyromagnetic ratios whose thermal equilibrium polarizations are smaller and often their natural abundance is lower (see Table 2.1), MR experiments require time-intensive signal averaging that becomes tedious or impossible. For example, for $^{13}$C, which is at 1.1% natural abundance, the thermal equilibrium polarization under the same conditions is merely $2.5 \times 10^{-6}$.

## 2.3 Dynamic Nulcear Polarization

Given that the thermal equilibrium polarization is on the order of $10^{-6}$, much effort has been focused on increasing MR signal, which is proportional to polarization and concentration of the nuclei under study. The most straightforward ways to enhance the MR signal are to either increase the concentration of the compound under study or, as equation 2.6 shows, use a stronger magnet to increase the thermal equilibrium polarization of the nuclei. Accordingly, state-of-the-art NMR spectrometers have reached fields upwards of 20 T while human MRI scanners have reached 9.4 T! Yet, these are merely incremental improvements at very high costs. Luckily, other techniques are also available that provide nuclear polarizations much greater than those achievable at thermal equilibrium.

In 1953, Albert Overhauser proposed a technique that would enhance the nuclear polarization by several orders of magnitude [Overhauser, 1953]. Later that same year, Charles Slichter experimentally validated the technique [Carver and Slichter, 1953]. Now known as dynamic nuclear polarization (DNP), this process enhances nuclear polarization by transferring the polarization from surrounding unpaired electrons, which themselves polarize more readily than nuclei (Table 2.1). Generally done in the solid state at very low temperatures (e.g., 1 K), a microwave source oscillated at the specific frequency, such that $\omega = \omega_e \pm \omega_n$, transfers the electron polarization to the surrounding nuclei. Today, solid state DNP is commonly used for measurements in structural biology.

As an aside, DNP is not the only technique used to generate polarizations greater than those allowed by the Boltzmann distribution. Other techniques include spin-exchange optical pumping (SEOP) of $^3$He and $^{129}$Xe gas [Möller *et al.*, 2002], para-hydrogen induced polarization (PHIP) [Golman *et al.*, 2001] and chemically induced dynamic nuclear polarization (CIDNP) [Kurhanewicz and Jurch, 1987].

With the development of dissolution DNP in the early 2000s [Ardenkjær-Larsen *et al.*, 2003], the polarization enhancements of solid state DNP became accessible for biomedical applications, both in research and clinical settings. Using DNP, the polarization of $^{13}$C nuclei are increased by greater than $10^4$ over that of thermally polarized $^{13}$C at physiologic temperatures. After about one hour in the polarizer, the $^{13}$C molecules are transferred into the liquid state by injection of a super heated solvent (190°C and 10 bar) that results in a final solution temperature of  37°C. The use of molecules with $^{13}$C carbonyls is deliberate since these have sufficiently long $T_1$s to monitor real time metabolism *in vivo* [Golman *et al.*, 2006]. This technique forms the basis of the work presented in this dissertation.

## 2.4 Bloch Equations

MR experiments observe the net magnetization produced from a large population of spins, referred to as the "bulk" magnetization. This bulk magnetization $\mathbf{M}$ comes from the summation of all magnetic moments $\mu$ in the sample that align with $\mathbf{B}$. When perturbed, this bulk magnetization begins to process about $\mathbf{B}$, as described by

$$\frac{d\mathbf{M}}{dt} = \mathbf{M} \times \gamma\mathbf{B} \tag{2.7}$$

This equation has the same form as that describing a gyroscope in a gravitational field. Thus, the MR experiment is often conceptually described as the procession of $\mathbf{M}$ (gyroscope) about $\mathbf{B}$ (gravity). To simplify matters, we can split $\mathbf{M}$ into its components: $M_z$, or the longitudinal magnetization, is parallel to $B_0$ along the $z$-axis, while $M_{xy}$, or the transverse magnetization, is in the $xy$-plane.

In addition to the procession of these molecules, two other dynamic processes are generally discussed when describing MR. The first is longitudinal relaxation or $T_1$. The equilibrium magnetization along the $+z$-axis is described as $M_0$. After tipping some portion of this magnetization away from the $z$-axis, $M_z$ will be smaller than $M_0$, but recovers exponentially back to $M_0$ according to

$$\frac{dM_z}{dt} = -\frac{M_z - M_0}{T_1} \tag{2.8}$$

for which the general solution is

$$M_z = M_0 + \left(M_z\left(0\right) - M_0\right)\, \exp\left(-t/T_1\right) \tag{2.9}$$

and after completely tipping $M_z$ into the transverse plane, $M_z(0) = 0$, this becomes

$$M_z = M_0\, \left(1 - \exp\left(-t/T_1\right)\right) \tag{2.10}$$

$T_1$ relaxation is the spin-lattice time constant characterized by the return of $M_z$ back to the equilibrium $M_0$. The physical properties determining $T_1$ are complex. Briefly, $T_1$ is influenced by the position of the nucleus within a molecule (i.e., its chemical environment), the strength of the external magnetic field and the presence of any paramagnetic materials. For protons, *in vivo* $T_1$s range from 0.1 – 1 s. The $T_1$s for most of the $^{13}C$ nuclei used in hyperpolarized experiments range from 10 – 60 s, where *in vivo* $T_1$s are shorter than those in solution.

The other dominant relaxation process in MR is transverse or $T_2$ relaxation. This relaxation process, also called spin-spin relaxation, can be best thought of as destructive interference. After being tipped into the transverse plane, the individual magnetization vectors from each of the spins comprising the bulk $M_{xy}$ magnetization vector will lose phase coherence as they rotate at slightly different frequencies. Over time, this will reduce the magnitude of $M_{xy}$. $T_2$ is the time-constant that describes the decay of $M_{xy}$, according to

$$\frac{dM_{xy}}{dt} = -\frac{M_{xy}}{T_2} \tag{2.11}$$

to which the solution after completely tipping $M_z$ into the transverse plane, $M_{xy}(0) = M_0$, is

$$M_{xy} = M_0 \, \exp\left(-t/T_2\right) \tag{2.12}$$

As for $T_1$, $T_2$ relaxation is determined by a variety of physical processes, including magnetic field inhomogeneities and restricted molecular movement as dictated by the viscosity of the surrounding environment.

Noteworthy is that when measuring the $T_1$s of hyperpolarized $^{13}$C nuclei, the response does not look like typical $T_1$ relaxation, as defined by equation 2.10. Rather, the measurements behave like $T_2$ relaxation, as defined by equation 2.12. The reason for this difference in the behavior of thermally polarized and hyperpolarized nuclei is the directionality of the relaxation back to the thermal equilibrium magnetization $M_0$. In the case of thermally polarized spins, $M_z$ grows back to $M_0$. Yet, for hyperpolarized spins, $M_z$ is initially much greater than the thermal polarization $M_0$, but over time this excess polarization is lost as $M_z$ approaches $M_0$.

Combining equations 2.7, 2.8 and 2.11, the nuclear magnetization ($\mathbf{M} = [M_x,\, M_y,\, M_z]$) can be described as a function of time in the presence of $T_1$ and $T_2$ relaxation. These form the Bloch equation:

$$\frac{d\mathbf{M}}{dt} = \mathbf{M} \times \gamma\mathbf{B} - \frac{M_x\mathbf{i} + M_y\mathbf{j}}{T_2} - \frac{(M_z - M_0)\,\mathbf{k}}{T_1} \tag{2.13}$$

where $\mathbf{i}$, $\mathbf{j}$ and $\mathbf{k}$ are the unit vectors in the laboratory frame of reference. As previously mentioned, the cross-product describes the processional behavior of the magnetization while both of the relaxation terms describe the exponential behavior of the longitudinal and transverse magnetizations. The Bloch equation can be modified to include the description of other physical processes that affect the bulk magnetization $\mathbf{M}$, as we will see below with diffusion.

## 2.5 Imaging in k-space

To create images with MR, we need to spatially encode the signals. Generally, linear magnetic field gradients are used to slightly alter the local magnetic field. Thus, the Larmor frequency is now location-dependent, according to

$$\omega(\mathbf{r}) = \omega_0 + \Delta\omega(\mathbf{r}) = \gamma B_0 + \gamma \mathbf{G} \cdot \mathbf{r} \tag{2.14}$$

Since in MR, we only measure the transverse ($M_{xy}$) signal *S(t)*, the Bloch equation after a 90° excitation pulse can be written as

$$S(t) = \exp(-i\omega_0 t) \int M(\mathbf{r}) \, \exp(-t/T_2(\mathbf{r})) \, \exp\left(-i\gamma \int_0^t \mathbf{G}(\tau) \cdot \mathbf{r} d\tau\right) \, d^3\mathbf{r} \tag{2.15}$$

Ignoring $T_2$ relaxation, this expression is the spatial Fourier transform of $M(\mathbf{r})$, with

$$\mathbf{k}(t) = \frac{\gamma}{2\pi} \int_0^t \mathbf{G}(\tau) d\tau \tag{2.16}$$

Thus, gradients are used to trace-out the $k$-space image and reconstruction is achieved with a simple Fourier transform.

For a more detailed discussion of MR, relaxation phenomena and DNP, the reader is directed to textbooks on these subjects [Levitt, 2008; Slichter, 1990].

## 2.6 Diffusion Essentials

The term diffusion is rather imprecise since it is often used to describe a variety of transport phenomena. In describing molecular motion, the term diffusion can describe self-diffusion and multicomponent diffusion. Flow is the net movement of molecular species, and while diffusion is always present, the influence of flow on the rate of dispersion will outweigh that of diffusion. Each of these processes describes the physical displacement of molecules over time and has the same unit, $\mathrm{mm}^2\ \mathrm{s}^{-1}$.

### 2.6.1 Brownian Motion and the Stokes-Einstein Equation

Brownian motion is the process of self-diffusion, where the stochastic movement of a molecule results from the system's thermal energy. In the strictest sense, self-diffusion is the motion of a molecule within a pure liquid at thermal equilibrium. But, the process describing the movement of a uniformly distributed solute within a solvent, known as tracer diffusion, is fundamentally the same. Einstein defined the diffusion coefficient $D$ of a species to depend both on mobility of the molecule and on the thermal energy of the system:

$$D = \frac{k_b T}{f} \tag{2.17}$$

where $k_b$ is Boltzmann's constant, $T$ is the absolute temperature, and $f$ is the friction factor describing the molecules mobility. The Stokes' relation further defines $f$ as

$$f = 6\pi\eta r \tag{2.18}$$

where $\eta$ is the solvent viscosity (Pa s) and $r$ is the effective hydrodynamic radius of the molecular species (i.e., Stokes radius), assumed to be spherical. Combining equations 2.17 and 2.18, we get the Stokes-Einstein equation for translational diffusion [Einstein, 1956]

$$D = \frac{k_b T}{6\pi\eta r} \tag{2.19}$$

Thus, we can see the $D$ increases with increasing temperatures, but decreases with increasing viscous environments and larger molecular sizes. Note that the form of $f$ here is for a sphere, while $f$ can also assume other forms to define other geometries [Bird *et al.*, 2002].

While Brownian diffusion refers to random thermal motion, this phenomena can be thought of as arising from local microscopic concentration gradients. Thus, Fick's Laws, as discussed in Section 2.6.2, can be used not only to describe diffusive motion due to bulk macroscopic concentrations gradients, but also self-diffusion.

### 2.6.2 Fick's Laws of Diffusion

Mutual diffusion or translational diffusion describes the mass flux of a species due to an inhomogeneous distribution. In this situation, molecular species will travel from an area of high concentration to an area of low concentration. This phenomena is described spatially with Fick's first law of diffusion, here written in one dimension,

$$J_x = -D\frac{\partial n}{\partial x} \tag{2.20}$$

or for three dimensions

$$\mathbf{J} = -D\nabla n \tag{2.21}$$

where $J_x$ and $\mathbf{J}$ are the diffusion flux (mol mm$^{-2}$ s$^{-1}$) and $n$ is the concentration of the species (mol mm$^{-3}$).

Fick's second law of diffusion describes the process as function of time, for one dimension

$$\frac{\partial n}{\partial t} = D\frac{\partial^2 n}{\partial x^2} \tag{2.22}$$

or in three dimensions for an isotropic distribution of $D$

$$\frac{\partial n}{\partial t} = D\nabla^2 n \tag{2.23}$$

It is also common to describe diffusion with the diffusion propagator $P(\mathbf{r}_0,\ \mathbf{r}_1,\ t)$, which denotes the probability of a particle starting at a position $\mathbf{r}_0$ and moving to position $\mathbf{r}_1$ after some time $t$. Fick's second law of diffusion can be rewritten using $P$

$$\frac{\partial P}{\partial t} = D\nabla^2 P \tag{2.24}$$

Suppose we start at $t = 0$ with a collection of molecules concentrated at a single point, which is idealized by the Dirac delta function. Then, the solution to this diffusion equation is described by

$$P(\mathbf{r}_0, \mathbf{r}_1, t) = \frac{1}{(4\pi DT)^{3/2}}\, exp\left(-\frac{(\mathbf{r}_1 - \mathbf{r}_0)^2}{4Dt}\right) \tag{2.25}$$

which takes the form of a Gaussian distribution. Thus, for unrestricted diffusion in an isotropic medium, over time the molecules will become normally distributed. The Gaussian nature of diffusion shows that

$$\bar{x}^2 = qDt \tag{2.26}$$

where $\bar{x}$ is the mean square displacement for a molecular species in one, two or three dimensions, where $q = 2$, 4 or 6, respectively.

## 2.7 Diffusion in MR

As previously mentioned, with Hahn's 1950 description of the spin-echo [Hahn, 1950] was also the realization that MR was perfectly suited to measure translational motion and noninvasively via the radio field emitted from atomic nuclei within the molecules under study. In general, translational motion is measured with dephasing and rephasing gradient pulses, leading to an attenuation or phase shift of the received signal.

### 2.7.1 Bloch-Torrey Equation

The Bloch equation (equation 2.13) used to describe the time-varying magnetization $\mathbf{M}$, can be amended to include diffusion and flow terms, known as the Bloch-Torrey equation [Torrey, 1956]

$$\frac{\partial \mathbf{M}(\mathbf{r},t)}{\partial t} = \mathbf{M} \times \gamma \mathbf{B}(\mathbf{r},t) - \frac{M_x\mathbf{i} + M_y\mathbf{j}}{T_2} - \frac{(M_z - M_0)\mathbf{k}}{T_1} + \nabla \cdot \mathbf{D} \cdot \nabla \mathbf{M} - \nabla \cdot \mathbf{v}\mathbf{M} \tag{2.27}$$

where the magnetization $\mathbf{M}(\mathbf{r},t)$ now varies both in time and space. Here, $\nabla \cdot \mathbf{D}$ shows the directional variation of the diffusion coefficient. When assumed to be isotropic, the diffusion term can be simplified to $D\nabla^2\mathbf{M}$. The final term describes the directional flow $\mathbf{v}$ of the spins.

Since MR measures the transverse magnetization, the Bloch-Torrey equation can be rewritten as

$$\frac{\partial M_+(\mathbf{r},t)}{\partial t} = -\gamma \mathbf{G} \cdot \mathbf{r} - \frac{M}{T_2} + D\nabla^2 M_+ - \mathbf{v} \cdot M_+ \tag{2.28}$$

where $M_+ = M_x + iM_y$. Making the substitution

$$M_+(\mathbf{r},t) = \Phi(t)\ \exp\left(-i\gamma\mathbf{r} \cdot \int_0^t \mathbf{G}(\tau)d\tau\right)\ \exp\left(\frac{-t}{T_2}\right) \tag{2.29}$$

into equation 2.28, where $\Phi(t)$ is the motion and diffusion induced phase imparted by the gradient pulses. Neglecting $T_2$ relaxation, this yields

$$\Phi(t) = \exp\left[-D\gamma^2 \int_0^t \left(\int_0^{t'} \mathbf{G}(\tau)d\tau\right)^2 dt'\right]\ \exp\left[i\gamma\mathbf{v} \cdot \int_0^t \left(\int_0^{t'} \mathbf{G}(\tau)d\tau\right) dt'\right] \tag{2.30}$$

where the first part of the equation describes diffusion and the second part describes flow.

From equation 2.30, we can see that the signal attenuation due to diffusion depends on the magnitude of $D$, the total gradient area and the $\gamma$ of the nuclei under study. The effects of the gradients and $\gamma$ on the signal attenuation are combined into the $b$-value term [Le Bihan *et al.*, 1986], defined as

$$b = \gamma^2 \int_0^{TE} \left[\int_0^t \mathbf{G}\left(\tau\right) d\tau\right]^2 dt \tag{2.31}$$

The $b$-value characterizes the diffusion sensitivity of a sequence, just as the TE characterizes the degree of $T_2$ weighting of a spin echo sequence. The echo signal of a diffusion weighted sequence at $t = \mathrm{TE}$ can now be written as

$$S = S_0 \exp(-bD) \tag{2.32}$$

### 2.7.2 Pulsed Gradient Spin Echo Sequence

The pulsed gradient spin echo experiment, first demonstrated by Stejskal and Tanner in 1965, lies at the heart of most diffusion weighted pulse sequences [Stejskal and Tanner, 1965]. The sequence places a pair of gradient pulses symmetrically around the 180° refocusing pulse of a spin echo sequence (Figure 2.1). To evaluate the $b$-value for this sequence, we integrate equation 2.31 at $t = \mathrm{TE}$:

$$b = \gamma^2 G^2 \delta^2 (\Delta - \delta/3) \tag{2.33}$$

which is a term commonly seen in the literature. The exact form for the $b$-value depends on different gradient shapes, where analytical solutions have been derived for trapezoidal and sinusoidal gradient shapes [Bernstein *et al.*, 2004].

Since its inception, the pulsed gradient spin echo sequence has been used to measure translational motion in a variety of application, including cells [Tanner and Stejskal, 1968] and *in vivo* [Le Bihan *et al.*, 1986]. While other diffusion weighted sequences have also been developed, the principles behind each stems from this basic pulsed gradient spin echo sequence.

Diffusion weighted imaging (DWI) sequences incorporate an imaging readout and generate an image for each $b$-value. When taken together, these images can be used to generate an apparent diffusion coefficient (ADC) map, where the use of “apparent” reflects the complex diffusive motion of molecules within the tissue. In oncology, ADC mapping has become a

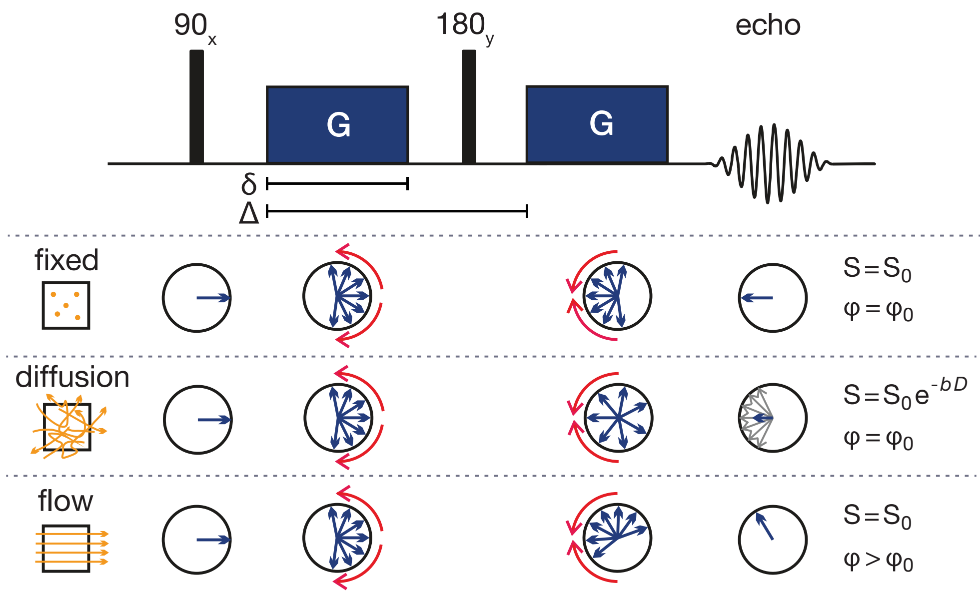


Figure 2.1: The pulsed gradient spin echo sequence used for measuring translational motion. Pulsed gradient pulses are placed symmetrically around the $180_y$ refocusing pulse, with duration $\delta$ and separation $\Delta$. Diffusive motion will cause a phase ($\varphi$) dispersion between all spins, leading to a reduction of the total signal (S). Flowing spins will experience some cohesive phase shift, while the signal amplitude will be preserved. Stationary or fixed spins will experience neither a phase shift nor a reduced signal amplitude. This example neglects signal loss due to $T_2$ relaxation.

valuable tool for the identification and characterization of tumors, first in the brain [Le Bihan *et al.*, 1986] but becoming more common in the body [Koh *et al.*, 2007].

For a more detailed discussion of diffusion, diffusion-weighted MR and its clinical role, the reader is directed to textbooks on these subjects [Price, 2009; Callaghan, 2011; Jones, 2011].

# Chapter 3

# Technical Background: Cancer Metabolism

## 3.1 Chapter Overview

Cancer, in the most general sense, is the uncontrolled growth of abnormal cells. In the body, cancers can occur in any organ or tissue. With the development of cell culture techniques, highly sensitive analytic techniques, genetic analysis and other modern assays over the past 100 years, our understanding of cancer has grown exponentially. Thanks to this increase in our understanding, many cancers, including stomach and cervical, have declined in the past decades. Yet, the incidence of several other cancers, such as kidney and thyroid, are on the rise [Siegel *et al.*, 2012; Jewett *et al.*, 2011]. While the survival rate for many localized cancers are high, it falls drastically for metastatic cancers [Siegel *et al.*, 2012]. Thus, there is a great need for further developing methods for the non-invasive *in vivo* assessment of the metastatic potential of cancers.

The following sections will give a brief overview of cancer and then focus on those areas that are relevant to the study of cancer with hyperpolarized $^{13}C$ pyruvate, namely pyruvate metabolism and the role of monocarboxylate transporters (MCTs). Finally, we will touch upon the role of hyperpolarized $^{13}C$ MR in the study of cancer metabolism, both *in vitro* and *in vivo*, to motivate the techniques developed in this dissertation for diffusion weighted MR of hyperpolarized $^{13}C$ metabolites.

## 3.2 The Hallmarks of Cancer

Cancers generally develops as a result of genetic mutations, activating a variety of processes that allow for sustained, unhindered growth. While cancer is a diverse set of diseases, cancer cells do share a number of common adaptive hallmarks. The most well-know list of these defining characteristics of malignant cancers is known as the "Hallmarks of Cancer" [Hanahan and Weinberg, 2000; Hanahan and Weinberg, 2011]:

- Self-sufficiency in growth signals
- Insensitivity to anti-growth signals
- Tissue invasion and metastasis
- Limitless replicative potential
- Sustained angiogensis
- Evading apoptosis
- Avoiding immune destruction
- Deregulation of cellular energetics

Each of these hallmarks are closely related to the unique aspects of cancer cell metabolism [Kroemer and Pouyssegur, 2008]. For example, increased glycolysis results from the cancer's self-sufficiency in growth signals and its limitless replicative potential. Glycolisys, in turn, promotes the cancer's ability to be insensitive to anti-growth signals and increased ability to metastatize to a secondary site. These connections can be seen in Figure 3.1.

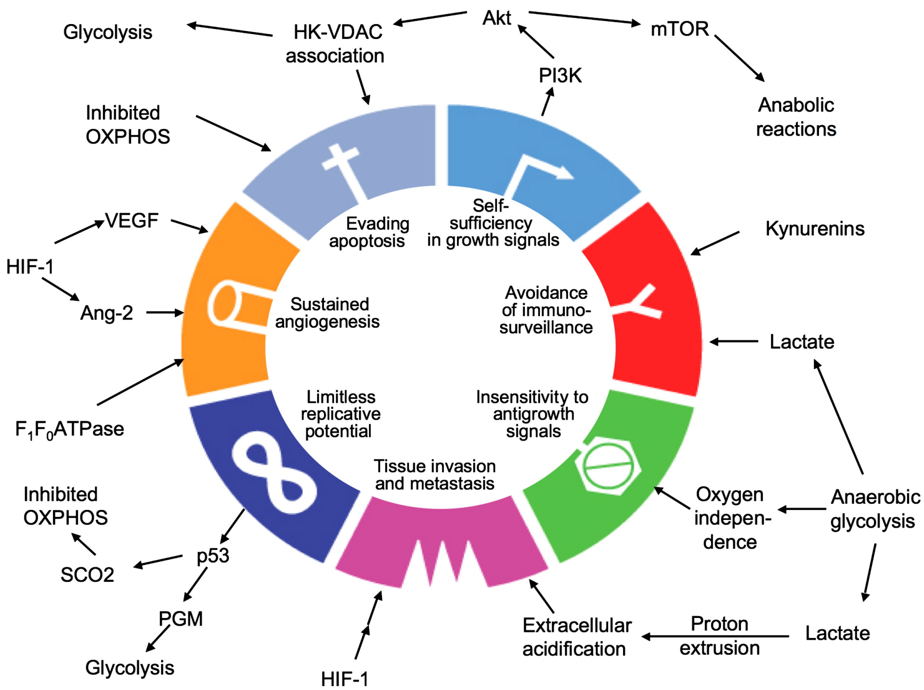


Figure 3.1: The link between cancer metabolism to the non-metabolic hallmarks of cancer. Arrows pointing *outwards* show how these hallmarks influence metabolism. Arrows pointing *inwards* indicate the affect of metabolism on a cancer's acquisition of these hallmarks. Adapted from [Kroemer and Pouyssegur, 2008].

## 3.3 An Increased Glycolytic Rate

In the 1920s, Otto Warburg made a monumental discovery: cancer cells preferred glycolytic metabolism even in the presence of oxygen [Warburg, 1956]. This phenomena, dubbed the "Warburg effect," is perplexing when viewed from an energetics standpoint, since the efficiency of glycolysis to produce ATP is about 19× smaller than that of oxidative phosphorylation. However, as tumors grow they quickly grow beyond the oxygen diffusion limit from the surrounding blood supply, leading to hypoxia or anoxia. In such a tumor environment, cancer cells must reduce their dependence on oxygen and thus use glycolysis to produce ATP. An oxygen-starved environment also promotes the hypoxia-inducible transcription factor (HIF). HIF, in turn, transcriptionally activates a long list of tumor promoting genes [Semenza, 2003] that express a variety of proteins essential to tumor metabolism, including glucose transporters (GLUT1), lactate dehydrogenase (LDH-A) and monocarboxylate transporters (MCT4) and more.

Despite the stoichiometrically inefficient production of ATP with glycolysis versus oxidative phosphorylation, several reasons have been put forward to explain why cancer cells adopt this form of metabolism [DeBerardinis *et al.*, 2008]. First, as mentioned, glycolysis runs independently of the presence of oxygen, which is essential in hypoxic or anoxic tumor environments. Additionally, when the rate of glycoysis is increased, it has the potential to produce more ATP than via mitochondrial metabolism. If fact, glycolysis may exceed the max enzymatic rate of pyruvate dehydrogenase (PDH), the first enzyme of mitochondrial metabolism, by over an order of magnitude [Curi *et al.*, 1988]. Finally, glucose degradation provides cells with intermediates needed several biosynthesis pathways and sustained proliferation.

The last step in glycolysis is mediated by the enzyme lactate dehydrogenase (LDH). Two LDH genes, *LDHA* and *LDHB*, encode for the two different subunits of the enzyme, M and H, respectively. Four subunits come together in any combination to form the LDH enzyme. LDH-1, expressed in most cells, has four H subunits and preferentially converts lactate into pyruvate [Koukourakis *et al.*, 2003]. LDH-5 is found predominately in cancer cells and is upregulated by HIF. It has four M subunits and preferentially converts pyruvate into lactate

[Koukourakis *et al.*, 2003]. Thus, the upregulation of *LDHA* drives glycolysis that is essential to cancer metabolism.

## 3.4 Acidification of the Extracellular Environment

The upregulation of glycolysis produces significant amounts of lactate, which to the detriment of the cancer cells could slow glycolysis and disrupt intracellular pH balance. To counter these problems, cancer cells use the HIF-induced upregulation of the monocarboxylate transporter 4 (MCT4) [Ullah *et al.*, 2006] to export both lactate and its associated proton from the cytosol into the surrounding interstitial spaces surrounding the tumor.

MCT1–MCT4 are a subset of MCTs that are proton symporters and facilitate the transmembrane transport of pyruvate, lactate and other moncarboxylic acid containing molecules. MCT1 is found in a variety of tissues and exhibit their highest affinity for pyruvate, but also transport lactate [Pinheiro *et al.*, 2012]. Generally, MCT1 plays a major role in the uptake of monocarboxylic acids. MCT4, on the other hand, is predominantly found in cancer tissue, has a high affinity for lactate and regulates the export of lactate and protons from cancer cells [Pinheiro *et al.*, 2012].

In cancer cells, MCTs are one of many plasma membrane ion pumps that help maintain an intracellular physiologic pH. In doing so, the rapid export of protons acidifies the surrounding, poorly-perfused extracellular environment, typically reaching a pH $\approx 6.7 - 7.1$ [Webb *et al.*, 2011]. This pH reduction promotes degradation of the extracellular matrix (ECM) and cancer cell invasion [Webb *et al.*, 2011; Stock and Schwab, 2009]. It has been shown that highly aggressive cancer cells acidify the extracellular environment more than less aggressive cancer cells, and certainly more than normal cells [Montcourrier *et al.*, 1997]. Thus, a highly acidic extracellular environments and MCT4 expression correlates with the metastatic potential of cancer cells [Gallagher *et al.*, 2007].

## 3.5 Hyperpolarized $^{13}$C in Cancer MR

Over the past decade, techniques using hyperpolarized $^{13}$C MR have been developed to study real-time cancer metabolism [Kurhanewicz *et al.*, 2011]. Most often, the flux of hyperpolarized $^{13}$C pyruvate to hyperpolarized $^{13}$C lactate has been measured, where a high flux is indicative of a tumor. This has been shown in a variety of tumors, including prostate tumors [Albers *et al.*, 2008] and brain tumors [Park *et al.*, 2010]. Other hyperpolarized $^{13}$C molecular probes can also be used. Hyperpolarized $^{13}$C biocarbonate, for example, has been used to measure pH *in vivo* [Gallagher *et al.*, 2008].

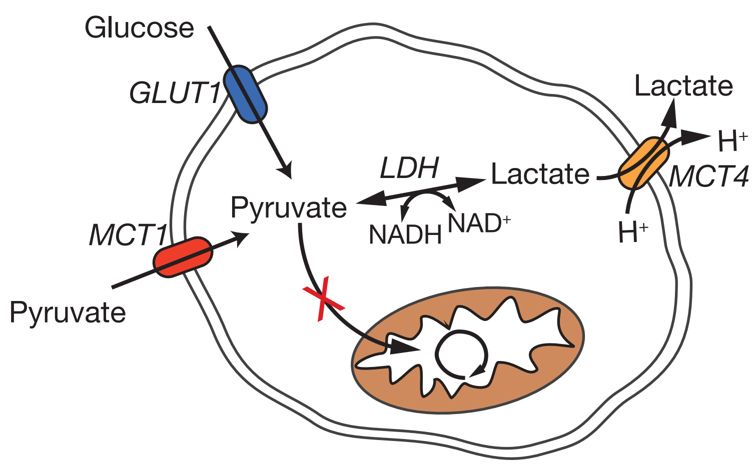


Figure 3.2: This schematic of a cancer cells shows the main components of metabolism that are relevant for the hyperpolarized $^{13}$C pyruvate and lactate studies presented in this dissertation. Increased glycolysis promotes the uptake of glucose through GLUT1 transporters and pyruvate through MCT1. The cancer cells forgoes mitochondrial metabolism and instead produces lactate via the enzyme LDH. The export of lactate and protons from cytoplams via MCT4 acidifies the extracellular environment and promotes the formation of metastases.

Cancer cell studies with hyperpolarized $^{13}$C pyruvate have been carried-out in bioreactors [Keshari *et al.*, 2010], perfusion systems that maintain cell viability while allowing for multiple studies. Various pre-clinical animal models have also been used to study *in vivo*, real-time metabolism, including mice [Albers *et al.*, 2008], rats [Chaumeil *et al.*, 2013], pigs [Lau *et al.*, 2010] and dogs [Nelson *et al.*, 2008]. These pre-clinical studies allow for both the development of hyperpolarized $^{13}$C acquisition techniques and for a deeper understanding of real-time cancer metabolism. But, the true greatest value for the technique lies in the clinic.

The use of hyperpolarized $^{13}$C MR in humans provides an opportunity to identify and characterize tumors unmatched by any other current clinical imaging modality. The completion of the first clinical trial using hyperpolarized $^{13}$C pyruvate successfully demonstrated use of the technique to identify tumors [Nelson *et al.*, 2013]. It is important to note that $^{1}$H spectroscopy (MRSI) can also be used to measure lactate *in vivo*. But, the use of $^{1}$H MRSI has many disadvantages that limit clinical adoption, including overlapping lipid peaks that complicate quantification and low SNR that results in long scan times. In addition to overcoming both of these shortcomings of $^{1}$H MRSI, hyperpolarized $^{13}$C lactate detects only metabolically active lactate, namely that generated by living cells from the injected hyperpolarized $^{13}$C pyruvate.

Work thus far in the hyperpolarized $^{13}$C MR field has been to study the generation of metabolites and use these flux measurements to identify tumors. But, as discussed above, understanding the localization of lactate could also help in characterizing cancer aggressiveness. The work presented in this dissertation focuses on developing the technique of diffusion weighted hyperpolarized $^{13}$C MR to allow for the differentiation of extracellular and intracellular hyperpolarized $^{13}$C lactate. Additionally, the technique provides a general understanding of the tissue microenvironment in which hyperpolarized $^{13}$C metabolites can reside.

# Chapter 4

# Hyperpolarized $^{13}$C-Pyruvate MR Reveals Rapid Lactate Export in Metastatic Renal Cell Carcinomas

## 4.1 Chapter Overview

The following work shows how the extra- and intracellular distribution of hyperpolarized $^{13}$C lactate varies with cancer aggressiveness. This work motivates that development of diffusion weighted techniques for hyperpolarized $^{13}$C metabolites, which can be used to localize these metabolites based on their mobility within a certain microenvironment, e.g., extra- and intracellular or vascular and within dense tissue. Since noninvasive methods to confidently predict a tumors biological behavior and select the most appropriate treatment for individual patients are lacking, diffusion weighted techniques for measuring the localization of hyperpolarized $^{13}$C lactate, as discussed in later chapters of this dissertation, could could provide more personalized therapeutic selection.

This work focuses on renal cell carcinomas (RCCs), which are a heterogeneous group of tumors with a wide range of aggressiveness. Here, we investigate the dynamic metabolic flux in living RCC cells using hyperpolarized $^{13}$C-pyruvate magnetic resonance spectroscopy (MRS) combined with a bioreactor platform, and interrogated the biochemical basis of the MRS data with respect to cancer aggressiveness. RCC cells have significantly higher pyruvate-to-lactate flux than the normal renal tubule cells. Furthermore, a key feature distinguishing the localized from the metastatic RCC cells is the lactate efflux rate, mediated by the monocarboxylate transporter 4 (MCT4). Metastatic RCC cells have significantly higher MCT4 expression and correspondingly higher lactate efflux, which is essential for maintaining a high rate of glycolysis. We show that such differential cellular transporter expression and associated metabolic phenotype can be noninvasively assessed via real-time monitoring of hyperpolarized $^{13}$C pyruvate-to-lactate flux.

## 4.2 Introduction

The incidence of renal tumors, both malignant renal cell carcinomas (RCCs) and benign renal tumors, has risen by approximately 150% in the last 30 years [Chow and Devesa, 2008; Patard, 2009]. In the case of renal tumors, biopsies are not routinely done, due to the risk of hemorrhage and high likelihood of indeterminate histology [Volpe *et al.*, 2008; Shannon *et al.*, 2008]. Treatment selection is thus heavily reliant on non-invasive imaging assessment of tumor masses. However, there are significant limitations to the current imaging methods for renal tumor characterization. It is increasingly recognized that RCCs are a heterogeneous group of tumors with a wide range of biological aggressiveness [Eggener *et al.*, 2006; Jewett *et al.*, 2011]. Emerging active surveillance data have shown that a significant percentage of small RCCs ($< 4$cm) are indolent with low metastatic risk, and patients may be over-treated if all such RCCs are surgically removed [Jewett *et al.*, 2011; Crispen *et al.*, 2009]. On the other hand, 20–40% of patients undergoing nephrectomies for clinically localized RCCs develop metastases with poor outcome [Lam *et al.*, 2005]. Unfortunately, current imaging methods cannot reliably predict the risks of progression from localized RCC to metastatic disease [Sun *et al.*, 2011]. Furthermore, certain benign renal tumors are difficult to distinguish from RCCs by imaging [Millet *et al.*, 2011]. This diagnostic challenge has resulted in the unnecessary resection of many benign renal tumors, which constitute 20% of all renal tumors $< 4$cm, with the associated surgical risks and potential loss of renal function [Cooperberg *et al.*, 2008]. Therefore, new imaging methods are needed to predict the biological behavior of renal tumors and select appropriate treatment.

The unique metabolism of cancer cells is central to their malignant behavior. For example, a common property of cancers is altered glucose metabolism with elevated glycolysis and lactate production in the presence of oxygen [Gatenby and Gillies, 2004; Warburg, 1956]. Increased glycolysis facilitates the uptake and incorporation of nutrients and biomass needed for cell proliferation in cancers [Vander Heiden *et al.*, 2009; Costello and Franklin, 2005], and acidifies the extracellular microenvironment promoting invasion of neighboring tissue and metastasis [Gatenby *et al.*, 2006]. A number of genomic and proteomic studies have demonstrated increased metabolism to lactate in RCCs [Unwin *et al.*, 2003; Semenza, 2007; Langbein *et al.*, 2008; Gao *et al.*, 2008]. Specifically, proteomic analysis of RCC tissues and metabolic profiling of serum samples revealed increased levels of glycolytic enzymes in RCC tissues and higher lactate in the serum of RCC patients [Gao *et al.*, 2008]. Metastatic RCCs have also demonstrated a bio-energetic shift toward aerobic glycolysis and lactate production [Langbein *et al.*, 2008]. These studies provide the rationale for metabolic imaging of glycolysis as a non-invasive means to characterize renal tumor aggressiveness.

Hyperpolarized $^{13}C$ MR is a molecular imaging technique that allows rapid and noninvasive monitoring of dynamic pathway-specific metabolic and physiological processes. Hyperpolarization, achieved through the dynamic nuclear polarization (DNP) technique [Ardenkjær-Larsen *et al.*, 2003], can provide dramatic gains in sensitivity (> 10,000-fold increase) for imaging $^{13}C$-labeled bio-molecules. The hyperpolarized $^{13}C$ probes can be injected into living systems, and their metabolism can be observed in real-time by chemical shift. The most commonly used hyperpolarized $^{13}C$ probe is $^{13}C$ pyruvate, which is at the juncture of several important energy and biosynthetic pathways. For example, pyruvate may be converted to lactate in glycolysis, to acetyl-CoA to support the tricarboxylic acid (TCA) cycle, or to alanine via transamination for protein synthesis. Hyperpolarized $^{13}C$ pyruvate MR has already been applied to the detection of the presence [Chen *et al.*, 2007; Cunningham *et al.*, 2007; Hu *et al.*, 2008; Kurhanewicz *et al.*, 2008; Golman and Petersson, 2006] and progression [Albers *et al.*, 2008; Zierhut *et al.*, 2010] of a number of cancers. The metabolic changes seen in RCCs suggest that hyperpolarized $^{13}C$ pyruvate will also be an excellent probe to interrogate these tumors noninvasively.

In this work, we compared the pyruvate metabolism of immortalized cells derived from human renal proximal tubules (the origin of most human RCCs), a localized human RCC, and a metastatic human RCC, with the goal of identifying clinically translatable hyperpolarized biomarkers of renal tumor aggressiveness. After evaluating the steady-state metabolism of these cells, we assessed the dynamic hyperpolarized pyruvate-to-lactate flux using a MR-compatible bioreactor platform that provides a controlled and physiological setting for the cells [Keshari *et al.*, 2010]. By monitoring the real time metabolic flux using hyperpolarized MR, we showed that RCC cells have significantly higher pyruvate-to-lactate flux than the normal renal proximal tubule cells. Furthermore, we showed that cells derived from the metastatic RCC have more rapid export of lactate to the extracellular space compared to the cells derived from the localized RCC, and that these differences are likely mediated by the differential expression of monocarboxylate transporter 4 (MCT4). These results suggest that using hyperpolarized $^{13}$C pyruvate to assess lactate production and export has the potential to improve the non-invasive characterization of renal tumors.

## 4.3 Methods

### 4.3.1 Cell Lines

HK-2 is an immortalized proximal tubule epithelial cell line from normal adult human kidney [Ryan *et al.*, 1994], and was obtained from American Type Culture Collection (ATCC, Virginia; obtained June, 2010; authentication performed at ATCC was via Short Tandem Repeat (STR) Profiling). UMRC6 cells are representative of localized human clear cell renal cell carcinoma [Grossman *et al.*, 1985], and were a gift from Dr. Bart Grossman (MD Anderson Cancer Center; obtained January, 2010; authenticated using STR Profiling, October 2012). UOK262 cells are derived from a metastasis of the highly aggressive hereditary leiomyomatosis renal cell carcinoma(HLRCC), which is characterized by mutation of the TCA cycle enzyme fumarate hydratase(FH) [Yang *et al.*, 2010]. UOK262 cells were a gift from Dr. W. Marston Linehan (National Cancer Institute; obtained May, 2010; authenticated using STR Profiling, October 2012). All cells were grown in Dulbecos Modified Eagles medium (DMEM) with 4.5 g $L^{-1}$ glucose. The cells were passaged serially and were used for assays and MR experiments between passages 2–10 and at 60–80% confluency.

### 4.3.2 $^1$H NMR Experiments

Cells were plated on 150 $cm^2$ coated petri dishes (Fisher Scientific) and incubated for 24 h in DMEM media supplemented with [1-$^{13}$C] glucose, or for 2 h in DMEM media supplemented with [3-$^{13}$C] pyruvate (Cambridge Isotope Labs, MA). At the end of incubation, an aliquot of medium was collected, and cells were extracted in ice-cold methanol. The cell extracts were reconstituted in $D_2O$ with known amounts of trimethyl silyl pentanoate (TSP) for internal reference. The extracts were measured on Bruker Advance III 800MHz equipped with a cryo-cooled triple resonance probe. High-resolution water-suppressed proton spectra were obtained with a repetition time of 12 s and 64 averages. The metabolite peak areas were quantified against the known TSP peak area.

### 4.3.3 Hyperpolarized $^{13}$C Pyruvate MR Bioreactor experiment

Cells were electrostatically encapsulated into 2.5% weight/volume alginate microspheres as previously described [Keshari *et al.*, 2010; Chandrasekaran *et al.*, 2006], and then loaded into a MR-compatible bioreactor. Approximately 800 μL of microspheres were perfused in the bioreactor with DMEM H-21 media at a flow rate of 2.5 mL min$^{-1}$. For the flow rate modulation bioreactor experiments, the flow rate was changed to either 1.3 mL min$^{-1}$ or 3.8 mL min$^{-1}$ for the duration of the hyperpolarized scans. The media was kept at 37°C with water-jacketed perfusion lines and was maintained at 95% air/5% $CO_2$ via gas exchanger. All bioreactor studies were performed on a 500 MHz Varian Inova (Agilent Technologies, CA) with a 10 mm, triple-tune, direct-detect, broadband probe at 37°C. For the hyperpolarized $^{13}$C-pyruvate studies, 2.5 μL of 14.2 M [1-$^{13}$C] pyruvate mixed with 15 mM of the trityl radical (GE Healthcare) was polarized on a Hypersense polarizer (Oxford Instruments, UK). This was followed by dissolution in 5 mL of 50 mM phosphate buffer. 1 mL of the resulting

7.5 mM HP pyruvate solution was injected into the bioreactor containing the microspheres. Hyperpolarized $^{13}$C MR data were acquired dynamically with a 10° flip-angle, pulse repetition time of 3 s and for a duration of 300 s. $^{31}$P spectra (TR 3 s, 1024 averages, 90° flip angle) were acquired before and after each hyperpolarized study to assess cell viability.

### 4.3.4 Cell Number Determination for Bioreactor Experiments

Moles of ATP per cell for each cell line were measured using CellTiter-Glo luminescent cell viability assay and Veritas Luminometer (Promega, WI). Moles of ATP corresponding to the β-NTP peak area on $^{31}$P spectra were determined using a $^{31}$P calibration curve. The number of cells in each bioreactor experiment was then calculated by dividing the moles of ATP approximated from β-NTP peak by the moles of ATP per cell as measured by the luminescent assay.

### 4.3.5 mRNA Expression and Enzyme Activity Assay

Total RNA was purified from cells using RNeasy procedure kit (Qiagen, USA), and reverse transcribed using iScript cDNA Synthesis kit (BioRad Laboratories, CA). PCR was conducted in triplicate for lactate dehydrogenase α (LDH-α) and the monocarboxylate transporters 1 and 4 (Hs00161826_m1, Hs00358829_m1) on the ABI 7900HT (Applied Biosystems, CA). Cyclophilin and β actin (Applied Biosystems, CA) were used as control, and the relative fold difference was calculated for each primer/probe combination.

LDH activity of cell lysates was measured spectrophotometrically by quantifying the linear decrease in nicotinamide adenine dinucleotide (NADH) absorbance at varying pyruvate concentrations at 339 nm using a microplate reader (Tecan Group Ltd., Switzerland). The maximum velocity ($V_{max}$) and the Michaelis-Menten constant ($K_m$) were estimated using the Lineweaver- Burke plot.

### 4.3.6 Data Analysis

The hyperpolarized pyruvate-to-lactate flux was calculated using a previously published model [Keshari *et al.*, 2010]. The pyruvate-to-lactate flux was normalized by the number of cells in each bioreactor study and the injected amount of hyperpolarized pyruvate. $^{31}$P metabolite peaks were integrated and normalized by the number of cells to determine the concentration of phosphocholine (PC), glyercophosphocholine (GPC) and β nucleoside triphosphates (β-NTP). Resonances were corrected for their respective $^{31}$P $T_1$ relaxation times (Table 4.1). One way analysis of variance (ANOVA) was used to assess the difference between the 3 groups with Tukey-Kramer HSD post-hoc tests using statistical software package JMP (SAS Institute, NC, USA). All values are reported as mean ± standard error.

## 4.4 Results

### 4.4.1 Steady-State Metabolite Concentrations with $^1$H MRS

We first utilized 1H MR spectroscopy (MRS) to interrogate the steady-state metabolite concentrations in HK2, UMRC6 and UOK262 cells. HK2 cells are derived from human renal proximal tubule cells (doubling time = 72–96 h) [Ryan *et al.*, 1994]. UMRC6 cells (doubling time = 43 h) originate from a localized human clear cell RCC [Grossman *et al.*, 1985]. Lastly, UOK262 cells were isolated from a metastasis of hereditary leiomyomatosis renal cell carcinoma (HLRCC) (doubling time = 23 h) [Yang *et al.*, 2010]. HLRCC is an aggressive RCC characterized by mutation of the tricarboxylic acid (TCA) cycle enzyme fumarate hydratase (FH). UOK262 cells therefore have markedly reduced oxidative phosphorylation and are highly glycolytic [Yang *et al.*, 2010]. Figure 4.1a illustrates the biochemical scheme of glycolysis and TCA cycle. Figure 4.1b shows the major steady-state intracellular metabolite concentrations, as measured by 1H MRS, in the 3 cell lines. We found that the steady-state lactate concentration was significantly higher in the UOK262 cells compared to the UMRC6 or HK2 cells (both $p < 0.05$). The increased steady-state lactate in the UOK262 cells is consistent with the FH mutation, which sharply attenuates the mitochondrial TCA cycle and concomitantly drives glycolysis for energy production [Yang *et al.*, 2010].

The alanine concentration was lower in the two RCC cell lines compared to the HK2 cells, likely due to increased flux of pyruvate to lactate. We also found significantly increased glutamate and decreased aspartate concentration in the UOK262 cells compared to the other 2 cell lines. Glutamate is reversibly formed from $\alpha$-ketoglutarate, a TCA cycle intermediate proximal to fumarate. Aspartate is formed reversibly from oxaloacetate, a TCA intermediate distal to fumarate. In the UOK262 cells, the increased steady-state glutamate and reduced aspartate are consistent with truncation of TCA cycle metabolism beyond fumarate, due to the FH mutation. The concentration of glycerophosphocholine (GPC), an abundant renal osmolyte [Nakanishi and Burg, 1989], was similar among the 3 cell lines. Interestingly, we found that phosphocholine (PC) was significantly higher in the UMRC6 cells than the UOK262 cells. While PC has been used as a biomarker of tumor proliferation and aggressiveness in other types of cancers [Shah *et al.*, 2010; Eliyahu *et al.*, 2007], the levels of PC did not correlate with aggressiveness in the RCC cell lines in our study. PC is converted from choline by the enzyme choline kinase $\alpha$ (CHKA) in the phosphatidylcholine synthesis (Kennedy) pathway. A recent study reported that CHKA forms a complex with epidermal growth factor receptor (EGFR) in a c-Src-dependent manner, and functions cooperatively with EGFR and c-Src in regulating pathways critical to cell proliferation [Miyake and

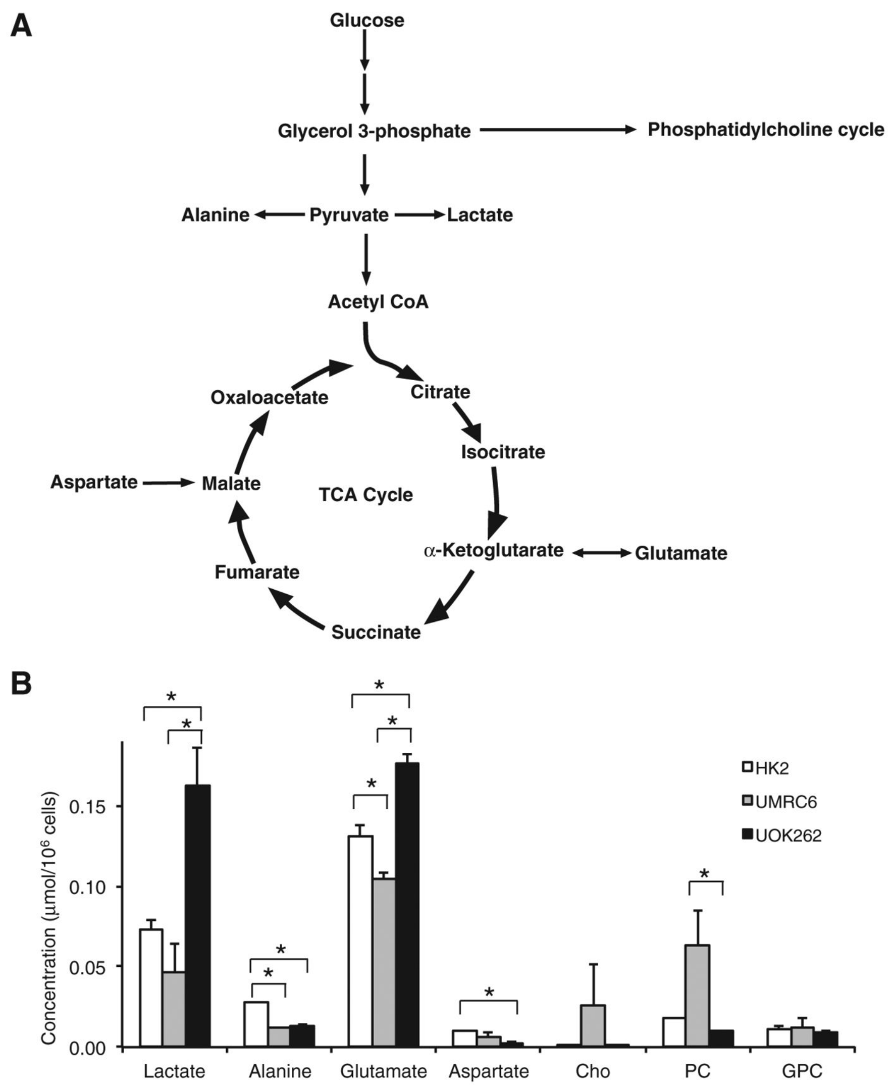


Figure 4.1: Major $^{1}$H steady-state metabolites in the 3 renal cell lines. (**a**) Biochemical scheme of glycolysis and tricarboxylic acid (TCA) cycle. (**b**) Steady-state concentrations of major metabolites, as measured by $^{1}$H MRS, in the 3 cell lines (N = 5 each). HK2 are normal renal cells, UMRC6 are localized RCC cells and UOK262 are metastatic RCC cells. All values are reported as mean $\pm$ std. err. * denotes significant difference ($p < 0.05$).

Parsons, 2012]. Such required functional interaction among the three enzymes for cancer cell proliferation may in part explain the lack of direct correlation between the PC levels and proliferation rates/aggressiveness of the two RCC cell lines in our study.

### 4.4.2 Labeling Studies with [1-$^{13}$C] Glucose and [3-$^{13}$C] Pyruvate

To further characterize glycolysis and lactate production in the RCC cells, we investigated the flux from labeled [1-$^{13}$C] glucose to lactate in 2D cell cultures following 24 hr incubation. Figure 4.2a shows the scheme of $^{13}$C labeled carbon atom transitions used to detect glucose metabolism to lactate. Glucose, the primary fuel for energy in cells, is taken up primarily via the glucose transporter 1 (GLUT1), and is converted to pyruvate and then lactate during glycolysis. Lactate is preferentially exported out of the cells via the monocarboxylate transporter 4 (MCT4) [Dimmer *et al.*, 2000]. Figure 4.2b and 4.2c demonstrate representative MR spectra of metabolites in the culture medium and intracellular compartment, respectively, of UOK262 cells following 24 hr labeling with [1-$^{13}$C] glucose. Figure 4.2d and 4.2e show the concentrations of $^{13}$C labeled lactate in the medium and the intracellular compartment, respectively, of the 3 cell lines following incubation with [1-$^{13}$C] glucose. After 24 hr of incubation with [1-$^{13}$C] glucose, 99% of lactate was found in the extracellular medium. The concentration of $^{13}$C lactate in the medium increased progressively from HK2 to UMRC6 to UOK262 cells, with the lactate concentration being nearly three-fold higher in the medium of UOK262 cells compared to that of the HK2 cells. The fractional enrichment (FE) of lactate was defined as the $^{13}$C labeled lactate / ($^{13}$C labeled lactate + unlabeled lactate). The FE of lactate in the medium was 76 ± 1%, 65 ± 2% and 84 ± 1% in the HK2, UMRC6 and UOK262 cells, respectively. This implies that the predominant source of lactate in these cells is glucose, although there is a contribution from other carbon sources as well. The intracellular concentration of $^{13}$C lactate was also significantly higher in the UOK262 cells compared to the UMRC6 or the HK2 cells ($p < 0.05$). The intracellular FE of lactate was 62.5 ± 3.1%, 61.8 ± 1.5% and 78.6 ± 0.4% in the HK2, UMRC6 and UOK262 cells, respectively. The differential lactate FE in the intracellular compartment and the medium might be related to lactate compartmentalization in the cells. Such compartmentalization has been reported to exist in the brain and myocardium [Sickmann *et al.*, 2005; Chatham and Forder, 1996]. It is possible that one compartment of intracellular lactate originates predominantly from $^{13}C$ labeled glucose, and the subsequently labeled lactate is preferentially exported into the medium. Another compartment of lactate may derive from other sources such as from glutamine via glutaminolysis [Wise and Thompson, 2010], and this compartment of lactate may not be as readily exported into the medium as that from glucose. The presence of lactate compartmentalization may also in part explain the higher FE of intracellular lactate in the UOK262 cells compared to the other cells. Because UOK262 have FH mutation with reduced TCA cycle metabolism, they are more likely to produce lactate from glycolysis than from other pathways such as glutaminolysis that contains parts of the TCA cycle. This may explain the higher FE of the intracellular lactate from labeled glucose in the UOK262 cells. Taken together, the above findings confirmed that UOK262 cells are highly glycolytic with increased production of lactate. Interestingly, the $^{13}C$ lactate concentration was lower in the UMRC6 RCC cells relative to both HK2 and UOK262 cells. This was in agreement with the steady-state intracellular lactate concentration data, which also showed a decreased lactate pool in UMRC6 cells compared to the other two cell lines (Figure 4.1b).

### 4.4.3 Real-Time Pyruvate-to-Lactate Flux using Hyperpolarized $^{13}C$

Given the dynamic nature of cellular metabolism, we then investigated the real-time pyruvate metabolism in the 3 cell lines utilizing hyperpolarized $^{13}C$ MR. We performed our hyperpolarized $^{13}C$ MR experiments using a bioreactor, a continuously perfused 3D cell culture system that provides a controlled and physiological setting for the cells. This system has been shown to produce highly reproducible hyperpolarized MR data [Keshari *et al.*, 2010], and facilitates the characterization of hyperpolarized substrate to metabolite conversion. $^{31}P$ MR spectroscopy was employed to monitor changes in cell bioenergetics during the

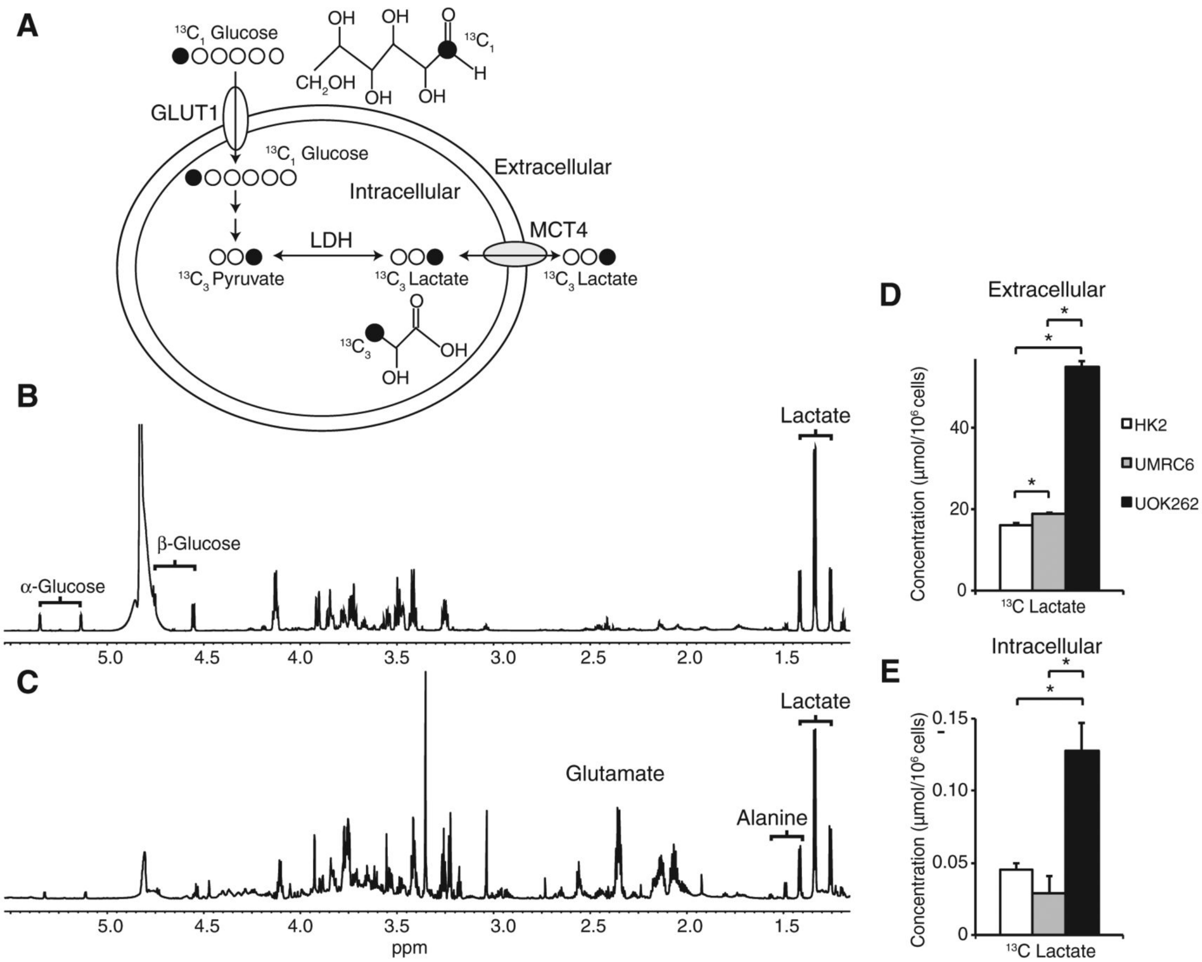


Figure 4.2: $^{13}C$ labeled lactate in the media and intracellular compartment of the 3 cell lines following 24 hour incubation with [1-$^{13}C$] glucose. (**a**) Biochemical scheme illustrating $^{13}C$ labeled carbon atom transitions used to detect glucose metabolism to lactate. Representative $^{1}H$ MR spectra of metabolites in the medium (**b**) and intracellular compartments (**c**) of UOK262 following 24 hour labeling with [1-$^{13}C$] glucose. The brackets indicate the $^{13}C$ satellites of each metabolite. Concentrations of $^{13}C$ labeled lactate in the media (**d**) and intracellular compartment (**e**) of the 3 cell lines following incubation with [1-$^{13}C$] glucose (N = 5 each). All values are reported as mean $\pm$ std. err. * denotes significant difference ($p < 0.05$).

bioreactor studies. Representative $^{31}P$ spectra of the cells are shown in supplementary data (Figure 4.7). NMR signals for the nucleoside triphosphates (NTPs: $\gamma$NTP, $\alpha$NTP, and $\beta$NTP), phosphocholine (PC), inorganic phosphate ($P_i$), and glycerol phosphocholine

(GPC) were readily visible. The total NTP content was unchanged following the injection of hyperpolarized $^{13}$C pyruvate, indicating maintenance of cell viability during the course of the hyperpolarized experiments. Figure 4.3 shows the PC/GPC ratios and PC+GPC concentration in the 3 cell lines. We found significantly higher PC+GPC concentration in the UMRC6 cells compared to the UOK262 cells ($p < 0.05$), which was in agreement with the steady-state $^{1}$H data from 2D cell culture. In addition to monitoring cell energetics, $^{31}$P spectroscopy also enables quantitative hyperpolarized data analysis by normalizing the hyperpolarized MR data with respect to the number of viable cells, through concomitant measurements of βNTP concentration via $^{31}$P MRS.

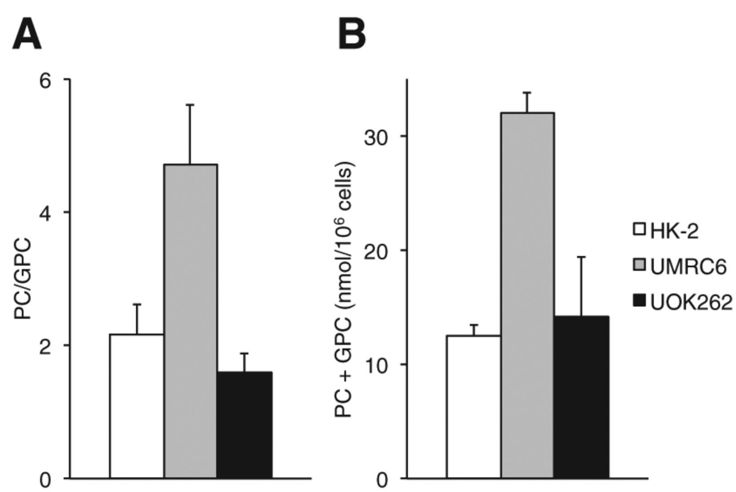


Figure 4.3: Phosphocholine metabolites in the 3 renal cell lines. PC/GPC ratios (**a**), and PC+GPC concentration (**b**) of cells encapsulated and perfused in a bioreactor (N = 5 each). All values are reported as mean ± std. err. PC phosphocholine, GPC glycerophosphocholine.

Figure 4.4a illustrates the scheme of $^{13}$C labeled carbon atom transitions used to detect $^{13}$C pyruvate metabolism during the hyperpolarized MR experiment. After the injection of hyperpolarized $^{13}$C pyruvate into the bioreactor, the real time pyruvate-to-lactate flux was assessed for all three cells lines. The data were fit to a two-state model of interconversion of pyruvate to lactate and the metabolic fluxes were calculated [Keshari *et al.*, 2010]. Figure 4.4b shows fitted pyruvate-to-lactate flux and representative spectra of $^{13}$C pyruvate and lactate. The average fluxes, at a flow rate of 2.5 mL min$^{-1}$ in the bioreactor, for each of these cell lines are demonstrated in Figure 4.4c. The observed flux rate was significantly higher in the two RCC cell lines (UMRC6 and UOK262) as compared to the renal tubule cell line HK2 (UMRC6 vs. HK2 $p < 0.0001$, UOK262 vs. HK2 $p = 0.003$). Unexpectedly, the observed real time hyperpolarized pyruvate-to-lactate flux for UOK262 cells (representative of metastatic RCC) was lower than that of the UMRC6 cells (representative of localized RCC). Similar to the flux data, the area under of the curve for the $^{13}$C lactate was higher in the RCC cells than the normal renal tubule cells, but was lower in the UOK262 RCC cells than the UMRC6 RCC cells (supplemental data, Table 4.2). Additional analysis of hyperpolarized $^{13}$C dynamics of the cells perfused in the bioreactors was summarized in Table 4.2.

### 4.4.4 LDH Activity Assay and mRNA Expression of LDHA and MCTs

To better understand the cellular processes underlying the hyperpolarized pyruvate flux results, we then assayed the mRNA expression and enzyme activity level of LDHA, and the mRNA expression of MCT1 and MCT4 in the 3 cell lines. LDHA encodes the predominantly M isoform of LDH, which catalyzes the conversion between pyruvate and lactate. MCT1 mediates the pyruvate transport into the cells, and MCT4 mediates the efflux of the lactate out of the cells [Kroemer and Pouyssegur, 2008]. We found that the mRNA expression of LDHA was significantly higher in the UOK262 cells than the other two cell lines (Figure 4.5). For the LDH activity, $K_m$ of the two RCC cell lines was significantly higher than that of the HK2 cells ($p < 0.03$), but not significantly different between the UMRC6 and UOK262 RCC cells. The $V_{max}$ of UOK262 cells was significantly higher than that of HK2

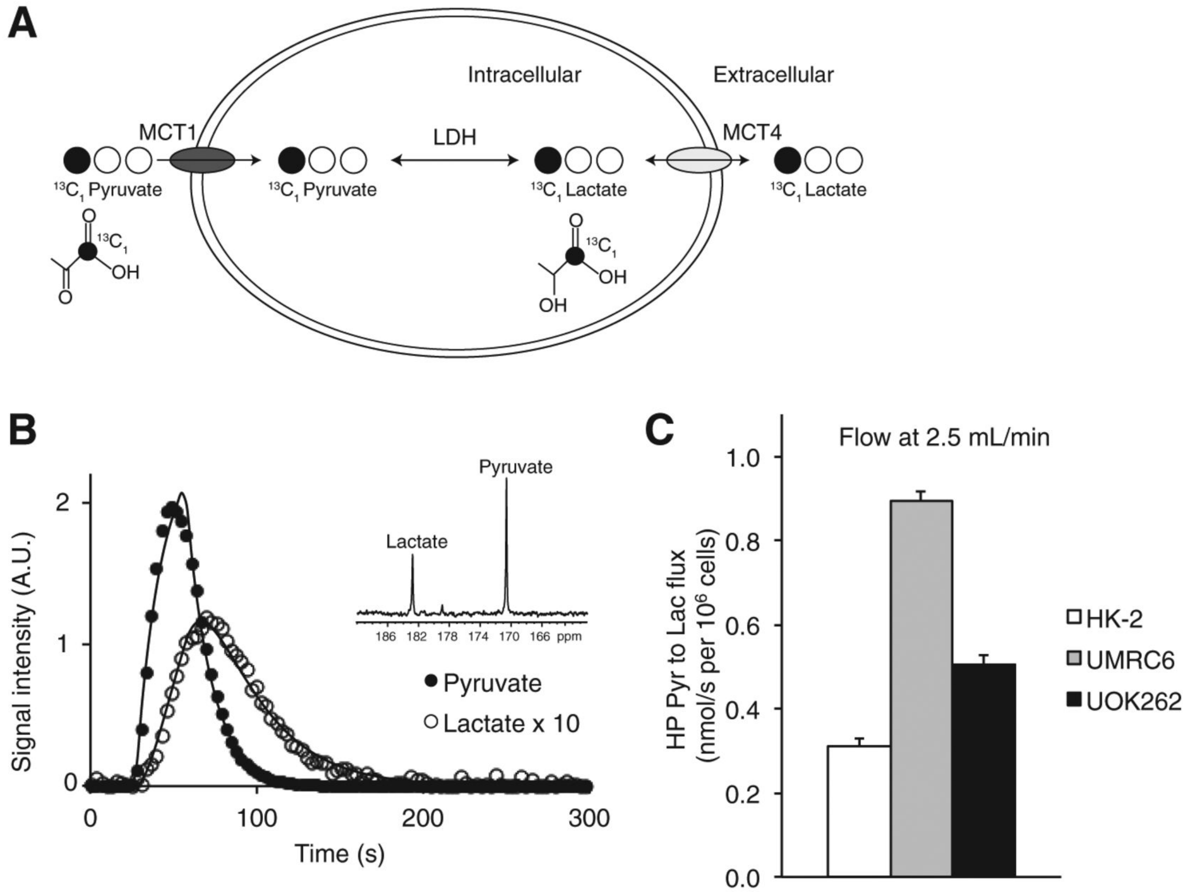


Figure 4.4: Dynamic hyperpolarized $^{13}$C pyruvate-to-lactate flux in the 3 renal cell lines. (**a**) Scheme of $^{13}$C labeled carbon atom transitions used to detect $C_1$ labeled pyruvate metabolism during the hyperpolarized experiment. (**b**) Fitted pyruvate-to-lactate flux and representative spectra (inset) of $^{13}$C pyruvate and lactate in the UMRC6 cells. (**c**) Comparison of observed real time hyperpolarized pyruvate-to-lactate flux in the 3 cell lines at a flow rate of 2.5 mL min$^{-1}$ in the bioreactor (N = 5 each). All values are reported as mean $\pm$ std. err.

cells ($p < 0.05$). The mRNA expression of MCT1 was significantly higher in the UMRC6 cells (UMRC6 vs. HK2, $p = 0.0004$; UMRC6 vs. UOK262, $p = 0.0002$) while the MCT4 expression was significantly elevated in the UOK262 cells (UOK262 vs. HK2, $p = 0.001$; UOK262 vs. UMRC6, $p = 0.02$).

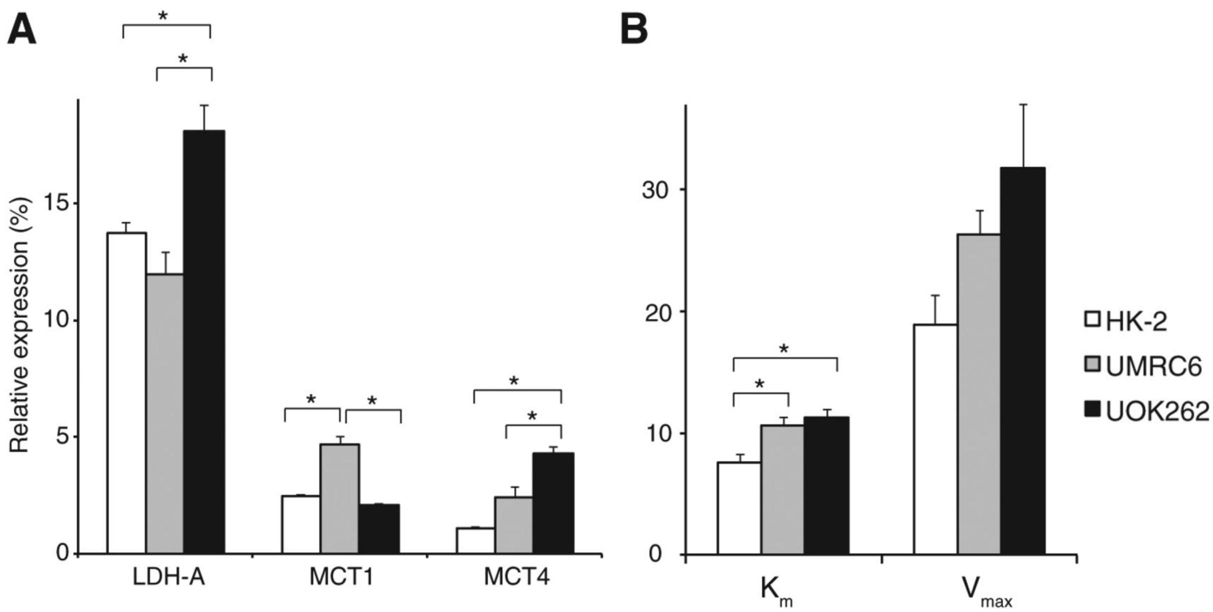


Figure 4.5: Analysis of relevant enzyme expression/activity and transporter expression in the 3 renal cell lines. (**a**) mRNA expression of lactate dehydrogenase A (LDHA) and monocarboxylate transporters 1 and 4 (MCT1 and MCT4), relative to internal β-actin expression, in the 3 cell lines (N = 6 each). (**b**) LDH activity as measured by $K_m$ (μmols pyruvate per $10^6$ cells) and $V_{max}$ (μmols NADH $sec^{-1}$ per $10^6$ cells) in the 3 cell lines (N = 6 each). All values are reported as mean ± std. err. * denotes significant difference ($p < 0.05$).

The higher hyperpolarized pyruvate-to-lactate flux in UMRC6 cells, as compared to UOK262, was likely due, in part, to the higher MCT1 expression rather than the lactate pool size in the UMRC6 cells, as both the steady-state and 24 hour labeling data showed lower lactate pool size in the UMRC6 cells (Figure 4.1b and Figure 4.2e). Importantly, the differential expression of MCT4 may explain the apparent discrepancy between the real time hyperpolarized pyruvate-to-lactate flux and the 24 hr labeling of lactate in the UOK262 cells compared to the UMRC6 cells. The UOK262 cells have an almost two-fold higher MCT4 expression compared to the UMRC6 cells, suggesting that they likely have more rapid MCT4-mediated export of lactate out of the cells. Rapid lactate efflux is essential for maintaining a neutral intracellular pH, and a high rate of glycolysis and lactate production over time. In contrast, UMRC6 cells have lower MCT4 expression, and likely slower rate of lactate export. Although UMRC6 cells have higher MCT1, these cells would be less able to maintain a high rate of lactate production over time due to buildup of intracellular lactate. Therefore, while the real time flux of pyruvate to lactate during the timeframe of the hyperpolarized experiment was lower in the UOK262 cells than the UMRC6 cells, the higher MCT4 expression in the UOK262 cells likely resulted in more rapid lactate efflux and accounted for the significantly higher $^{13}$C labeled lactate accumulated in the medium in the 24 hr labeling experiment. Over time, the large amount of labeled lactate accumulated in the medium of UOK262 cells likely diffused back into the cells down a gradient, and may explain the higher intracellular labeled lactate in the UOK262 cells compared to the UMRC6 cells. We postulate that, while such diffusion of lactate back into the cells may reduce further generation of labeled lactate, this process occurs after a large amount of lactate has already accumulated in the medium of the UOK262 cells. This accumulation of medium lactate and diffusion back into the UOK262 cells were likely accentuated in the 2D cell cultures where the extracellular lactate was not removed, in contrast to the bioreactor where the medium was continuously exchanged.

It is also important to note that while MCT1 may affect the hyperpolarized lactate signal (both the intracellular and extracellular hyperpolarized lactate) if it were the rate-limiting step in the pyruvate-to-lactate flux, the relative proportion of the intracellular versus extracellular hyperpolarized lactate would be determined by MCT4, which modulates the lactate efflux. Additionally, lactate efflux in general is not expected to be significantly affected by MCT1, since most of the lactate produced in the cells is derived from glucose (transported via GLUT1) rather than pyruvate (transported via MCT1) uptake into the cells.

### 4.4.5 Flow-Rate Modulation Affects Hyperpolarized $^{13}$C Flux

We then performed a second set of hyperpolarized MR experiments using different flow rates in the bioreactor in order to investigate the real-time lactate efflux rate in the two RCC cell lines. At high flow rates, the extracellular lactate will more likely flow out of the NMR coils sensitive volume and will not contribute to the MR signal, thereby decreasing the observed pyruvate-to-lactate flux (Figure 4.6a). It follows that the relative amount of extracellular lactate (lactate in the medium) of the two RCC cell lines, which reflects the lactate efflux rate, can be inferred from the observed hyperpolarized pyruvate-to-lactate flux at different flow rates. Figure 4.6b shows the pyruvate-to-lactate flux at different flow rates for the two RCC cells. For the UMRC6 cells, the mean observed hyperpolarized pyruvate-to-lactate flux was 0.92 nmol $s^{-1}$ per $10^6$ cells at 1.3 mL $min^{-1}$, 0.90 nmol $s^{-1}$ per $10^6$ cells at 2.5 mL $min^{-1}$, and 0.94 nmol $s^{-1}$ per $10^6$ cells at 3.8 mL $min^{-1}$, all of which were not statistically different from one another. For the UOK262 cells, the mean observed hyperpolarized pyruvate-to-lactate flux was 0.56 nmol $s^{-1}$ per $10^6$ cells at 1.3 mL $min^{-1}$, 0.51 nmol $s^{-1}$ per $10^6$ cells at 2.5 mL $min^{-1}$, and 0.41 nmol $s^{-1}$ per $10^6$ cells at 3.8 mL $min^{-1}$. These observed hyperpolarized pyruvate-to-lactate flux for the UOK262 cells progressively decreased at higher flow rate, with a significant 20% decrease in the flux between the 2.5 mL $min^{-1}$ and 3.8 mL $min^{-1}$ flow rate ($p = 0.01$). At the high flow rate of 3.8 mL $min^{-1}$, the decreased pyruvate-to-lactate flux in the UOK262 cells indicated that these cells had more rapid lactate efflux and higher amount of extracellular lactate, which was readily removed from the NMR-sensitive region at high flow rate. The high flow rate should not have significantly limited the MCT1-mediated pyruvate uptake into the cells. This is because the injected hyperpolarized pyruvate substrate available to the cells was expected to be in excess compared to MCT1, even at the high flow rate of 3.8 mL $min^{-1}$. Indeed, the UMRC6 cells, with two-fold higher expression of MCT1 compared to the UOK262 cells, showed similar hyperpolarized pyruvate-to-lactate flux at all 3 flow rates, indicating that the flow rates did not limit pyruvate uptake. The flow rate should also not have affected the enzymatic conversion of pyruvate to lactate in the cells. Taken together, the hyperpolarized flux data at different flow rates strongly support the notion that the UOK262 cells have increased MCT4-mediated lactate efflux out of the cells.

Additionally, we incubated the UMRC6 and UOK262 cells for 2 hours in medium containing [3-$^{13}$C] pyruvate, and observed $0.47 \pm 0.05$ versus $2.32 \pm 0.27$ µmols per $10^6$ cells of $^{13}$C labeled lactate in the medium of UMRC6 versus UOK262 cells. This $>$ 5-fold increase in the extracellular lactate of the UOK262 cells further verifies that lactate derived from labeled pyruvate is produced and transported out of the cells at a higher rate in the UOK262 cells compared to the UMRC6 cells.

## 4.5 Discussion

There is increasing evidence that RCCs are among those tumors strongly linked to abnormal metabolism, a feature that may be exploited therapeutically. In this work, we investigated the pyruvate metabolism in perfused human RCC cells using a clinically translatable hyperpolarized $^{13}$C MR probe, and interrogated both the biochemical basis of the observed hyperpolarized MR data and its relationship to cancer aggressiveness. We found higher pyruvate-to-lactate flux, consistent with increased glycolysis, in RCC cells compared to normal renal proximal tubule cells. We further noted that a key feature distinguishing the localized UMRC6 from the metastatic UOK262 RCC cells is the lactate efflux rate, and that, importantly, this feature can be noninvasively depicted via real-time monitoring of hyperpolarized $^{13}$C pyruvate-to-lactate flux.

Lactate efflux is predominantly mediated by MCT4, which is a proton-coupled lactate transporter [Kroemer and Pouyssegur, 2008], exporting lactate and $H^+$ in the same direction

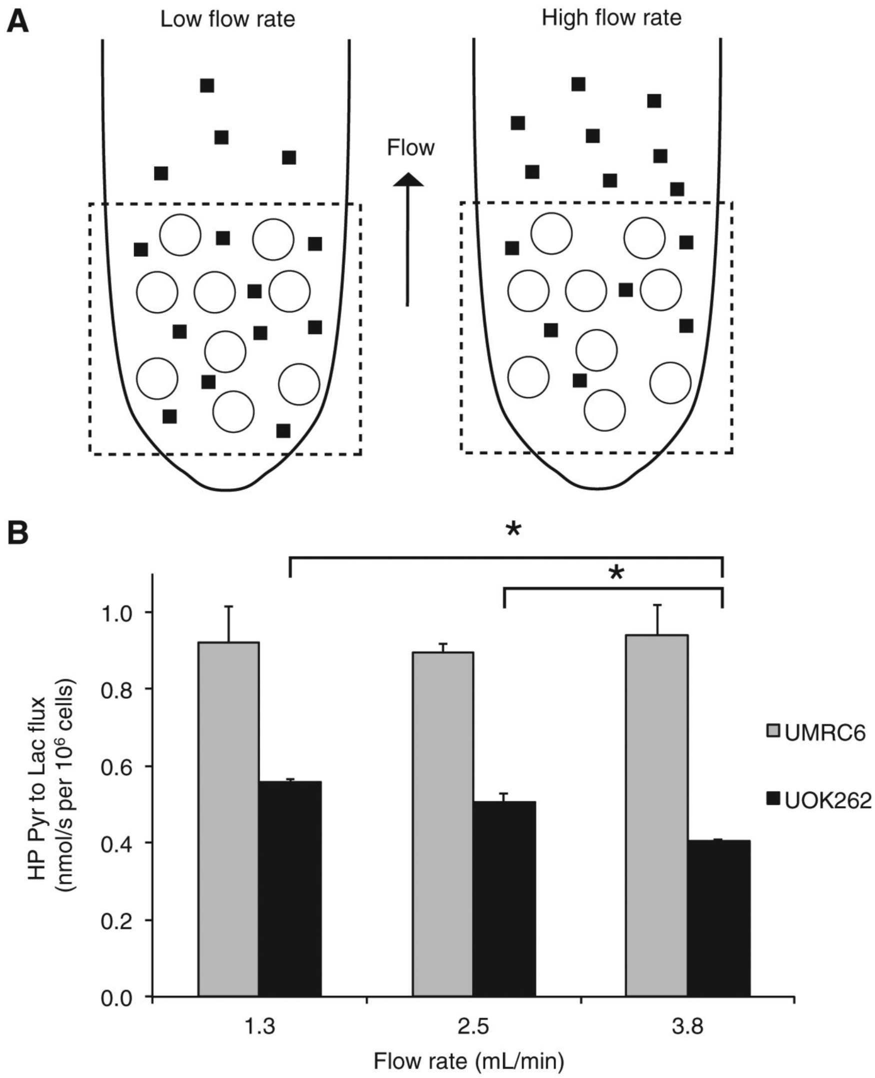


Figure 4.6: Dynamic hyperpolarized $^{13}C$ pyruvate-to-lactate flux in the RCC cells following flow rate modulation in the bioreactor. (**a**) Schematic illustrating the relationship between flow rates and observed hyperpolarized $^{13}C$ pyruvate-to-lactate flux in the bioreactor. At high flow rates, the extracellular lactate will more likely to flow out of the NMR coils sensitive volume and will not contribute to the MR signal, thereby decreasing the observed pyruvate-to-lactate flux. The dotted square represents NMR sensitive region. ◯ represent microspheres containing encapsulated cells. ■ denotes extracellular lactate. (B) HP pyruvate-to-lactate flux of UOK262 and UMRC6 cells at 3 different flow rate (N = 5 each). There is a decreasing trend in observed pyruvate-to-lactate flux with increasing flow rate for UOK262 cells. All values are reported as mean $\pm$ std. err. * denotes significance ($p < 0.05$).

out of the cells. Rapid lactate efflux serves to maintain high levels of glycolysis in cancer cells, and concurrently acidifies the extracellular environment [Gatenby and Gillies, 2004]. Low extracellular pH supports invasion and metastasis, perhaps due to pH-dependent activation of cathepsins and metalloproteinases that degrade extracellular matrix and basement membranes [Swietach *et al.*, 2007]. In this study, we found that the metastatic UOK262 cells have significantly higher MCT4 expression compared to the localized UMRC6 cells, and also have more rapid export of lactate out of the cells. UOK262 cells have mutations in the TCA enzyme FH, which leads to an uncommon and highly aggressive hereditary RCC. However, recent studies have shown that FH mRNA and protein expression are reduced in clear cell RCC, the most common histological variant of kidney cancer, promoting tumor migration and invasion [Sudarshan *et al.*, 2009]. The reduced FH leads to accumulation of hypoxia inducible factor-2 alpha (HIF-2$\alpha$) [Pollard *et al.*, 2005], a transcription factor known to promote renal carcinogenesis in part by up-regulating glycolysis [Semenza, 2007]. Thus, the metabolic changes observed in the UOK262 cells are likely not unique to this particular RCC type, and the MCT4-mediated lactate efflux may be an important determinant of RCC aggressiveness in general. Supporting this hypothesis, a recent study showed that MCT4 protein expression in primary clear cell RCCs was associated with poorer relapse-free survival, and correlated with Fuhrman nuclear grade [Gerlinger *et al.*, 2012]. Additionally, MCT4 knockdown RCC cell lines had reduced intracellular pH, impaired proliferation and increased apoptosis [Gerlinger *et al.*, 2012]. These studies indicate that MCT4 targeting may also be an important strategy for the treatment of RCCs.

We showed that the MCT4-mediated lactate efflux in living cells can be explored noninvasively using hyperpolarized $^{13}$C MR. This was accomplished by monitoring the real time cellular pyruvate-to-lactate fluxes under different flow rates in the bioreactor. While our study utilized an ex vivo system, interrogation of lactate export using hyperpolarized $^{13}$C

MR can be achieved *in vivo*. For example, it is possible to measure the tumoral extracellular or interstitial pH, which in part reflects the amount of exported lactate, using hyperpolarized $^{13}$C bicarbonate MR [Gallagher *et al.*, 2008; Wilson *et al.*, 2010]. Moreover, it is possible to discriminate the local environment of hyperpolarized metabolites using diffusion weighting *in vivo* [Larson *et al.*, 2012; Chen *et al.*, 2012]. Future studies will develop diffusion-weighted hyperpolarized MR that can directly quantify the relative amount of intracellular versus extracellular lactate.

While total lactate levels can also be monitored using $^{1}$H MRS, this approach has limited utility in the metabolic evaluation of renal tumors, particularly in the *in vivo* setting. Lactate and lipid peaks usually overlap such that the assessment of lactate is challenging even when methods for lipid suppression are applied. More importantly, the real time metabolic fluxes, influenced by enzymatic and transporter expression, cannot be captured using $^{1}$H MRS.

## 4.6 Conclusion

In this study, we have demonstrated that hyperpolarized $^{13}$C pyruvate MRS enables real-time observation of differential lactate efflux, mediated by MCT4, in living RCC cells of varying aggressiveness. Importantly, as MCT4 and lactate efflux are implicated in the pathogenesis of many types of cancers, hyperpolarized $^{13}$C MRS has the potential to noninvasively interrogate tumor aggressiveness and treatment efficacy in a broad range of cancers.

## 4.7 Supplemental Content

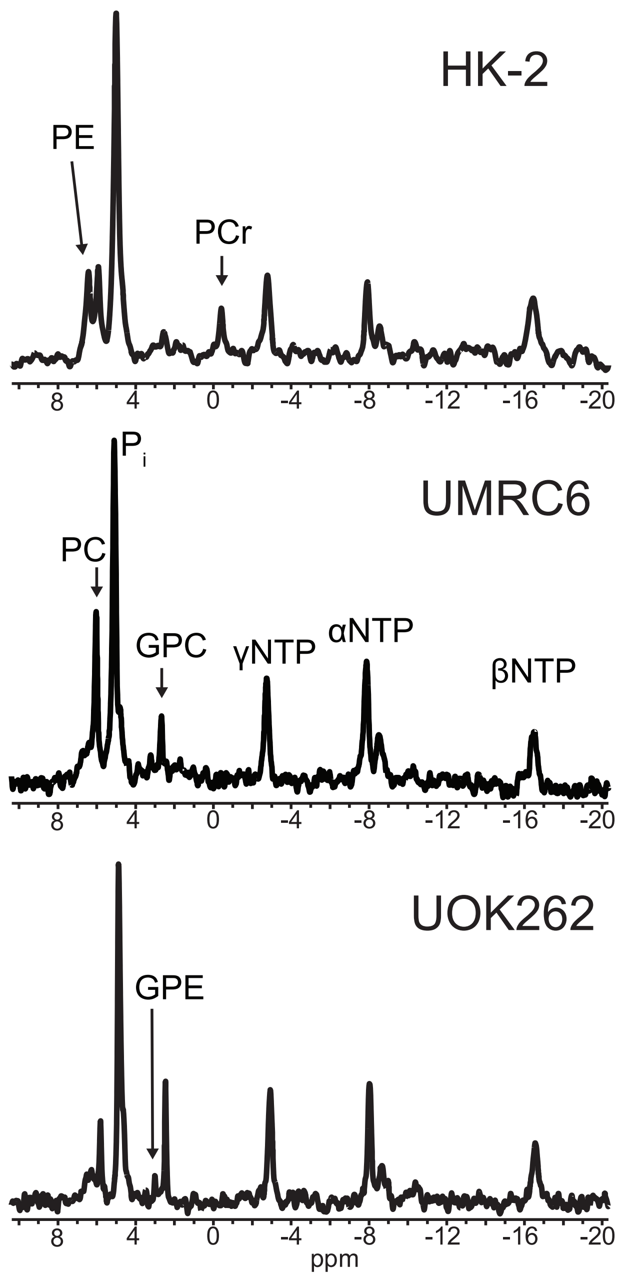


Figure 4.7: Representative $^{31}P$ spectra for each of the 3 renal cell lines acquired in the 10 mm bioreactor (TR 3 s, 1024 averages, 90° flip angle)

Table 4.1: $^{31}$P metabolite chemical shifts (δ) and $T_1$ relaxation times at 11.7 T (202 MHz), measured in living UMRC6 cells within a 10 mm bioreactor.

| Metabolite | δ [ppm] | $T_1$ [s] |
|---|---|---|
| PC | 5.72 | 2.46 ± 0.65 |
| $P_i$ | 4.54 | 3.82 ± 0.68 |
| GPE | 3.01 | 2.57 ± 1.41 |
| GPC | 2.46 | 2.73 ± 0.75 |
| γ-NTP | -2.94 | 0.40 ± 0.07 |
| α-NTP | -8.03 | 0.51 ± 0.07 |
| NAD(H) + UDP | -8.69 | 0.92 ± 0.16 |
| UDP only | -10.43 | 0.67 ± 0.25 |
| β-NTP | -16.52 | 0.47 ± 0.11 |

PC: phosphocholine; $P_i$: inorganic phosphate; GPE: glycerophosphoethanolamine; GPC: glycerophosphocholine; NTP: nucleotide triphosphate resonances; NAD(H): nicotinamide adenine diphosphate; UDP-sugars: uridine diphosphate sugars

Table 4.2: Analysis of hyperpolarized $^{13}$C lactate curve dynamics in 10 mm bioreactors for perfused HK2, UMRC6 and UOK262 cells at a flow rate of 2.5 mL min$^{-1}$.

| Cells | AUC$^{\dagger\ddagger\pounds}$ | Time to max$^{\dagger\pounds}$ [s] | $1^{st}$ inflection$^{\dagger\pounds}$ [s] | $2^{nd}$ inflection$^{\dagger\pounds}$ [s] | Peak width$^{\dagger\pounds}$ [s] |
|---|---|---|---|---|---|
| HK2 | 162 ± 7 | 57.3 ± 3.4 | 28.4 ± 0.2 | 98.4 ± 6.8 | 70.0 ± 6.7 |
| UMRC6 | 382 ± 18 | 40.0 ± 0.7 | 21.5 ± 0.7 | 61.9 ± 1.7 | 40.5 ± 1.0 |
| UOK262 | 266 ± 13 | 53.6 ± 1.7 | 28.7 ± 0.1 | 89.8 ± 2.6 | 61.1 ± 2.5 |

AUC: Area Under the Curve; $1^{st}$ and $2^{nd}$ inflections: the times at which the curve changes shape; Peak width: difference in time between the inflection points.

† $p < 0.005$ HK2 *vs.* UMRC6; ‡ $p < 0.005$ HK2 *vs.* UOK262; £ $p < 0.005$ UMRC6 *vs.* UOK262

# Chapter 5

# Diffusion MR of Hyperpolarized $^{13}$C Molecules in Solution

## 5.1 Chapter Overview

In this chapter, we combine the high MR signal enhancement achieved using dissolution dynamic nuclear polarization (DNP) with a pulsed gradient double spin echo diffusion MR sequence to rapidly and accurately measure the diffusion coefficients of various hyperpolarized $^{13}$C molecules in solution. Furthermore, with a diffusion weighted imaging sequence we generate diffusion coefficient maps of multiple hyperpolarized metabolites simultaneously. While hyperpolarized experiments can measure rapid, non-equilibrium processes by avoiding signal averaging, continuous signal loss due to longitudinal relaxation ($T_1$) complicates quantification. By correcting for this signal loss, we demonstrate the feasibility of using hyperpolarized $^{13}$C diffusion weighted MR to accurately measure real-time (seconds) molecular transport phenomena. Applications of this methodology used later in this dissertation include rapidly measuring cellular membrane transport and *in vivo* metabolite distributions with apparent diffusion coefficient (ADC) maps. Both of these could be used for cancer staging by assessing the localization of hyperpolarized $^{13}$C lactate, given that several studies have shown that aggressive and highly metastatic tumors rapidly transport lactate out of cells.

## 5.2 Introduction

Diffusion MR has a variety of applications in solution, and is central to modern biomedical imaging. Many variations of the pulsed gradient spin echo experiment originally developed by Stejskal and Tanner [Stejskal and Tanner, 1965] have been used to measure diffusion coefficients [Price *et al.*, 1999], compartment size [Codd and Callaghan, 1999], as well as molecular transport [Benga *et al.*, 1993] and molecular exchange [Price *et al.*, 2002]. Diffusion measurements often suffer from low sensitivity and require time-intensive signal averaging to obtain a sufficient signal to noise ratio (SNR) for reliable measurements. Long experimental times also require samples to be at steady state, since any signal perturbations other than molecular motion can skew measured diffusion constants. Since sensitivity has traditionally been limiting for diffusion MR experiments, $^{1}$H has been used more frequently than other spin-1/2 nuclei (e.g, $^{13}$C, $^{15}$N, $^{31}$P) that have low gyromagnetic ratios and natural abundance. Hyperpolarized gasses, most notably $^{3}$He and $^{129}$Xe, circumvent this low signal problem and allow for rapid diffusion measurements [Patyal *et al.*, 1997; Chen *et al.*, 1999]. Unfortunately, these inert gasses are not typically involved in chemical reactions or metabolic pathways of interest.

In this chapter, we combine diffusion MR with dissolution dynamic nuclear polarization (DNP) [Ardenkjær-Larsen *et al.*, 2003] hyperpolarized $^{13}$C and thereby lay the foundation for making real-time, non-equilibrium diffusion measurements. The signal gain provided by hyperpolarization and the chemical shift sensitivity of $^{13}$C will allow for diffusion studies to be carried-out on the time scale of chemical reactions [Wilson *et al.*, 2009] or metabolic processes [Golman *et al.*, 2006]. Since both diffusion MR and hyperpolarized experiments are characterized by a time-decay constant, the experimental setup for diffusion measurements of hyperpolarized molecules must allow for the quantitative separation of these two factors.

Dissolution DNP is typically used to polarize $^{13}$C nuclei with long spin-lattice ($T_1$) relaxation times (tens of seconds) and, upon dissolution, a solution of hyperpolarized spins is obtained. A conventional NMR spectrum of this solution can exhibit a signal enhancement of greater than 10,000-fold [Ardenkjær-Larsen *et al.*, 2003] when compared to a spectrum of a similar solution at its thermal equilibrium polarization in a typical magnetic field of an NMR at ambient temperature. Hyperpolarized [1-$^{13}$C] pyruvate has been used most extensively to study various cancers by monitoring [1-$^{13}$C] lactate generation [Albers *et al.*, 2008; Day *et al.*, 2007]. Additionally, numerous other molecules have also been polarized to monitor other reactions and metabolic processes [Keshari *et al.*, 2009; Gabellieri *et al.*, 2008; Witney *et al.*, 2010; Keshari *et al.*, 2011] either as single agents or in combination [Wilson *et al.*, 2010]. The challenge in combining hyperpolarization with diffusion MR lies in the non-renewable nature of the hyperpolarized spin state and its fast decay, where small imperfections in data acquisition can lead to large NMR signal modulations and thereby increase diffusion measurement error. When correctly implemented, the merging of these two techniques will provide significant advances in numerous fields, including molecular biding, cellular transport studies and in vivo diffusion weighted MRI.

## 5.3 Methods

### 5.3.1 Data Acquisition

All MR studies were performed on a 14.1 T Varian INOVA spectrometer (600 MHz $^1H$/150 MHz $^{13}C$) micro-imaging system (Agilent Technologies), equipped with a 10 mm broadband probe and 100 G cm$^{-1}$ gradients. Probe temperature was controlled at 27°C.

A pulsed gradient double spin echo sequence was used for all experiments (Figure 5.1). A 10° excitation pulse with a pair of adiabatic 180° refocusing pulses. This pulse sequence is particularly suited for quantitative hyperpolarized diffusion experiments because the adiabatic pulses are insensitive to transmitter-gain calibrations and the pair of 180° refocusing pulses realign the magnetization with the main magnetic field, thereby avoiding increased signal loss [Cunningham *et al.*, 2007]. Since hyperpolarized signal is non-renewable, any small errors in a pulse sequence will propagate throughout an entire experiment and could complicate quantification. Diffusion measurements were interleaved with measurements used to determine the apparent $T_1$. Unless indicated otherwise, data were acquired every second (TR = 1 s) for 150 seconds, with an echo time (TE) of 50 ms. A crusher gradient (4 G cm$^{-1}$, 4 ms) was applied to saturate remaining transverse magnetization between every acquisition of the experiment.

Diffusion gradient pulses were positioned symmetrically around both 180° pulses with a gradient pulse duration ($\delta$) of 5 ms and a gradient pulse separation ($\Delta$) of 20 ms. By applying a range of gradient strengths (2 – 60 G cm$^{-1}$, in transverse orientation) spectra with different $b$-values (2 – 1500 s mm$^{-2}$) were obtained. To utilize the high SNR at the beginning of hyperpolarized experiments, $b$-values were arrayed from high to low. The $b$-

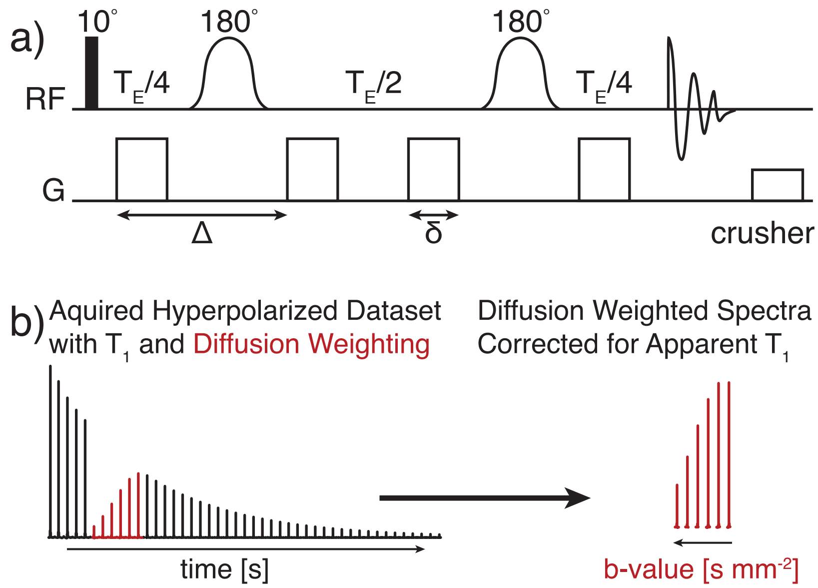


Figure 5.1: (**a**) The pulsed gradient double spin echo pulse sequence used for hyperpolarized diffusion experiments, with a 10° excitation pulse and adiabatic 180° pulses. (**b**) Representative spectra for which the apparent $T_1$ (*black*) and hyperpolarized diffusion measurements (*red*) are interleaved. Correcting the hyperpolarized diffusion weighted spectra for the $T_1$ enables an accurate calculation of diffusion coefficient for the hyperpolarized molecules.

value for two square gradient pairs [Nicolay *et al.*, 2001] is defined by

$$b = 2\,\gamma^2\,G^2\,\delta^2\,(\Delta - \delta/3) \tag{5.1}$$

with $\gamma$ being the gyromagnetic ratio for $^{13}$C. Spectra used to fit the apparent $T_1$ had a pair of crusher gradients (2 G cm$^{-1}$, 5 ms) around each of the adiabatic 180° pulses.

### 5.3.2 Hyperpolarization and Dissolution

Samples were polarized on a Hypersense (Oxford Instruments) and dissolved into 2 mL of a dissolution buffer, resulting in a final temperature of 27°C. From this solution, 0.8 mL were rapidly transferred into an 8 mm susceptibility matched NMR tube (Shigemi Inc.), which was manually inserted into the bore of the spectrometer. Polarizations were measured by comparing the signal of the hyperpolarized sample with that of the thermally polarized sample. Convective effects were minimized by heating the spectrometers bore to 27°C (same as the sample temperature), by using a small sample volume that would reduce temperature gradients across the sample and by using diffusion gradients in the transverse plane (e.g., $G_x$). Additionally, the comparison of hyperpolarized $^{13}$C urea, measured in several seconds, with thermally polarized $^{13}$C urea, measured over several minutes, confirms the ability to minimize convective effects in our diffusion measurements.

### 5.3.3 Thermal and Hyperpolarized $^{13}$C Urea

Hyperpolarized $^{13}$C urea diffusion coefficients were compared to those of $^{13}$C urea at its thermal equilibrium polarization. Thermally polarized $^{13}$C urea experiments were done on a 1 M solution, doped with 2 mM gadolinium to decrease the $T_1$ and thereby shorten the experiment time. These thermally polarized experiments used a 90° excitation pulse and a TR of 10 s. The gradient strengths and thus $b$-values were the same as those used for the hyperpolarized experiments. The $^{13}$C urea DNP sample was prepped according to a previously published protocol [Wilson *et al.*, 2010]. Hyperpolarized $^{13}$C urea was dissolved in 2 mL deionized water and gave a final concentration of 16 mM.

### 5.3.4 Simulation

We simulated the effects of both the apparent $T_1$ and the total diffusion measurement time on the accuracy of the calculated diffusion coefficient, using urea as our test case. With a previously published diffusion coefficient for urea [Gosting and Akeley, 1952], adjusted to the temperature of our experiments, and the $T_1$ measured with a simple pulse-and-acquire experiment, we generated simulation diffusion data for hyperpolarized urea. Then, we modeled the correction of this simulation data using apparent $T_1$s that deviated from the true $T_1$ by $\pm$ 25% and with various total diffusion measurement times.

### 5.3.5 Hyperpolarized Diffusion of $^{13}$C Pyruvate and $^{13}$C Lactate

Both [1-$^{13}$C] pyruvate and [1-$^{13}$C] lactate were prepared according to previously published protocols [Wilson *et al.*, 2010; Chen *et al.*, 2008]. The dissolution solution was a 50 mM phosphate buffer and the final concentration of these experiments was 11 mM.

### 5.3.6 Secondary Hyperpolarization with [1,1-$^{13}$C] Acetic Anhydride

Both protonated and perdeuterated [1,1-$^{13}$C] acetic anhydride were prepped according to a previously published protocol [Wilson *et al.*, 2009]. Signal enhancements after the chemical reaction were similar to those previously reported [Wilson *et al.*, 2009]. In separate experiments, acetic anhydride was reacted with glycine, triglycine or RGD (arginine-glycine-aspartic acid). The dissolution solution for hyperpolarized [1,1-$^{13}$C] acetic anhydride contained 3 equivalents of the amino acid or peptide of interest and 2 equivalents of sodium hydroxide. This fast reaction resulted in hyperpolarized $^{13}$C acetate and the acetylated version of the amino acid or peptide of interest. The absence of the [1,1-$^{13}$C] acetic anhydride in all spectra indicated that the reaction had gone to completion.

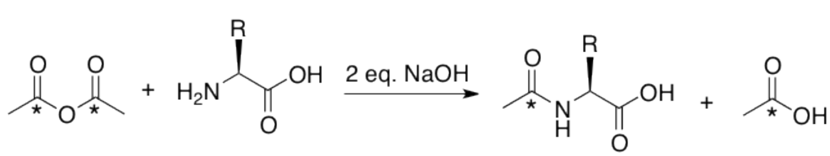


Figure 5.2: The mechanism for secondary hyperpolarization of amino acids using hyperpolarized [1,1-$^{13}$C] acetic anhydride

Diffusion coefficients of both [1-$^{13}$C] acetate and [1-$^{13}$C,d$_3$] acetate were measured at 26 mM while those for N-[acetyl-1-$^{13}$C] glycine and N-[acetyl-1-$^{13}$C,d$_3$] triglycine were done at a hyperpolarized concentration of 26 mM and a total concentration of 78 mM (since the amino acid/peptide was added at 3 times excess).

Diffusion coefficients for N-[acetyl-1-$^{13}$C,d$_3$] RGD were measured at a hyperpolarized concentration of 52 mM and a total concentration of 156 mM. For the N-[acetyl-1-$^{13}$C,d$_3$] RGD experiments, the TR = 0.5 s, $\delta = 10$ ms and $b$-values ranged from 150 – 5,400 s mm$^{-2}$. Additionally, the diffusion coefficient of N-[acetyl-1-$^{13}$C,d$_3$] RGD at its thermal equilibrium polarization was measured by using 15 averages per spectra at each $b$-value and required 12 h to complete. We calculated this diffusion coefficient to be $0.47 \times 10^{-3}$ mm$^2$ s$^{-1}$ (n = 1).

### 5.3.7 NMR Data Analysis

All spectra were zero-filled to 8,000 points, line broadened 10 Hz and phase corrected (zero order). Integrated peak height and intensity were corrected for multiple excitations and the apparent $T_1$ was determined by fitting the exponential decay of the corrected signal. Subsequently, all diffusion data were also corrected for the apparent $T_1$ and for multiple excitations. From this, the diffusion coefficients ($D$) were determined by fitting the exponential $S/S_0 = \exp(-b\,D)$, where $b$ are the $b$-values at each diffusion spectra. Six different diffusion weighted spectra were acquired for each dataset. $S_0$ is the hyperpolarized signal without diffusion weighting ($b$ = 2 s mm$^{-2}$), but corrected both for the apparent $T_1$ and multiple excitations.

All data are presented as mean ± SD, n = 3. Statistical comparisons were made with Student's t-test and significance was considered to be at a p-value $< 0.05$.

### 5.3.8 Diffusion Weighted MRI

Diffusion weighted imaging was done with a pulsed gradient double spin echo and a concentric echo planar imaging (EPI) readout. Hyperpolarized metabolites were excited with a 10° frequency specific Shinnar-Le Roux (SLR) pulse. During the 1 s TR, $^{13}$C urea, $^{13}$C pyruvate and $^{13}$C lactate were imaged with a field of view (FOV) of 25 × 25 mm (16 × 16 points). Diffusion coefficients maps were fit on a per-voxel basis in a region of interest (ROI) and are reported as ± SD. Otherwise, all pulse sequence parameters and data analysis methods were identical to those discussed above.

## 5.4 Results and Discussion

Hyperpolarized experiments consisted of interleaved acquisitions to measure both the hyperpolarized molecules apparent $T_1$ and its diffusion coefficient. Diffusion acquisitions with increasing gradient strengths (Figure 5.1b, *red lines*) were interspersed with $T_1$ acquisitions with small crusher gradients (Figure 5.1b, *black lines*). Diffusion coefficients were calculated by fitting the diffusion spectra with the following equation:

$$S = S_o \exp(-bD) \exp(-t/T_1) \exp(TE/T_2) \cos^n(\theta) \tag{5.2}$$

where $D$ is the diffusion coefficient (mm$^2$ s$^{-1}$) and $b$ is the diffusion weighting. The cosine term corrects the data for multiple excitations ($n$) of the hyperpolarized magnetization with a flip angle $\theta$. Individual spectra are corrected for $T_1$-dependent signal loss based on a per-time basis ($t$). Since the TE (50 ms) for all experiments was kept constant, any $T_2$-weighting was a constant across all spectra and datasets and therefore was not needed to calculate the reported diffusion coefficients.

This approach for measuring diffusion coefficients relies on correcting for the effects of $T_1$ relaxation since hyperpolarized experiments are characterized by a $T_1$-dependant signal loss. While determining the $T_1$ of a hyperpolarized molecule in solution is trivial, accurate $T_1$ measurements become more difficult in complex environments, such as with molecular binding or in tissue.

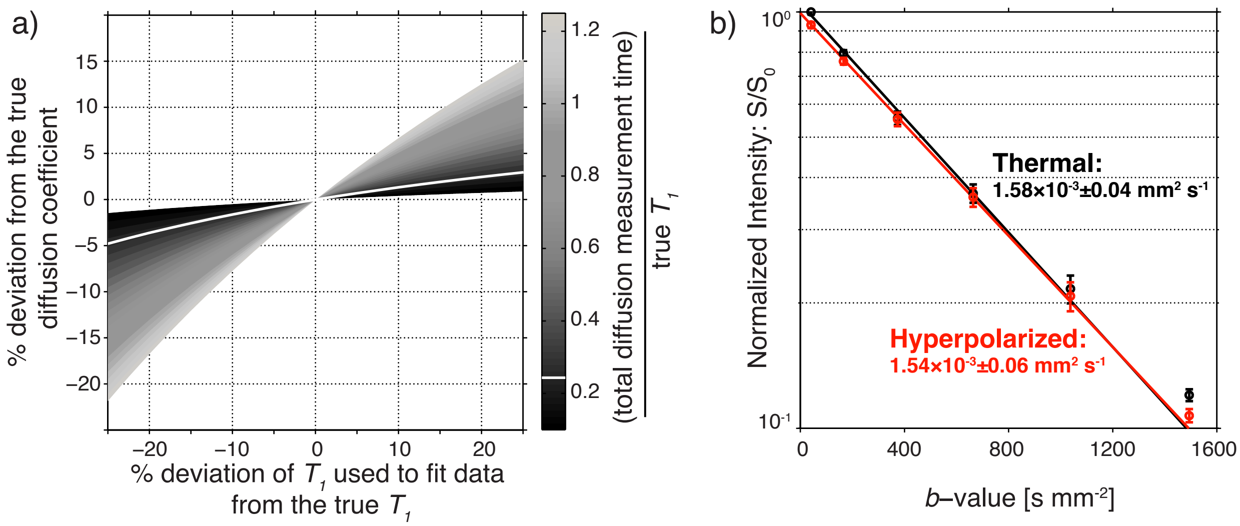


Figure 5.3: (**a**) A simulation for hyperpolarized $^{13}$C urea shows how a short total diffusion measurement time relative to the $T_1$ makes calculations of the diffusion coefficient less sensitive to the apparent $T_1$ accuracy. The *white line* represents the (total diffusion measurement time)/true $T_1$ ratio used in our hyperpolarized $^{13}$C urea experiments, where errors of up to $\pm$ 25% in apparent $T_1$ only result in less than 5% errors in the diffusion coefficient. (**b**) Diffusion coefficients of $^{13}$C urea at 27°C, measured using thermal equilibrium polarization and hyperpolarization. *b*-value is a measure of the degree of diffusion weighting.

The simulation presented in Figure 5.3a illustrates the dependence of the calculated diffusion coefficient on both the apparent $T_1$ of the hyperpolarized spin used to correct the dataset and the total diffusion measurement time required for the experiment. As the ratio of the total diffusion measurement time to the true relaxation time decreases (i.e., darker regions in Figure 5.3a), the calculated diffusion coefficient becomes less sensitive to errors in the apparent $T_1$ used to correct the hyperpolarized diffusion dataset. Since long $T_1$

carbon species are typically used in hyperpolarized experiments (on the order of 30–60 s), the diffusion measurement time can be significantly shorter than signal loss due to relaxation. The acquisition is also further accelerated due to the increased signal intensity afforded by hyperpolarization of the molecule of interest. Furthermore, while the decay nature of hyperpolarized signal complicates these experiments, within experimental tolerances, this can be addressed to generate reliable diffusion measurements.

Table 5.1: Diffusion coefficients ($D$) and relaxation times ($T_1$) of hyperpolarized $^{13}$C molecules measured in aqueous solution

| Molecule | MW [g mol$^{-1}$] | $T_1$ [s]$^a$ | $D$ [$\times 10^{-3}$ mm$^2$ s$^{-1}$]$^b$ | Literature $D$ [$\times 10^{-3}$ mm$^2$ s$^{-1}$]$^c$ |
|---|---|---|---|---|
| $^{13}$C urea | 61.05 | 35.3±2.6 | 1.54±0.06 | 1.45† |
| [1-$^{13}$C] acetate | 61.04 | 46.2±0.7 | 1.15±0.03 | 1.15‡ |
| [1-$^{13}$C,d$_3$] acetate | 64.04 | 49.9±1.7 | 1.13±0.02 | – |
| [1-$^{13}$C] pyruvate | 89.05 | 43.8±3.3 | 1.12±0.04 | – |
| [1-$^{13}$C] lactate | 91.07 | 32.3±0.7 | 1.00±0.01 | 1.12§ |
| N-[acetyl-1-$^{13}$C] glycine | 118.10 | 16.9±0.8 | 0.87±0.07 | 1.11*,# |
| N-[acetyl-1-$^{13}$C,d$_3$] triglycine | 232.20 | 9.9±0.7 | 0.6±0.04 | 0.70*,£ |
| N-[acetyl-1-$^{13}$C,d$_3$] RGD | 391.37 | 5.4±0.8 | 0.49±0.03$^d$ | – |

*a*) $T_1$ relaxation times are at 14.1 T/150 MHz for $^{13}$C. *b*) Measurements at 27°C. *c*) Literature references cite diffusion coefficients of either exactly the compound or a similar compound (marked with *), e.g., the diffusion coefficient for triglycine as compared to N-acetyl-triglycine. All literature values were adjusted for temperature using the Stokes-Einstein equation. *d*) A 12 hr diffusion acquisition of thermally polarized N-acetyl-RGD ($0.47 \times 10^{-3}$ mm$^2$ s$^{-1}$) corresponds with this rapid hyperpolarized measurement.

†[Gosting and Akeley, 1952], ‡[Kida and Uedaira, 1977], §[Lundberg and Kuchel, 1997], #[Longsworth, 1953], £[Longsworth, 1953]

To confirm our ability to accurately measure the diffusion coefficient of a hyperpolarized molecule, we compared measurements of $^{13}$C urea both at its thermal equilibrium polarization and hyperpolarized, polarized to 8.4% ± 0.6. As seen in Figure 5.3b the diffusion coefficients of thermally polarized and hyperpolarized $^{13}$C urea were $1.58 \times 10^{-3} \pm 0.04$ and $1.54 \times 10^{-3} \pm 0.06$ mm$^2$ s$^{-1}$, respectively, and not statistically different (p-value = 0.20). In a similar fashion, we measured the diffusion coefficients of $^{13}C$ pyruvate and $^{13}C$ lactate (Table 5.1), polarized to 18.5% ± 0.7 and 2.9% ± 0.5, respectively.

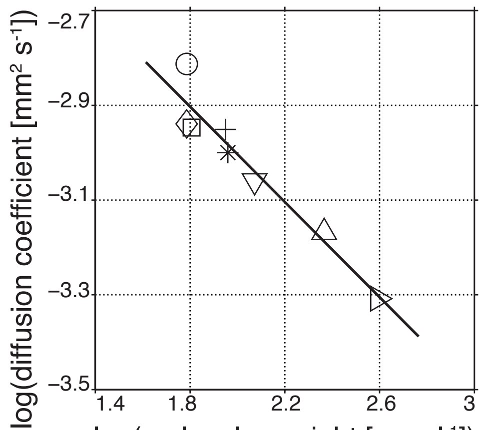


Figure 5.4: This plot shows the relationship between a molecule's molecular weight and its diffusion coefficient. The data are presented in Table 5.1. ○ $^{13}C$ urea, ◇ [1-$^{13}C$] acetate, □ [1-$^{13}C$,$d_3$] acetate, + [1-$^{13}C$] pyruvate, ∗ [1-$^{13}C$] lactate, ▽ N-[acetyl-1-$^{13}C$] glycine, △ N-[acetyl-1-$^{13}C$,$d_3$] triglycine, ▷ N-[acetyl-1-$^{13}C$,$d_3$] RGD.

We extended the technique developed here to measuring diffusion coefficients of larger molecules. Utilizing secondary hyperpolarization [Wilson *et al.*, 2009], we generated hyperpolarized amino acids and peptides, achieving signal enhancements similar to those previously reported. The technique reacts hyperpolarized [1,1-$^{13}C$] acetic anhydride (polarized to 2.4% ± 0.2) with nucleophilic amine termini. In this manner, we measured the diffusion coefficients of $^{13}C$ acetate and $^{13}C$ N-acetyl-glycine at 27°C in aqueous solution (Table 5.1). To lengthen the $T_1$ of larger secondarily hyperpolarized peptides, we polarized perdeuterated [1,1-$^{13}C$,$d_6$] acetic anhydride (polarized to 2.9 % ± 0.5), which avoids cross-relaxation between the carbonyl carbon and methyl protons. Reacting this with triglycine, we measured the diffusion coefficients of perdeuterated $^{13}C$ acetate and $^{13}C$ N-acetyl-triglycine (Table 5.1). Finally, we reacted the cell integrin adhesion peptide arginine-glycine-aspartic acid peptide (RGD) with perdueterated $^{13}C$ acetic anhydride to measure the diffusion coefficient of $^{13}C$ N-acetyl-

RGD (Table 5.1). This experiment shows the feasibility of using hyperpolarized diffusion measurements to studying the translational motion and interaction of biologically relevant small peptides.

In the regime of small molecules, a linear relationship has been observed between molecular weight and diffusion coefficients [Chen *et al.*, 1995]. As expected, this phenomenon is observed in the case of hyperpolarized molecules of varying molecular weights (Figure 5.4), further validating our approach.

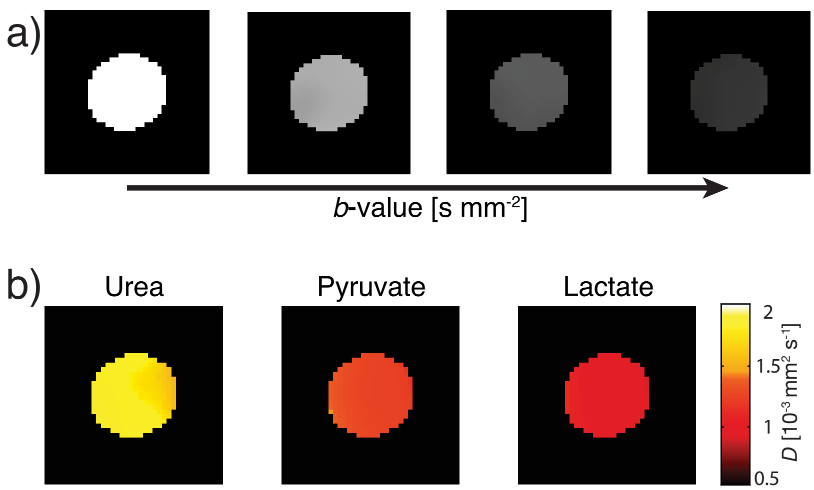


Figure 5.5: Diffusion weighted MRI of three hyperpolarized metabolites, acquired simultaneously. (**a**) Representative $T_1$ corrected diffusion weighted images with increasing diffusion weighting ($b$-values 1.7, 173, 693 and 1560 s mm$^{-2}$) used to simultaneously generate diffusion coefficient maps (**b**) of $^{13}$C urea, $^{13}$C pyruvate and $^{13}$C lactate.

To demonstrate the feasibility of using diffusion MR of hyperpolarized metabolites in the clinical setting, we added a concentric echo planar imaging readout to the pulsed gradient double spin echo to generate diffusion coefficient maps (Figure 5.5). Here, the diffusion coefficient maps of hyperpolarized $^{13}$C urea ($1.55 \times 10^{-3} \pm 0.07$ mm$^2$ s$^{-1}$), $^{13}$C pyruvate ($1.12 \times 10^{-3} \pm 0.06$ mm$^2$ s$^{-1}$) and $^{13}$C lactate ($0.98 \times 10^{-3} \pm 0.04$ mm$^2$ s$^{-1}$), measured simultaneously with frequency specific excitation pulses, match values acquired with hyperpolarized diffusion NMR.

Hyperpolarized diffusion NMR can allow for rapid measurements of real-time, non-equilibrium chemical process. For example, molecular binding can be measured using a pulsed gradient spin echo approach [Fielding, 2007]. These experiments require time intensive signal averaging and today commonly utilize signal enhancement via the nuclear Overhauser effect (NOE) [Chen and Shapiro, 1998]. Conversely, hyperpolarized diffusion NMR would greatly reduce the measurement times of these experiments, would not be complicated by NOE polarization transfers [Chen and Shapiro, 1999] when using $^{13}$C and would allow for the simultaneous observation of any changes in chemical shifts. However, even these relatively rapid acquisition times with hyperpolarized diffusion NMR experiments are still too slow for measuring some sugar-protein binding mechanisms [Nilsson *et al.*, 2008].

Like non-steady state chemical kinetics, assessment of metabolic flux requires rapid measurement, since metabolism occurs on the order of seconds. Closely associated with a metabolic pathways activity is the cellular membrane transport of these metabolites. Prior diffusion NMR studies took advantage of differences in metabolite diffusivity in the intra- and extracellular environments to measure intracellular metabolite concentrations [Van Zijl *et al.*, 1991]. This approach used diffusion NMR as a filter, but because of the need for signal averaging, it could solely measure steady state metabolites. The hyperpolarized diffusion NMR technique developed here can be extended for use as a diffusion filter to measure real-time membrane transport of various hyperpolarized metabolites. For example, the intra- versus extracellular localization of the hyperpolarized $^{13}$C lactate produced in cancer cells could help elucidate aggressiveness and metastatic potential [Bhujwalla *et al.*, 2002]. Of course, hyperpolarized diffusion filters could be used to measure cellular transport from a variety of metabolites, especially when applying these studies to bioreactors [Keshari *et al.*, 2010].

While diffusion weighted MRI has become a standard clinical tool for assessing anatomy, combining it with hyperpolarized substrates has the potential to inform on metabolism localization in the cellular microenvironment. Larson et al. recently developed a super stimulated echo sequence to suppress vascular hyperpolarized $^{13}$C signal [Larson *et al.*, 2012]. By only imaging hyperpolarized $^{13}$C lactate in the tissue, this technique improved the delineation of primary tumors *in vivo*. Extending this technique to create a diffusion filter could allow for measurement of both the generation of hyperpolarized metabolites and their tissue distribution, similar to how cell studies would elucidate membrane transport kinetics. Furthermore, hyperpolarized $^{13}$C diffusion MRI could measure apparent diffusion coefficient (ADC) maps for hyperpolarized metabolites. Noteworthy is that such ADC maps are magnetic field independent, a particular benefit since hyperpolarized $^{13}$C signal intensities change according to initial polarization levels and magnetic field dependent $T_1$ relaxation.

## 5.5 Conclusion

In summary, we present the foundations for carrying out fast diffusion studies with dissolution DNP hyperpolarized $^{13}$C molecules. The SNR gain provided by hyperpolarization and the chemical shift sensitivity of $^{13}$C allows for diffusion studies to be carried-out on the time scale of chemical reactions or metabolic processes, where both products and reactants can be measured simultaneously. Our technique demonstrates how to robustly sample dynamic hyperpolarized magnetization in order to obtain quantitatively accurate diffusion measurements. Given this, hyperpolarized $^{13}$C diffusion MR has far reaching applicability in areas such as binding studies, metabolomics, clinical diagnoses and many more.

# Chapter 6

# Complete Separation of Extra- and Intracellular Hyperpolarized $^{13}$C Metabolites Using Diffusion Weighted MR

## 6.1 Chapter Overview

This chapter uses diffusion weighted MR to completely separate the extra- and intracelluar hyperpolarized $^{13}$C metabolite signals. The techniques developed in Chapter 5 are adapted here to measure the extra- and intracellular diffusion coefficients of these metabolites. Furthermore, in separate experiments we use alternating low and high diffusion weighting gradients to monitor the total and intracellular hyperpolarized $^{13}$C metabolite signals in time, allowing for a real-time assessment of their relative extra- and intracellular pool sizes. These experiments demonstrated that lactate efflux may play an important role in the hyperpolarized $^{13}$C lactate signal acquired during metabolism *in vivo*.

It has been established that metastatic cancers overexpress the monocarboxylate transporters 4 (MCT4). MCT4s facilitate lactate efflux from the cytoplasm, and coupled with the cotransport of a proton, help maintain a physiologic intracellular pH and resulting in acidification of the surrounding extracellular tumor environment that aids in tissue invasion. Specifically, this acidic environment promotes the degradation of the extracellular matrix by proteinases, increases angiogenesis through the release of vascular endothelial growth factor (VEGF) and inhibits immune responses to tumor antigens [Gillies and Gatenby, 2007a; Gillies and Gatenby, 2007b; Gatenby and Gillies, 2008]. The studies in this chapter show that this efflux of lactate can be directly measured *in vitro* with bioreactor systems. *In vivo*, it may not be possible to measure the extra- and intracellular hyperpolarized $^{13}$C metabolites directly, but measurements of their apparent diffusion coefficients (ADCs) provide information about their relative distribution within the tissue and between the extra- and intracellular environments. Ultimately, this chapter emphasizes the biologic importance of understanding the extra- and intracellular distribution of hyperpolarized $^{13}$C lactate and motivates the development of a technique in which this could be done clinically, as is done in Chapter 7.

## 6.2 Introduction

The use of hyperpolarized $^{13}$C pyruvate has shown clinical potential in identifying and characterizing tumors by measuring its real-time conversion to hyperpolarized $^{13}$C lactate [Nelson *et al.*, 2013]. These measurements observe the effects of one of the hallmarks of cancer cells: increased glycolysis [Warburg, 1956]. Studies in pre-clinical animal models of prostate cancer have shown increased hyperpolarized $^{13}$C lactate production with increasing cancer grade [Albers *et al.*, 2008]. Recently, the question whether hyperpolarized $^{13}$C pyruvate can be used to differentiate between benign and metastatic tumors has drawn attention [Keshari *et al.*, 2013]. Another hallmark of metastatic cancer cells is that they acidify their extracellular environment [Kroemer and Pouyssegur, 2008], a process promoting tumor growth and metastases. This acidification is a consequence of increased tumor lactate production, the upregulation of the monocarboxylate transporters 4 (MCT4) [Gallagher *et al.*, 2007; Gerlinger *et al.*, 2012], which co-transport lactate and protons out of the cell, and poor perfusion. Thus, measuring not only the overall production of hyperpolarized $^{13}$C lactate, but also its localization may improve the ability to non-invasively identify aggressive tumors with high metastatic potential using hyperpolarized $^{13}$C MR.

Recently, a study from our lab observed a reduced hyperpolarized $^{13}$C lactate signal in metastatic cancer cells. This *in vitro* study using a MR-compatible bioreactor, or cell perfusion system, shows that metastatic renal cell carcinoma (RCC) UOK262 cells transported hyperpolarized $^{13}$C lactate out of the cytoplasm during the course of the hyperpolarized $^{13}$C MR experiment [Keshari *et al.*, 2013]. By addressing relative expression levels of MCT1 and MCT4 between the indolent and metastatic cells, this study demonstrated how the localization of hyperpolarized $^{13}$C lactate between the extra- and intracellular environment could provide valuable information concerning tumor metastatic potential.

Diffusion weighted MR has been extensively used to assess the localization of various metabolites, both *in vitro* to study their extra- and intracellular distributions and *in vivo* to characterize tumor tissue microstructure based on water's apparent diffusion coefficient (ADC) [Le Bihan *et al.*, 1986]. Recently, there have been several publications that have used diffusion weighted MR to measure the diffusion coefficients of hyperpolarized $^{13}$C metabolites, in solution [Koelsch *et al.*, 2013b], in cell suspensions [Schilling *et al.*, 2013] and *in vivo*

[Kettunen *et al.*, 2013]. These studies showed how changes in the ADCs could indicate the extra- and intracellular localization of the hyperpolarized $^{13}$C metabolites. Yet, each of these studies used relatively small diffusion weighting gradients, or $b$-values, and thus measured only single diffusion coefficients from mono-exponential signal responses. Proton diffusion studies have shown that using a large range of $b$-values, with values upwards of 3000 s mm$^{-2}$, results in a multi-exponential signal response that is indicative of the various diffusion environments, shown both in cells [Tanner and Stejskal, 1968; Van Zijl *et al.*, 1991] and *in vivo* [Inglis *et al.*, 2001].

In the studies presented here, large diffusion gradients were used to investigate the extra- and intracellular distribution of hyperpolarized [1-$^{13}$C]pyruvate and its metabolites in RCC cells perfused in a MR compatible 3D cell culture bioreactor. Using $b$-values up to 15000 s mm$^{-2}$, a multi-exponential signal response was measured for the various hyperpolarized $^{13}$C metabolites and by fitting the fast and slow asymptotes of these curves, their extra- and intracellular diffusion coefficients were determined. Next, the dynamics of these extra- and intracellular hyperpolarized $^{13}$C metabolite pools were assessed in real-time, including the impact of inhibiting MCT4 catalyzed efflux of hyperpolarized $^{13}$C lactate. These studies demonstrate the importance of membrane transport, in addition to enzymatic activity, in understanding the metabolic flux of hyperpolarized $^{13}$C metabolites. Specifically for hyperpolarized $^{13}$C lactate, an overexpression of MCT4, as is found in the RCC cell line UOK262, contributes to a large extracellular fraction. While very high $b$-values, as used in this *ex vivo* study, are not feasibly achievable on clinical MRI systems to measure extra- and intracellular distribution of hyperpolarized $^{13}$C lactate, its ADCs can be measured on a clinical MRI scanner with relatively high $b$-values, as demonstrated in Chapter 7. These ADCs provide important information concerning the microenvironment of hyperpolarized $^{13}$C lactate, and ongoing studies are focused on determining the relationship between hyperpolarized $^{13}$C lactate ADC values and the presence, aggressiveness and metastatic potential of a variety of cancers.

## 6.3 Methods

### 6.3.1 RCC Cell Line Experiments in a NMR Compatible Bioreactor

Two different renal cell carcinoma (RCC) cell lines were used. UMRC6 cells are representative of localized human clear cell RCC [Grossman *et al.*, 1985], and were a gift from Dr. Bart Grossman (MD Anderson Cancer Center, Houston, TX; obtained January, 2010; authenticated using STR profiling, October 2012). UOK262 cells are derived from a metastasis of the highly aggressive hereditary leiomyomatosis RCC (HLRCC), which is characterized by mutation of the TCA cycle enzyme fumarate hydratase [Yang *et al.*, 2010]. UOK262 cells were a gift from Dr. W. Marston Linehan (National Cancer Institute, Bethesda, MD; obtained May, 2010; authenticated using STR profiling, October 2012). All cells were grown in Dulbeco's Modified Eagle's Medium (DMEM) with 4.5 g $L^{-1}$ glucose. The cells were passaged serially and were used for assays and magnetic resonance experiments between passages 2 to 10 and at 60–80% confluency. mRNA expression levels were assayed according to previously described protocols [Keshari *et al.*, 2013].

For bioreactor experiments, cells were electrostatically encapsulated into 3.5% w/v alginate microspheres, as previously described [Keshari *et al.*, 2010; Chandrasekaran *et al.*, 2006], and then loaded into a NMR spectrometer compatible bioreactor [Keshari *et al.*, 2010; Keshari *et al.*, 2013]. Approximately 800 μL of microspheres were perfused in the bioreactor with DMEM H-21 media at a flow rate of 2 mL $min^{-1}$. The media was kept at 37°C with water-jacketed perfusion lines and was maintained 95% air/5% $CO_2$ via gas exchanger.

All MR studies were performed on a 14.1 T Varian INOVA spectrometer (600 MHz $^{1}$H/150 MHz $^{13}$C) microimaging system (Agilent Technologies), equipped with a 10 mm broadband probe and 100 G cm$^{-1}$ gradients. Probe temperature was controlled at 37°C. $^{31}$P spectra were acquired before and after each hyperpolarized study to assess cell viability and measure the number of cells within the bioreactor, as previously described [Keshari *et al.*, 2013]; TR = 3 s, 512 or 1024 averages, 90° flip-angle.

### 6.3.2 Diffusion Weighted Studies of $^{1}$H Water

A $^{1}$H pulsed gradient single spin echo sequence with hard 90° and 180° pulses was used to measure the extra- and intracellular diffusion coefficients of water: TR = 2.5 s, TE = 26 ms, gradient pulse duration $\delta = 9$ ms, gradient pulse separation $\Delta = 16$ ms and without averaging. The diffusion weighting or $b$-value was arrayed by changing the gradient amplitudes $G$ from 0–46 G cm$^{-1}$, resulting in $b$-values 0–15944 s mm$^{-2}$. Diffusion gradients were applied in the transverse direction, i.e., $G_x$ or $G_y$. The flow was stopped for the duration of these scans to eliminate the effects of flow.

The diffusion coefficients of extra- and intracellular water determined by fitting the first 7 points (i.e., fast decaying asymptote) or last 7 points (i.e., slowly decaying asymptote) of the multi-exponential signal response to the equation [Stejskal and Tanner, 1965; Van Zijl *et al.*, 1991]

$$\ln(S/S_0) = -b\,D \tag{6.1}$$

where $S_0$ is the signal without diffusion weighting, $D$ is the diffusion coefficient (s mm$^{-2}$) and $b$ represents the diffusion weighting factor, or $b$-values, defined as

$$b = n\,\gamma^2\,G^2\delta^2(\Delta - \delta/3) \tag{6.2}$$

in which $\gamma$ is the gyromagnetic ratio and $n$ is 1 for single spin echo experiments and 2 for double spin echo experiments, here $^1$H and $^{13}$C experiments, respectively.

A $^1$H diffusion weighted spin echo imaging sequence was used to visually show the suppression of the extracellular water signal with increasing $b$-values. Again, only the gradient amplitude was changed to increase the diffusion weighting, while the gradient timing parameters were kept constant: $\delta = 6$ ms, $\Delta = 14$ ms. TR = 2 s, TE = 27.7 ms, FOV = 40 mm $\times$ 8 mm (RO $\times$ PE), 256 $\times$ 64 matrix, 0.5 mm slices and 10 or 100 averages. Experiments were in quadruplicates.

### 6.3.3 Hyperpolarization of $^{13}$C Metabolites

A HyperSense (Oxford Instruments) was used for dynamic nuclear polarization (DNP), operating at 3.35 T, 1.3 K and 94.100 GHz microwave irradiation for a minimum of 45 min. Sample preparation and polarization methods are similar to those previously published [Ardenkjær-Larsen *et al.*, 2003; von Morze *et al.*, 2013; Mayer *et al.*, 2012]. The [1-$^{13}$C] pyruvate preparation contained 14.1 M neat pyruvic acid, 16.5 mM of the trityl radical OX063 (GE Healthcare) and 1.5 mM Dotarem (Guerbet). The $^{13}$C urea preparation contained 390 mg of $^{13}$C urea dissolved in 895 mg of glycerol (Aldrich), and OX63 was added to a final concentration of 15 mM. For all cell studies, these two compounds were co-polarized and dissolved with 5 mL of a 50 mM phosphate-buffer, yielding a final concentration of 21.15 mM $^{13}$C pyruvate and 24 mM $^{13}$C urea. Studies with cell-free alginate microspheres were done with $^{13}$C lactate, in addition to $^{13}$C pyruvate and $^{13}$C urea. The [1-$^{13}$C] lactate preparation contained equal parts glycerol and a 50% by weight solution of sodium [1-$^{13}$C] lactate, 15mM of the trityl radical and 1 mM Dotarem; upon dissolution, lactate was at a final concentration of 15 mM. After dissolution, 1 mL of the hyperpolarized solutions were injected into the bioreactor in 30 s.

### 6.3.4 Diffusion Weighted Pulse Sequence for Hyperpolarized $^{13}$C

A pulsed gradient double spin echo sequence was used for all hyperpolarized $^{13}$C diffusion experiments, as seen in Figure 6.1a [Koelsch *et al.*, 2013b]. A 15° or 30° excitation pulse was used in combination with a pair of 180° hyperbolic secant adiabatic refocusing pulses (6 ms, 10 kHz). Diffusion gradient pulses were positioned symmetrically around both 180° pulses; $\delta = 10$ ms, $\Delta = 30$ ms. Only gradient amplitudes were varied to change the diffusion weighting or $b$-value and were applied in the transverse direction, i.e., $G_x$ or $G_y$. A crusher pulse (4 G cm$^{-1}$, 0.4 ms) was played after acquisition to dephase any remaining transverse magnetization. As is typical for hyperpolarized experiments, no signal averaging was used.

### 6.3.5 Extra- and Intracellular Diffusion Coefficients of Hyperpolarized $^{13}$C Metabolites

To measure the diffusion coefficients of extra- and intracellular hyperpolarized $^{13}$C metabolites, a gradient array was used where the highest $b$-values were acquired before smaller $b$-values (Figure 6.1b), thereby exploiting the strong hyperpolarized signal at the beginning of the experiment. To remove signal loss not due to diffusion weighting, normalization scans were interspersed throughout the gradient array, where the equation to used to determine the diffusion coefficients becomes

$$\ln(S') = -b\,D \tag{6.3}$$

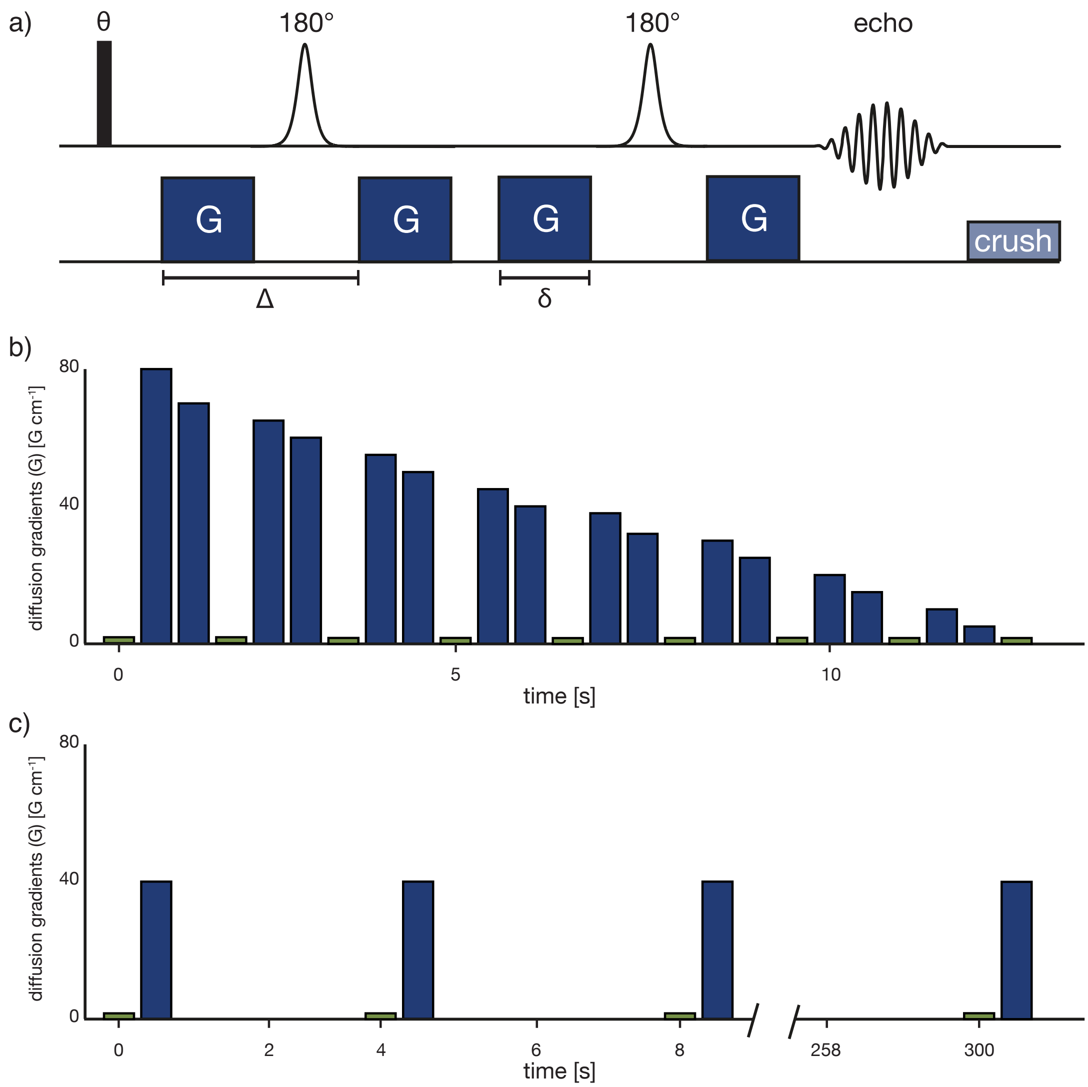


Figure 6.1: (**a**) The pulsed gradient double spin echo sequenced used for diffusion weighting of hyperpolarized $^{13}$C metabolites. Diffusion gradients (G) are placed symmetrically around the adiabatic 180° refocusing pulses, with a duration $\delta$ and a separation $\Delta$. A crusher gradient after the readout ensures no transverse magnetization carries-over to subsequent scans. The excitation flip angle $\theta$ was either 15° or 30°. (**b**) The diffusion gradient array used to measure the extra- and intracellular diffusion coefficients of hyperpolarized $^{13}$C metabolites. Every third scan (*green*) was used to normalize adjacent diffusion weighted scans (*blue*), thereby removing the effects of $T_1$ relaxation and metabolism on the signal change from that due to the diffusion weighting. (**c**) The gradient array used to measure the total (*green*) and the intracellular (*blue*) hyperpolarized $^{13}$C metabolite signals over time.

where $S'$ is the normalized diffusion weighted signal, is defined by

$$S' = \frac{S\ \cos^{-1}(\theta)}{S_{0+}} \tag{6.4}$$

or

$$S' = \frac{S}{S_{0-}\ \cos^{-1}(\theta)} \tag{6.5}$$

depending on whether the closest normalizing scan is either immediately before ($S_{0+}$) or after ($S_{0-}$) $S$. Normalizing scans $S_{0+}$ and $S_{0-}$ had G = 1 G cm$^{-1}$ and $b$-value = 2.42 s mm$^{-2}$. The cosine factor corrects for the difference in magnetization between $S$ and $S_{0+}$ or $S_{0-}$ due to multiple excitations from a single, non-renewable pool of magnetization. This normalization removes non-diffusion weighted signal changes. $b$ is defined by equation 6.2. For these experiments, $\theta = 30°$, G = 1–80 G cm$^{-1}$, $b$-value = 2–15,000 s mm$^{-2}$, TR = 0.5 s, TE = 79.8 ms.

As for the water signal, the extra- and intracellular diffusion coefficients were determined from fitting the fast and slowly decaying asymptotes. Specifically, the after normalizing the signal at each $b$-value (i.e., $S'$), the first 7 or the last 5 points were fit with equation 6.3. Experiments were in quadruplicates.

### 6.3.6 Assessment of Real-Time Membrane Transport of Hyperpolarized $^{13}$C Lactate

Using diffusion weighting, the total and the intracellular hyperpolarized $^{13}$C metabolite pools were monitored over time. This was accomplished using low and a high $b$-value scans in succession, after which a 3 s delay was inserted before the next pair of acquisitions were acquired (Figure 6.1c). The diffusion gradients of the low $b$-value scan, 2.4 s mm$^{-2}$, merely act as crusher gradients around each of the adiabatic refocusing pulses and don't impart any significant diffusion weighting. The diffusion weighting necessary to observe intracellular signal was chosen by identifying a $b$-value where, under flowing conditions in the bioreactor, the hyperpolarized $^{13}$C pyruvate hydrate signal that had been injected into cell-free alginate microspheres was completely suppressed, namely a $b$-value = 3863 s mm$^{-2}$. The suppression of hyperpolarized $^{13}$C pyruvate hydrate was chosen because its signal intensity is in the same order of magnitude as the $^{13}$C lactate signal. The signal intensity of $^{13}$C pyruvate is over an order of magnitude greater and thus choosing a diffusion weighting necessary to suppress it lead to very poor SNR for the other hyperpolarized $^{13}$C metabolites.

The same pulsed gradient double spin echo sequence was used for these acquisitions: $\theta$ = 15°, TR = 0.5 s, TE = 79.8 ms, low $b$-value = 2.4 s mm$^{-2}$ at G = 1 G cm$^{-1}$, high $b$-value = 3863 s mm$^{-2}$ at G = 40 G cm$^{-1}$, $\delta$ = 10 ms, $\Delta$ = 30 ms, delay between paired low and high $b$-value scans = 3 s, total acquisition time = 300 s.

The conversion of hyperpolarized $^{13}$C pyruvate to lactate was assessed by taking the ratio

$$\frac{L_{total}}{P_{total}} \approx \frac{\sum_{n}^{N} L(n)}{\sum_{n}^{N} P(n)} \tag{6.6}$$

where $L_{total}$ and $P_{total}$ are the sum of the signals at all time points (i.e., the area under the curve) acquired here for the total signal at the low $b$-value. This ratio has previously been shown correlate with $k_{PL}$ measurements made with models of the rate of enzymatic conversion of lactate dehydrogenase (LDH) [Hill *et al.*, 2013].

Using a similar approach, we assessed the of the hyperpolarized $^{13}$C metabolites during the time course of the experiment by taking the ratio of the signals acquired at the high and low $b$-values, namely the intracellular to the total hyperpolarized $^{13}$C metabolite signal

$$\frac{X_{intra}}{X_{total}} \tag{6.7}$$

where $X$ represents the signal for pyruvate ($P$), lactate ($L$) or urea ($U$). The $X_{intra}$ signal has been corrected for signal loss of the intracellular $^{13}$C metabolite due to application of the diffusion gradients. The correction uses the intracellular diffusion coefficient measured ($D_x$, see Table 6.1) and the difference in the $b$-values used for these measurements

$$X_{intra} = X'_{intra} \frac{\exp(-D_x \cdot 2.4)}{\exp(-D_x \cdot 3863)} \tag{6.8}$$

The amount of extracellular signal was determined by taking the difference in the total and the intracelluar signals, according to

$$\frac{X_{intra}}{X_{extra}} = \frac{X_{intra}}{X_{total} - X_{intra}} \tag{6.9}$$

These ratios were normalized to the number of cells used for each experiment, as measured by $^{31}$P spectroscopy and previously described [Keshari *et al.*, 2013].

Cells were treated with 1 mM 4,4'-Di-isothiocyanostilbene-2,2'-disulphonic acid (DIDS), an inhibitor of monocarboxylate transporters (MCTs), within the bioreactor for 40 min before injection of the hyperpolarized solution to modulate the extra- and intracellular hyperpolarized $^{13}$C lactate pools. To clearly see the relative change in the ratios before and after treatment, each ratio for the pre-treatment data was normalized to 1.

A paired two-sample t-test was used for all statistical comparisons with $\alpha = 0.05$. All values represented as mean $\pm$ standard deviation.

## 6.4 Results

### 6.4.1 Extra- and Intracellular Diffusion Coefficients of $^1$H Water

Measuring water signal of the cells encapsulated in the alginate microspheres over a range of $b$-values reveals a multi-exponential signal decay (Figure 6.2a). The self-diffusion of water is represented by the fast asymptote, while the water within the cells is represented by the slow asymptote, as has been previously described for bioreactor cell experiments [Van Zijl *et al.*, 1991]. The open markers in Figure 6.2a is the water signal from cell-free alginate microspheres and shows no signal at higher $b$-values, given the absence of an intracellular environment. At mid-range $b$-values (i.e., 4000–6000 s mm$^{-2}$) the presence of the water within the alginate microspheres can be seen by the slight trailing-off of the curve, as has been previously described [Pilatus *et al.*, 1997]. The extra- and intracellular diffusion coefficients of water are listed in Table 6.1 and seen graphically in Figure 6.4.

The diffusion weighted imaging experiment, shown in Figure 6.2b, visually confirms the suppression of extracellular water signal with increasing $b$-values. Shown is a NMR tube with three regions: only water, cell-free microspheres and cells encapsulated within the alginate microspheres. With images, only intracellular water signal remains at merely 3200 s mm$^{-2}$, which is lower than that indicated by the graph in Figure 6.2a acquired spectroscopically. This most likely arises because of the lower sensitivity of the imaging sequence.

### 6.4.2 Diffusion Weighted Pulse Sequence for Hyperpolarized $^{13}$C

The pulsed gradient double spin echo sequence was chosen for the diffusion weighting of hyperpolarized $^{13}$C metabolites, given that it has several advantages. Spectral phase is improved with the use of a pair of adiabatic refocusing pulses, where the second refocusing

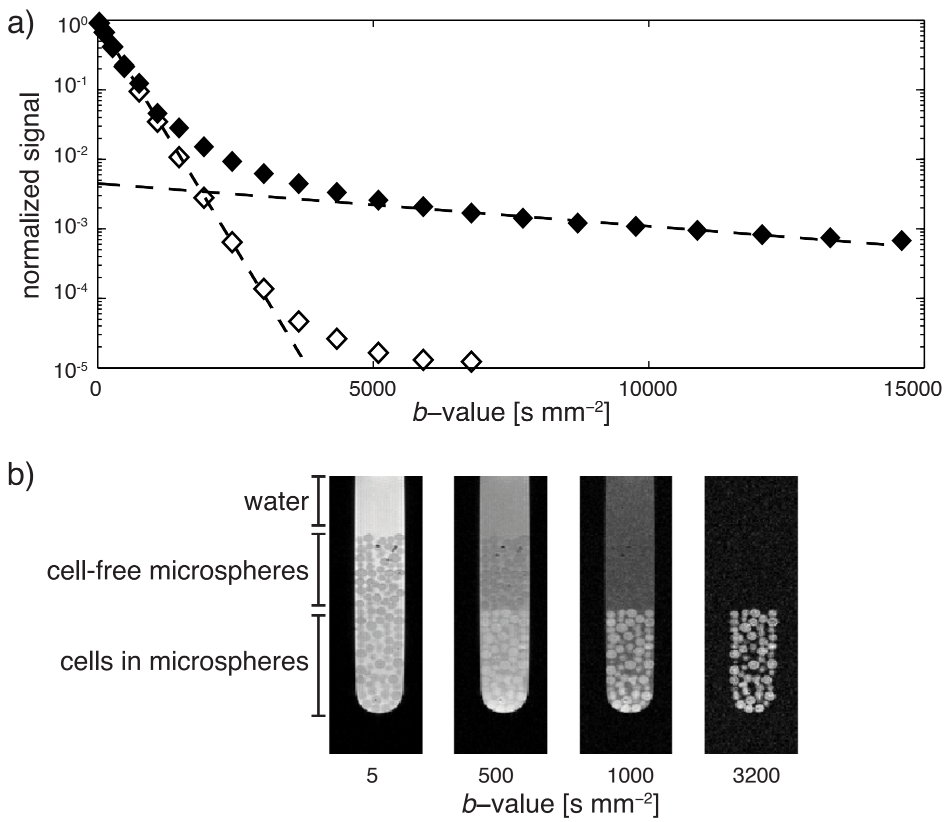


Figure 6.2: (**a**) The water signal response with increasing diffusion weighting in the bioreactor. For cells encapsulated in the alginate microspheres (⧫), the water signal response reveals the presence of multiple environments with different water diffusion coefficients. The fast and slow asymptotes (*dotted lines*) were used to determine extra- and intracellular diffusion coefficients, respectively. The water signal response in cell-free microspheres (◊) reflects water diffusion in solution and in the microspheres. (**b**) A diffusion weighted imaging experiment confirms the presence of the different diffusion environments. At low *b*-values, water signal is present in all three environments. As the *b*-values increase, signal from compartments with faster diffusion decreases while signal from highly restricted environments (i.e., intracellular). At *b*-values above 3200 s mm$^{-2}$, only signal from within the cells can be seen. The intensity of these images are scaled independently to more easily identify the various features.

pulse re-winds any non-linear phase imparted by the first [Conolly *et al.*, 1989]. The pair of refocusing pulses also places the hyperpolarized magnetization back onto the $+z$ axis before the next excitation, which over the time course of the experiment prevents mixing of hyperpolarized magnetization that is oriented along the $+z$ and $-z$ axes that would lead to rapid signal loss [Cunningham *et al.*, 2007].

The use of two pair of diffusion gradients for this diffusion sequence also has several advantages. First, the relatively small gyromagnetic ratio of $^{13}$C nuclei complicates diffusion weighting, as seen by equation 6.2. Hence, the use of two pair of diffusion gradients doubles the $b$-value, allowing for $b$-values upward to 15000 s mm$^{-2}$. Additionally, the two pair of diffusion gradients will minimize the diffusion time ($\Delta - \delta/3$) necessary to achieve a desired $b$-value, since each gradient pair will separately de- and re-phase the magnetization. This minimizes the effects of a restricted environment (i.e., cells) in the diffusion coefficient measurements [Tanner and Stejskal, 1968], where longer diffusion times would lead to decreases in the measured diffusion coefficient [Pilatus *et al.*, 1997]. In the studies discussed here, the diffusion times are kept constant, 13 ms for $^{1}$H studies and 26.7 ms for $^{13}$C studies, while the gradient amplitudes are changed to increase the diffusion weighting. While these are relatively short diffusion times, the diffusion coefficients presented here are still apparent diffusion coefficients since there will inevitably still be some restricted diffusion effects.

### 6.4.3 Extra- and Intracellular Diffusion Coefficients of Hyperpolarized $^{13}$C Metabolites

As for the water signal, the diffusion coefficients of the hyperpolarized $^{13}$C metabolites can be determined in the extra- and intracellular environments within the bioreactor. Yet, in the case of hyperpolarized $^{13}$C metabolite signal, several sources of signal change are present that will complicate the quantification of diffusion coefficients. These include the decay of the hyperpolarized signal due to $T_1$, repeatedly taking the signal from a single, non-renewable pool of magnetization and metabolism. To remove the effects of these non-diffusion weighted signal changes, we acquired multiple normalization scans throughout the experiment. The result gives a multi-exponential signal response where, like for the water measurements, the fast and slow asymptotes correspond to the extra- and intracellular diffusion coefficients, as seen in Figure 6.3a. All extra- and intracellular diffusion coefficients are listed in Table 6.1 and seen graphically in Figure 6.4.

To confirm the ability to measure purely intracellular hyperpolarized $^{13}$C metabolite signal, the signal decay of these same compounds was measured in cell-free alginate microspheres, represented by the open markers in Figure 6.3a. At lower $b$-values, the fast signal decay rate (i.e., diffusion coefficient) for hyperpolarized $^{13}$C pyruvate, pyruvate hydrate and urea corresponds with that from encapsulate cell studies. The fast decay rate or extracellular diffusion coefficient of hyperpolarized $^{13}$C lactate, however, is different between cell-free microspheres and the experiments with encapsulated cells. This difference may arise from the difference in the localization of the dominant hyperpolarized $^{13}$C lactate signal. In the cell-free microsphere experiment, $^{13}$C lactate was polarized and injected into the bioreactor, thereby being predominantly in the media and resulting in a higher extracellular diffusion coefficient (Table 6.1). In the cell encapsulates, the hyperpolarized $^{13}$C lactate was produced within the cells and transported into the extracellular environment during the experiment, thus most likely being localized within the alginate microspheres and so having a lower extracellular diffusion coefficient (Table 6.1) than in free solution.

### 6.4.4 Assessing Extra- and Intracellular Pools of Hyperpolarized $^{13}$C Lactate

To monitor the extra- and intracellular hyperpolarized $^{13}$C metabolite pools over the time course of the experiments, we intermittently measured the total and the intracellular signals with low and high degrees of diffusion weighting, respectively. Figure 6.5 shows the distribution of hyperpolarized $^{13}$C pyruvate and lactate between the extra- and intracellular compartments. Considering that hyperpolarized $^{13}$C pyruvate is injected at excess into the bioreactor, its intracellular fraction is small fraction of the total signal. The hyperpolarized $^{13}$C lactate that is produced in the cells is actively transported out of the cells via MCT4 and in UOK262 cells, the intracellular signal can be seen by the red lines in Figure 6.5c and 6.5d.

Treatment of the UOK262 cells with 1 mM of the MCT inhibitor DIDS shows clear modulation of the extra- and intracellular hyperpolarized $^{13}$C lactate pools; see Figure 6.6. DIDS has been shown to inhibit MCT4 more readily than MCT1 [Dimmer *et al.*, 2000], the dominant transporters for lactate efflux and pyruvate uptake [Pinheiro *et al.*, 2012], respectively.

With DIDS treatment, Figure 6.6 shows that the conversion of hyperpolarized $^{13}$C pyruvate to lactate decreases, as shown be the decrease in the ratios $L_{total}/P_{total}$ and $L_{intra}/P_{intra}$. This may result from a combination of two effects: one, that DIDS also partially inhibits MCT1 and therefore less hyperpolarized $^{13}$C pyruvate may be available for conversion, and two, that with the inhibition of hyperpolarized $^{13}$C lactate efflux, the intracellular lactate concentration increases and inhibits the forward conversion of pyruvate to lactate via LDH-A.

The overall extra- and intracellular distribution of the these hyperpolarized $^{13}$C metabolites was assessed by taking the ratios $X_{intra}/X_{total}$ and $X_{intra}/X_{extra}$, where $X$ represents the metabolites pyruvate ($P$), lactate ($L$) and urea ($U$). The distribution of hyperpolarized $^{13}$C pyruvate and urea do not significantly change with treatment of DIDS. However, there is a significant increase in the intracellular fraction of hyperpolarized $^{13}$C lactate with DIDS treatment, as expected since DIDS has a higher affinity for MCT4 than MCT1.

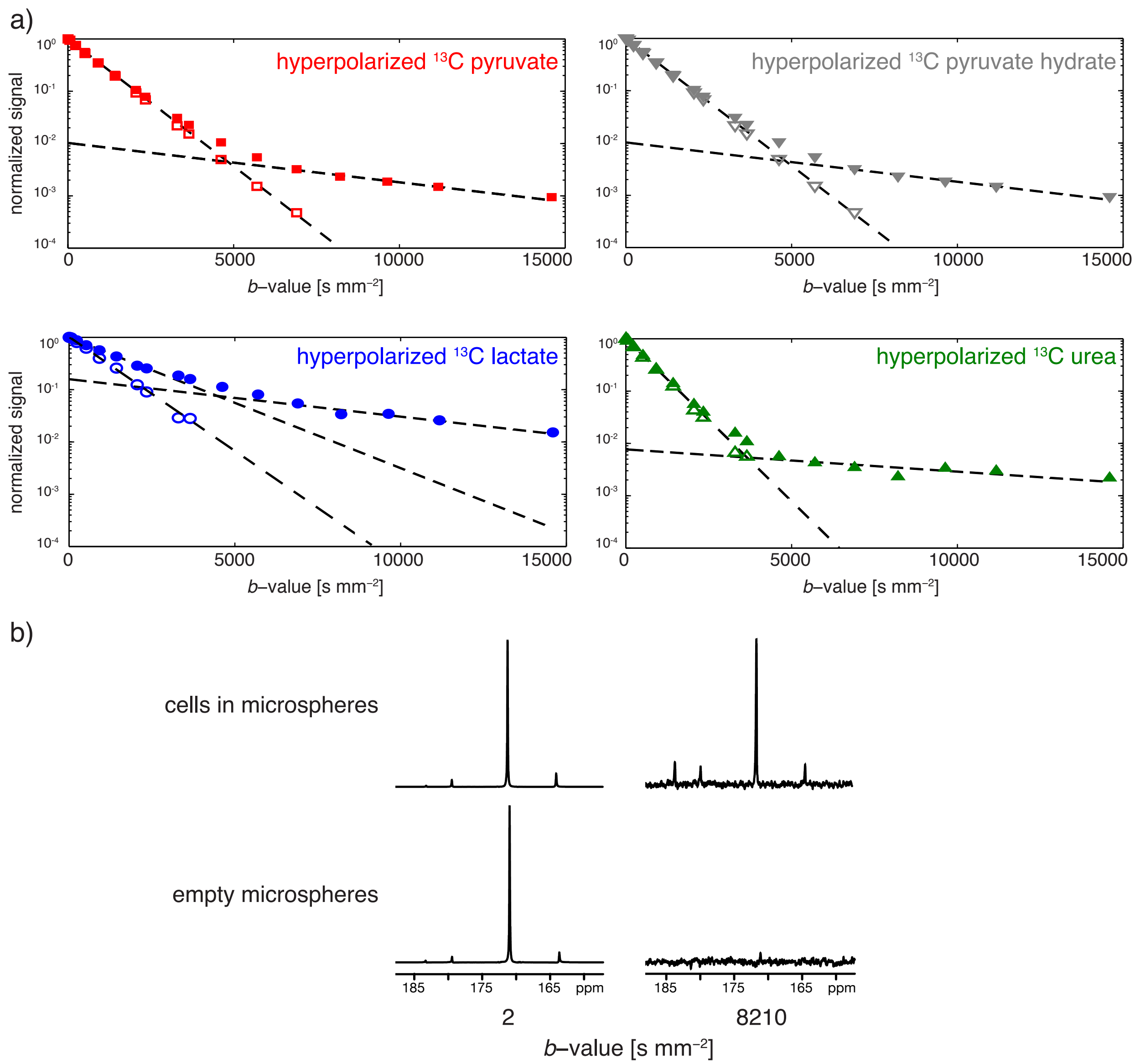


Figure 6.3: (**a**) Hyperpolarized $^{13}$C metabolite signal response with increasing diffusion weighting in the bioreactor. The graphs of hyperpolarized $^{13}$C pyruvate, pyruvate hydrate, lactate and urea each reveal multiple diffusion environments in experiments with cells encapsulated in alginate microspheres (*filled symbols*). As for water (Figure 6.2), the fast and slow asymptotes were used to determine the diffusion coefficients in the extra- and intracellular environments, respectively. Diffusion weighting of these hyperpolarized $^{13}$C metabolites in cell-free microspheres are also shown (*empty symbols*). (**b**) Spectra of the hyperpolarized $^{13}$C metabolites with increasing diffusion weighting shows the suppression of extracellular signals at higher *b*-values. Spectra at a single *b*-value, both with and without cells, are scaled to the same SNR.

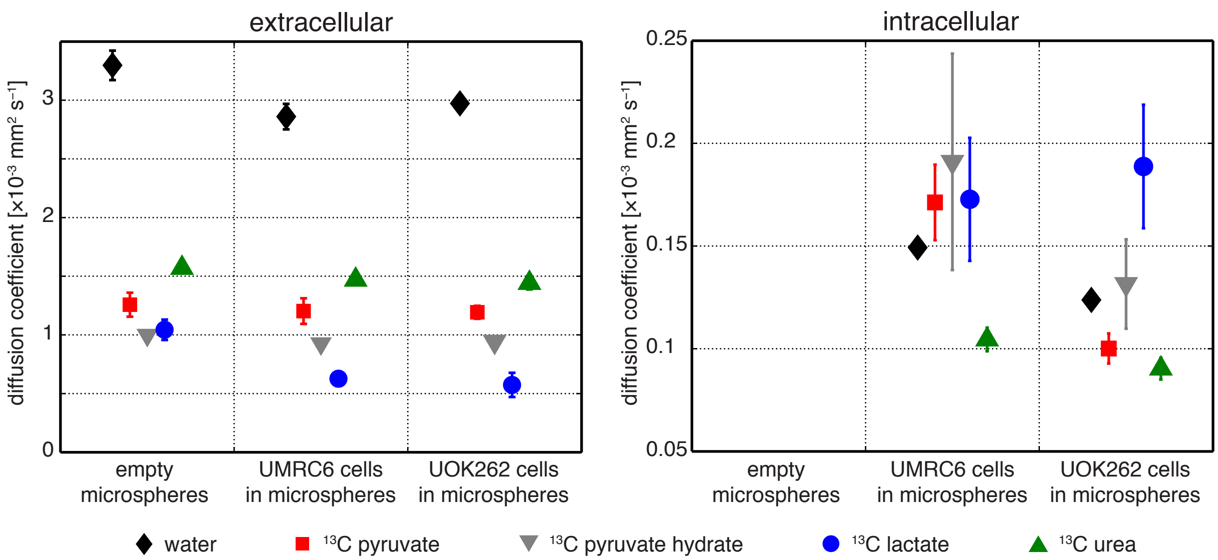


Figure 6.4: The extra- and intracellular diffusion coefficients of water and several hyperpolarized $^{13}$C metabolites for cell-free alginate microspheres and UMRC6 cell and UOK262 cells encapsulated within the microspheres. The diffusion coefficients correspond to the fast and slow asymptotes, shown in Figures 6.2 and 6.3. Values listed in Table 6.1.

Table 6.1: Diffusion coefficients ($D$) of $^{1}$H water and hyperpolarized $^{13}$C metabolites at 37°C, as measured in the bioreactor

Extracellular $D$ [$\times 10^{-3}$ mm$^2$ s$^{-2}$]

| | $^{1}$H Water | $^{13}$C Pyruvate | $^{13}$C Pyruvate Hydrate | $^{13}$C Lactate | $^{13}$C Urea |
|---|---|---|---|---|---|
| Microspheres | 3.27±0.13 | 1.26±0.10 | 0.99±0.02 | 1.04±0.08 | 1.57±0.03 |
| UMRC6 | 2.86±0.11 | 1.20±0.11 | 0.93±0.02 | 0.63±0.06 | 1.47±0.04 |
| UOK262 | 2.97±0.03 | 1.19±0.06 | 0.94±0.03 | 0.57±0.10 | 1.44±0.06 |

Intracellular $D$ [$\times 10^{-3}$ mm$^2$ s$^{-2}$]

| | $^{1}$H Water | $^{13}$C Pyruvate | $^{13}$C Pyruvate Hydrate | $^{13}$C Lactate | $^{13}$C Urea |
|---|---|---|---|---|---|
| Microspheres | – | – | – | – | – |
| UMRC6 | 0.15±0.006 | 0.17±0.02 | 0.19±0.05 | 0.17±0.03 | 0.10±0.006 |
| UOK262 | 0.12±0.002 | 0.10±0.007 | 0.13±0.02 | 0.19±0.03 | 0.09±0.006 |

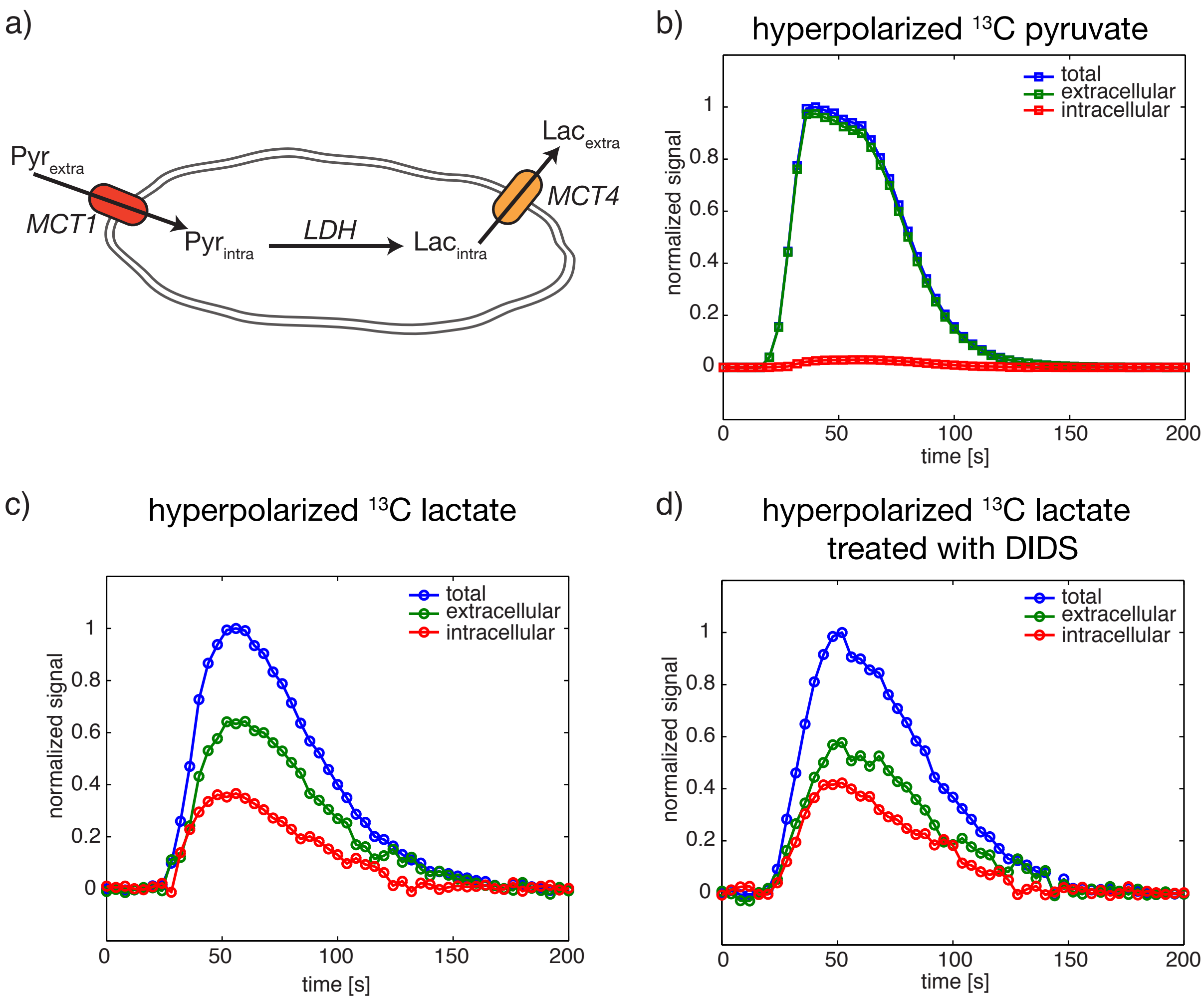


Figure 6.5: (**a**) A schematic of a cell showing the transport of hyperpolarized $^{13}$C pyruvate into the cell via the monocarboxylate transporter 1 (MCT1), its conversion to hyperpolarized $^{13}$C lactate by the enzyme lactate dehydrogenase (LDH) and the transport of $^{13}$C lactate out of the cell via MCT4. The dynamic signals of hyperpolarized $^{13}$C pyruvate (**b**) and lactate (**c**) in UOK262 cells perfused in the bioreactor, showing the total, extra- and intracellular metabolite pools. (**d**) UOK262 cells treated with the high-affinity MCT4 inhibitor DIDS show increased hyperpolarized $^{13}$C lactate within the intracellular compartment. All plots are normalized to the respective maximum total signal.

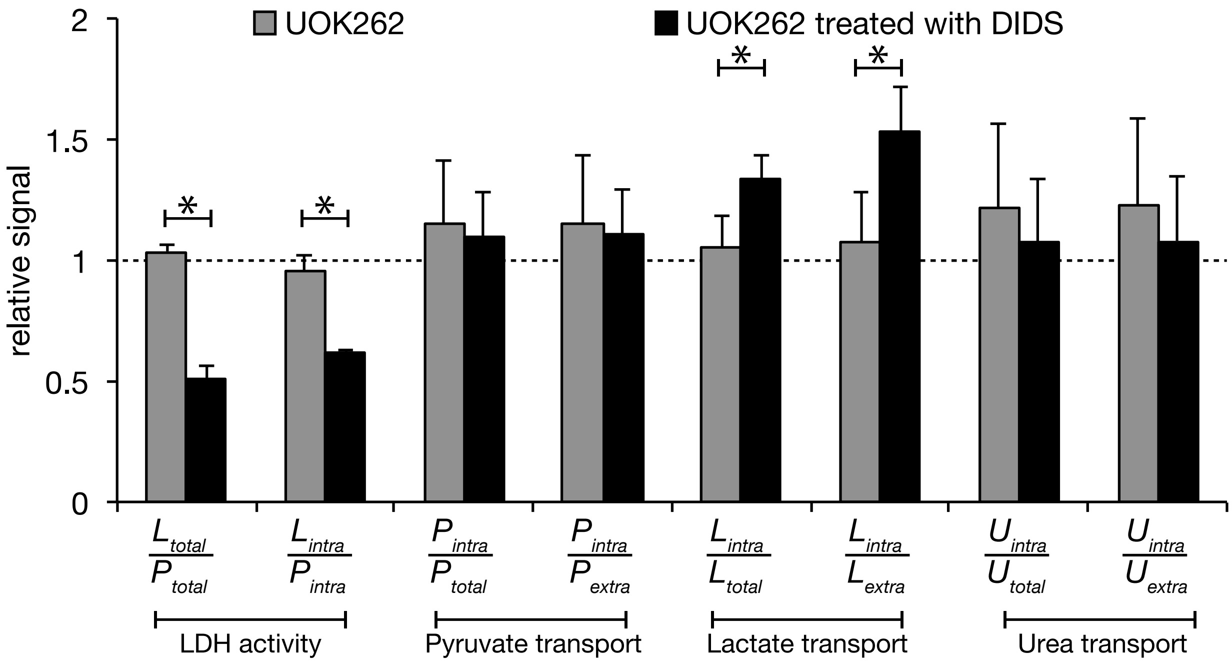


Figure 6.6: The relative changes in metabolism and membrane transport of hyperpolarized $^{13}C$ metabolites in UOK262 cells, without and with treatment with DIDS, a high-affinity inhibitor of MCT4. The ratios for LDH activity show a significant decrease with DIDS treatment. The membrane transport ratios for hyperpolarized $^{13}C$ pyruvate and urea do not change with DIDS treatment. The increase in the lactate transport ratios shows that DIDS inhibition of MCT4 leads to a higher intracellular fraction of hyperpolarized $^{13}C$ lactate. Intracellular hyperpolarized $^{13}C$ metabolite signals were acquired with a high *b*-value while extracellular signals were determined by taking the difference between the total and intracellular signals. Significant differences with p-value $< 0.05$ are represented by $*$.

## 6.5 Discussion

### 6.5.1 Extra- and Intracellular Diffusion Coefficients

As previous studies of cells in bioreactors have shown, acquiring metabolite signal with increasing diffusion weighting results in a multi-exponential signal response, where the fast and slowly decaying asymptotes represent the extra- and intracellular diffusion coefficients of the molecule under study [Van Zijl *et al.*, 1991]. The water diffusion coefficients measured in the extracellular environments (Table 6.1) align nicely with those values previously published [Mills, 1973; Holz *et al.*, 2000]. Likewise, the intracellular water diffusion coefficients measured (Table 6.1) also align with those measured previously [Van Zijl *et al.*, 1991; Pfeuffer *et al.*, 1998]. The main purpose of these water diffusion coefficient measurements was to verify a previously established methodology in order to extend it to measuring the extra- and intracellular diffusion coefficients of hyperpolarized $^{13}$C metabolites.

Measuring diffusion coefficients of hyperpolarized $^{13}$C molecules is challenging because of the multiple sources of signal change, including $T_1$ decay, repeated excitations from a single, non-renewable pool of magnetization and metabolism. Previous studies have quantified these signal change not due to diffusion weighting and corrected the diffusion weighted acquisitions accordingly [Koelsch *et al.*, 2013b; Schilling *et al.*, 2013]. To simplify the quantification, here we acquire multiple interspersed normalization scans temporally close to the diffusion weighted scans and thereby eliminate the effects of these non-diffusion weighted signal changes. This methodology was verified in solution studies of hyperpolarized $^{13}$C urea where diffusion coefficients measured via this technique aligned with those calculated after corrections to the data for $T_1$ signal loss [Koelsch *et al.*, 2013b]; data not shown. The idea here is similar to previous studies where every diffusion weighted acquisition ($S_{echo}$) by the non-diffusion weighted signal acquired immediately after excitation ($S_{FID}$) [Kettunen *et al.*, 2013]. In encapsulated cell experiments, this produces multi-exponential curves for these hyperpolarized $^{13}$C metabolites similar to those for water, where the fast and the slowly decaying asymptotes correspond to the extra- and intracellular diffusion coefficients.

The extracellular diffusion coefficients for these hyperpolarized $^{13}$C metabolites, as measured in the cell-free microspheres, correspond well with those measured previously in solution [Koelsch *et al.*, 2013b], accounting for difference in temperature and the more restricted environment of the alginate. Previous cell suspension studies [Schilling *et al.*, 2013] of the diffusion coefficients of hyperpolarized $^{13}$C pyruvate, pyruvate hydrate and lactate with *b*-values up to $\sim 1500$ s mm$^{-2}$ measured diffusion coefficients of these molecules approximately equal to those measured here in the extracellular space (Table 6.1). The low *b*-values used in that study were not sufficient to measure purely intracellular diffusion coefficients. All other currently published studies reporting hyperpolarized $^{13}$C metabolite diffusion coefficients were acquired *in vivo* [Kettunen *et al.*, 2013; Sogaard *et al.*, 2014; Patrick *et al.*, 2014] and also used lower *b*-values than those used in this study. Those reported diffusion coefficients are therefore between the extra- and intracellular values measured in this study (Table 6.1). The diffusion coefficients measured *in vivo* thus represent the combined effects of both the extracellular tissue and the intracellular environments. Similarly, water measurements in tissue are higher than those listed above for purely intracellular water [Clark and Le Bihan, 2000].

The intracellular diffusion coefficients for the hyperpolarized $^{13}$C metabolites measured here correspond to values measured previously *in vivo* of lactate using a $\{^{1}\mathrm{H}\text{–}^{13}\mathrm{C}\}$ editing technique and*b*-values up to 50000 s mm$^{-2}$ [Pfeuffer *et al.*, 2005]. The purely extra- and intracellular metabolite diffusion coefficients measured in this *ex vivo* study can be used to better interpret the more complex *in vivo* hyperpolarized $^{13}$C lactate ADC findings, which are a consequence of both proportion of extra- and intracellular lactate as well as changes in the tumor microenvironment.

### 6.5.2 Assessment of Membrane Transport of Hyperpolarized $^{13}$C Metabolites

The same study that inspired the extra- and intracellular diffusion coefficient measurements [Van Zijl *et al.*, 1991] also showed the ability to measure membrane transport by observing solely the intracellular signal at a specified $b$-value. With hyperpolarized $^{13}$C metabolites, the signal is sufficiently high that measurements can be made in real-time, without the need to average signals for prolonged periods of time, as is necessary for the thermal NMR measurements. When the total and the intracellular signals are observed in time, with low and high $b$-values, respectively, the dynamic change in the extra- and intracellular metabolite pools can be measured.

The dynamic changes in extra- and intracellular hyperpolarized $^{13}$C lactate observed in this study was consistent with substantial efflux of lactate out of UOK262 cells within the time-frame of the hyperpolarized MR study. This finding is consistent with a prior published MR compatible cell culture bioreactor study of UOK262 cells, in which flow-rate modulations in the bioreactor demonstrated that hyperpolarized $^{13}$C lactate was being transported out of the cell and washed-away during the time frame of the hyperpolarized MR study [Keshari *et al.*, 2013]. Treatment of the UOK262 cells with DIDS in this study, a MCT inhibitor with a more sensitive inhibitory effect for MCT4 than for MCT1 [Dimmer *et al.*, 2000], reduced the relative extracellular hyperpolarized lactate pool size, further verifying that the diffusion weighted experiments were providing a measurement of extra- and intracellular metabolite pools.

MCTs are a class of transports that shuttle various monocarboxylates across the cell membrane, coupled with the transport of a proton. MCT1 exhibit higher affinity for pyruvate influx while MCT4s facilitate lactate efflux [Pinheiro *et al.*, 2012]. It is well established that many malignant cancers exhibit an upregulation of MCT4 [Ullah *et al.*, 2006], as can be seen in RCC tumors [Gerlinger *et al.*, 2012] and breast cancer [Gallagher *et al.*, 2007]. In cancer cells, the role of MCT4 in shunting lactate and protons form the intracellular environment helps maintain an intracellular physiologic pH while acidifying the extracellular space and thereby promotes invasion into the surrounding tissue [Webb *et al.*, 2011; Stock and Schwab, 2009]. The studies presented here show that hyperpolarized $^{13}$C lactate is superbly suited to evaluate the efflux of lactate from cancer cells. More studies are needed to evaluate the differences in hyperpolarized $^{13}$C lactate efflux in normal, indolent and metastatic cancer cells. In this clinical setting, this would allow for a more refined characterization of cancer cells, where evaluations would incorporate both the extent of hyperpolarized $^{13}$C lactate production and its distribution.

## 6.6 Conclusion

In this study, we use large diffusion weightings to measure the extra- and intracellular distribution of hyperpolarized $^{13}$C metabolites. Use of a pulsed gradient double spin echo sequence with strong diffusion gradient amplitudes allows us to achieve $b$-values up to 15000 s mm$^{-2}$. Measurements of hyperpolarized $^{13}$C metabolite signal for an array of $b$-values allow us to measure their extra- and intracellular diffusion coefficients. Furthermore, in experiments employing alternating low and high $b$-values allowed the dynamic measurement of the total and intracellular hyperpolarized $^{13}$C metabolite signals in time, allowing for a real-time assessment of their relative extra- and intracellular pool sizes. Given the known upregulation of MCT4 in metastatic cancer cells, diffusion weighted hyperpolarized $^{13}C$ MR may provide an assessment of not only cancer presence but also its aggressiveness and metastatic potential.

## 6.7 Supplemental Content

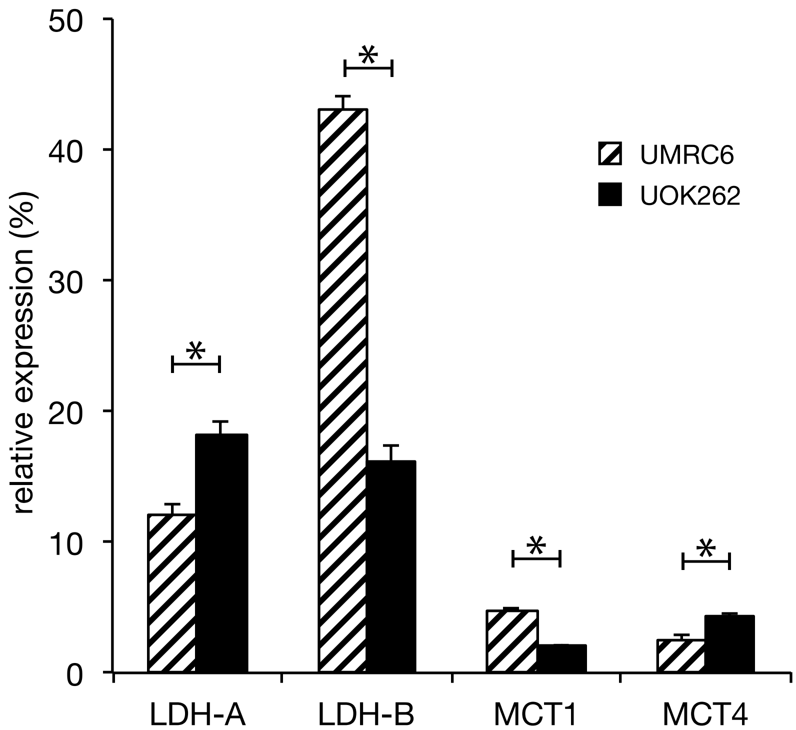


Figure 6.7: The mRNA expression levels of lactate dehydrogenase (LDH) and monocarboxylate transporters (MCT) for two RCC cells lines. UMRC6 cells are from a localized human clear cell RCC while UOK262 cells are derived from a metastasis of the highly aggressive hereditary leiomyomatosis RCC (HLRCC). LDH-A preferentially converts pyruvate to lactate, while LDH-B does the opposite. MCT1 has a higher affinity for pyruvate uptake while MCT4 for lactate transport out of the cells. Significant differences with p-value $< 0.05$ are represented by $*$.

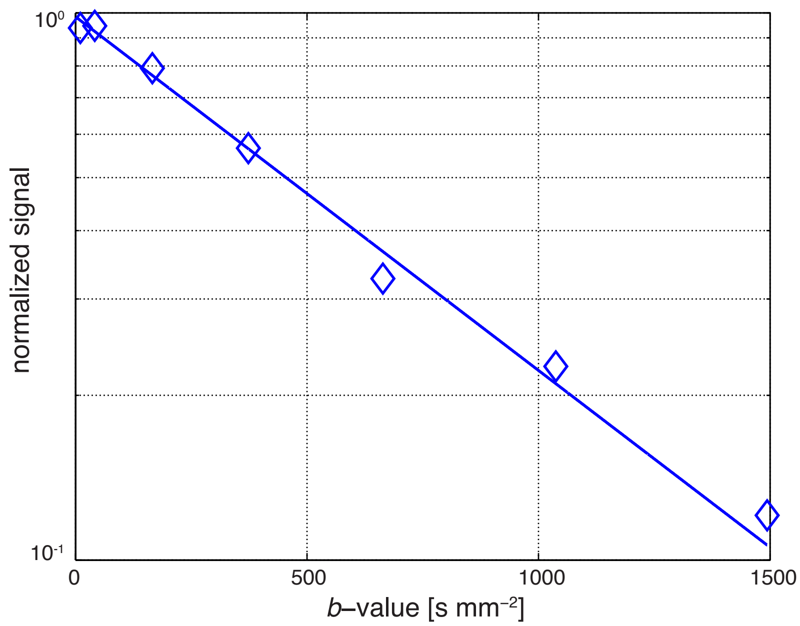


Figure 6.8: The diffusion coefficient for $^{13}$C urea measured using the technique presented in Figure 6.1, where higher *b*-value scans were immediately preceded by normalization scans. This process eliminates non-diffusion weighted signal loss, here due to $T_1$ decay, and allows for easier quantification of diffusion coefficients. The diffusion coefficient for hyperpolarized $^{13}$C urea measured here is $1.49 \times 10^{-3}$ mm$^2$ s$^{-1}$, which aligns well with previously measured values seen in Table 5.1.

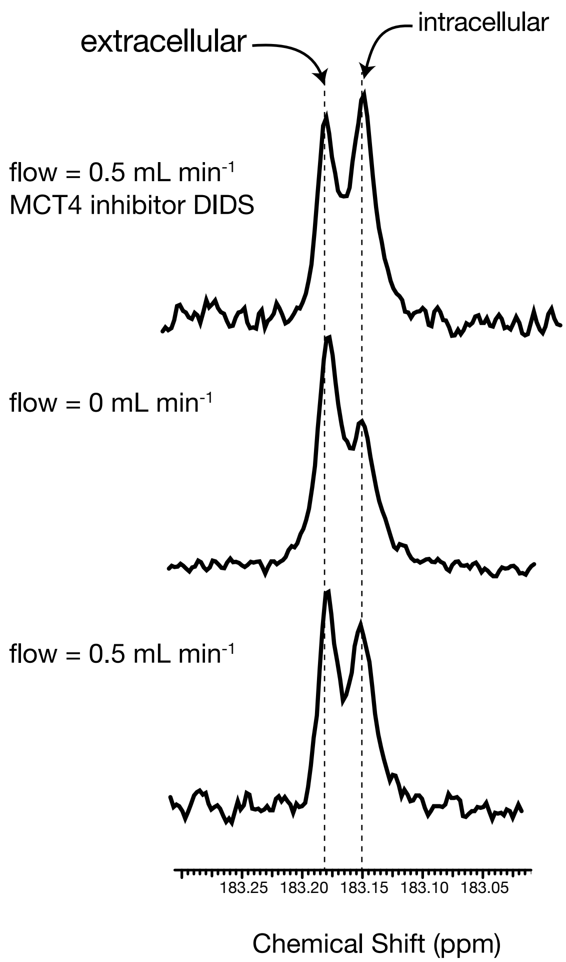


Figure 6.9: The chemical shift separation of extra- and intracellular hyperpolarized $^{13}$C lactate that can be observed using a 5 mm bioreactor with shim of $\sim$ 13 Hz and 230 Hz at the 50% and 0.11% linewidths in proton, respectively. The chemical shift separation comes from susceptibility differences of the extra- and intracellular environments. These peaks are from the maximum lactate signal during a hyperpolarized $^{13}$C experiments. At a flow rate of 0.5 mL min$^{-1}$, the ratio of $L_{intra}/L_{extra} = 2.23$. Stopping the flow in the bioreactor allows for the extracellular hyperpolarized $^{13}$C lactate to accumulate, as seen by the increase in the left peak, and resulting in a 15% decrease in the ratio $L_{intra}/L_{extra}$ ($= 1.90$). Treating the UOK262 cells with 1 mM of the MCT4 inhibitor DIDS prevents export of lactate from the cytoplasm and thus we observe increase in the intracellular hyperpolarized $^{13}$C lactate peak, increasing the ratio $L_{intra}/L_{extra}$ ($=$ 3.55) by 60%.

# Chapter 7

# Rapid in vivo ADC Mapping of Hyperpolarized $^{13}C$ Metabolites

## 7.1 Chapter Overview

This chapter focuses on the development of a methodology that enables diffusion weighted (DW) imaging and apparent diffusion coefficient (ADC) mapping of hyperpolarized $^{13}C$ metabolites on a clinical MRI scanner. The techniques presented here will facilitate the clinical translation of the DW techniques for hyperpolarized $^{13}C$ metabolites. Given this, tumor identification and characterization will not only be done with metabolite flux measurements, but also with ADC maps that elucidate the distribution of these metabolites within the tissue microenvironment.

Hyperpolarized $^{13}C$ MR allows for the study of real-time metabolism *in vivo*, including significant hyperpolarized $^{13}C$ lactate production in many tumors. Other studies have shown that aggressive and highly metastatic tumors rapidly transport lactate out of cells. Thus, the ability to not only measure the production of hyperpolarized $^{13}C$ lactate but also understand its compartmentalization using diffusion weighted MR will provide unique information for improved tumor characterization.

Here, we used a bipolar pulsed-gradient double spin echo EPI sequence to rapidly generate diffusion-weighted images of hyperpolarized $^{13}$C metabolites. Our methodology included a simultaneously acquired $B_1$ map to improve apparent diffusion coefficient (ADC) accuracy and a diffusion compensated variable flip angle scheme to improve ADC precision. The DW sequence and methodology is validated in hyperpolarized $^{13}$C phantoms. Next, we generated ADC maps of several hyperpolarized $^{13}$C metabolites in a rat brain tumor model, a prostate cancer mouse model and a normal rat using both pre-clinical and clinical trial-ready hardware.

ADC maps of hyperpolarized $^{13}$C metabolites provide information about the localization of these molecules in the tissue microenvironment. The methodology presented here allows for further studies to investigate ADC changes due to disease state that may provide unique information about cancer aggressiveness and metastatic potential.

## 7.2 Introduction

Fast diffusion weighted (DW) echo-planar imaging (EPI) techniques have allowed apparent diffusion coefficient (ADC) maps of water to become an invaluable tool for the identification and characterization of various cancers [Padhani *et al.*, 2009], including brain tumors [Sugahara *et al.*, 1999] and prostate cancer [Nagarajan *et al.*, 2012]. Structural changes in the tissue microstructure caused by the tumor masses alter the local mobility of water molecules and thereby generate contrast in DW images and ADC maps.

The growing field of hyperpolarized $^{13}$C magnetic resonance (MR) [Ardenkjær-Larsen *et al.*, 2003; Keshari and Wilson, 2014] has also proven to be useful in identifying and characterizing tumors by measuring the real-time metabolism of hyperpolarized $^{13}$C pyruvate to lactate, in both brain tumors [Park *et al.*, 2010] and prostate cancer [Albers *et al.*, 2008]. These abnormally high levels of hyperpolarized $^{13}$C lactate arise from a shift towards increased aerobic glycolytic metabolism, a process known as the Warburg effect [Warburg, 1956]. Currently, *in vivo* MR studies spatially localize these hyperpolarized $^{13}$C metabolites to identify tumor masses (9). However, these acquisitions give no discrimination of the distribution of the hyperpolarized $^{13}$C metabolites within the tissue microstructure based on their local mobility.

Having the ability to identify both the overall production of hyperpolarized $^{13}$C lactate and its extra- and intracellular distribution could be useful for improved tumor identification and characterization. Research has shown that aggressive and metastatic tumors acidify their extracellular environment [Gatenby and Gillies, 2004], a process that facilitates the tumors invasion into surrounding tissue. Acidification in part happens via the export of protons through monocarboxylate transporters (MCTs), which is coupled to the export of lactate [Halestrap and Price, 1999]. Correspondingly, a recent study comparing two renal cell carcinoma cell lines showed that while increased hyperpolarized $^{13}$C lactate production was seen in all cancer cell lines, the highly aggressive metastatic cells also rapidly pumped more hyperpolarized $^{13}$C lactate out of the cell [Keshari *et al.*, 2013].

Recently, several studies have combined DW techniques with hyperpolarized $^{13}$C to rapidly measure the translational motion of these molecules. Solution state studies verified the accuracy of the measurements with diffusion coefficient measurements of molecules with varying molecular weights [Koelsch *et al.*, 2013b]. Cell studies rapidly measuring the ADCs of hyperpolarized $^{13}$C pyruvate and lactate have shown that intracellular metabolites have lower diffusion coefficients than the extracellular metabolites [Schilling *et al.*, 2013; Koelsch *et al.*, 2013a]. Animal studies using DW spectroscopic techniques of hyperpolarized

$^{13}$C metabolites showed improved tumor contrast [Larson *et al.*, 2012], assessed their vascular and tissue distribution [Kettunen *et al.*, 2013] and measured their ADCs in muscle tissue [Sogaard *et al.*, 2014]. One recent hyperpolarized $^{13}$C imaging study used bipolar gradients to suppress flowing vascular spins, which improved metabolic measurements [Gordon *et al.*, 2013]. Clinical translation of DW MR of hyperpolarized $^{13}$C metabolites will allow for the identification and characterization of tumors based on both the conversion of hyperpolarized $^{13}$C pyruvate to lactate and on their localization to various microenvironments.

In this work, we present a technique for rapidly generating ADC maps of hyperpolarized $^{13}$C metabolites using a bipolar pulsed-gradient double spin echo, single-shot EPI sequence. The bipolar diffusion gradient pairs produce diffusion weighting ($b$-values) upwards of 1,000 s mm$^{-2}$, compensating for the relatively small gyromagnetic ration of $^{13}$C ($\gamma$ = 10 MHz T$^{-1}$) and the limited maximum gradient amplitudes on clinical MR scanners (e.g., 40 mT m$^{-1}$). Our technique includes a simultaneously generated $B_1$ map to improve the accuracy of the ADC measurements, while a diffusion compensated variable flip angle (VFA) scheme improves their precision. The technique presented here lays the foundation for generating robust ADC maps of hyperpolarized $^{13}$C metabolites on clinical MR scanners and its use in improved characterization of cancers in patients.

## 7.3 Methods

### 7.3.1 Scanner Hardware

All scans were done on a General Electric Signa MR 3T scanner equipped with a broadband RF amplifier and gradients with 40 mT m$^{-1}$ peak amplitudes and 150 mT m$^{-1}$ ms$^{-1}$ peak slew rates. A custom designed $^{13}$C/$^{1}$H dual-tuned transmit/receive birdcage coil was used for mouse studies, rat brain studies and phantom studies; diameter = 5 cm, length = 8 cm, operating in quadrature for both $^{13}$C and $^{1}$H [Chen *et al.*, 2007]. Whole body rat studies were performed using clinical hardware; a custom designed $^{13}$C transmit clamshell coil with two linear 4-channel carbon-tuned receive panels, where each rectangular coil element is 5 $\times$ 10 cm [Ohliger *et al.*, 2013].

### 7.3.2 Hyperpolarization

Sample preparation and polarization methods are similar to those previously published [Ardenkjær-Larsen *et al.*, 2003; von Morze *et al.*, 2013; Mayer *et al.*, 2012]. The [1-$^{13}$C] pyruvate preparation contained neat pyruvic acid, 16.5 mM of the trityl radical OX063 (GE Healthcare) and 1.5 mM Dotarem (Guerbet). The [1-$^{13}$C] lactate preparation contained equal parts glycerol and a 50% by weight solution of sodium [1-$^{13}$C] lactate, 15mM of the trityl radical and 1 mM Dotarem. HMCP (bis-1,1-(hydroxymethyl)-[1-$^{13}$C]cyclopropane-$d_8$), also referred to as HP001, was mixed with water in a ratio of 2.78:1 by weight, with 19 mM OX063 and 1.2 mM Dotarem. A HyperSense (Oxford Instruments) was used for dynamic nuclear polarization (DNP), operating at 3.35 T, 1.3 K and 94.100 GHz microwave irradiation for a minimum of 45 min. After polarization, pyruvate was dissolved with an 80–100 mM NaOH saline solution with 10mM TRIS to achieve 80 mM (for mice) or 100 mM (for rats) solutions of hyperpolarized [1-$^{13}$C] pyruvate at pH $\approx$ 7.4. Lactate and HMCP were dissolved with a phosphate-buffered saline solution at 40 mM and 100 mM concentrations, respectively, at pH $\approx$ 7.4.

### 7.3.3 $^1$H Diffusion Imaging

DW proton images were acquired with a pulsed gradient single spin echo sequence. These images were acquired in the axial plane and diffusion weighting was applied in the through-slice direction at $b$-values = [0, 600] s mm$^{-2}$, echo time (TE) = 68 ms, repetition time (TR) = 4 s, 1.25×1.25 mm resolution, 64×64 matrix, 4 mm slice thickness, 16 averages.

### 7.3.4 Hyperpolarized $^{13}$C Diffusion Imaging

Prior to hyperpolarized $^{13}$C studies, a rough flip angle calibrations were performed by measuring the transmitter power required to produce a signal null ($\theta = 180°$) with a thermally polarized 8 M $^{13}$C urea phantom, doped with 2 mM Dotarem, placed at the edge of the coil. Hyperpolarized $^{13}$C DW imaging experiments were performed using a bipolar pulsed-gradient double spin echo sequence with a single-shot flyback EPI readout; total readout time = 32.6 ms, echo spacing = 2.9 ms, duty cycle = 41.4% (Figure 7.1). A spectral-spatial excitation pulse was used in conjunction with a pair of adiabatic refocusing pulses. Similar to prior $^{13}$C spin echo acquisitions [Koelsch *et al.*, 2013b; Kettunen *et al.*, 2013; Josan *et al.*, 2011; Cunningham *et al.*, 2007], the sequence consisted of a slice-selective excitation pulse followed with a pair of adiabatic refocusing pulses.

A symmetric-frequency response,"true null" spectral-spatial pulse [Meyer *et al.*, 1990] was designed similar to those used in prior hyperpolarized $^{13}$C studies to excite a single metabolite [Lau *et al.*, 2010; Schulte *et al.*, 2013]. This excitation had a 60 Hz FWHM spectral bandwidth, 13 mm minimum slice thickness, 400 Hz stop-band, and was designed to alternatively excite [1-$^{13}$C] lactate and [1-$^{13}$C ] pyruvate, which have a 390 Hz chemical shift separation at 3.0 T.

The dual-tuned $^{13}C/^{1}H$ dual-tuned transmit/receive birdcage coil used 10 ms sech/tanh (HS*n*, *n*=1) adiabatic 180° refocusing pulses [Cunningham *et al.*, 2007]; refocusing bandwidth = 2000 Hz and peak-power = 1 G. The $^{13}C$ transmit clamshell coil used low-power 15 ms stretched hyperbolic secant (HS*n*, *n*=3) adiabatic 180° refocusing pulses [Park *et al.*, 2006; Hu *et al.*, 2009]; refocusing bandwidth = 600 Hz and peak-power = 0.3 G. Both adiabatic pulses were nominally run at 20% above the adiabatic threshold. RF and gradient spoiling were used to ensure transverse magnetization would not carry-over to subsequent scans.

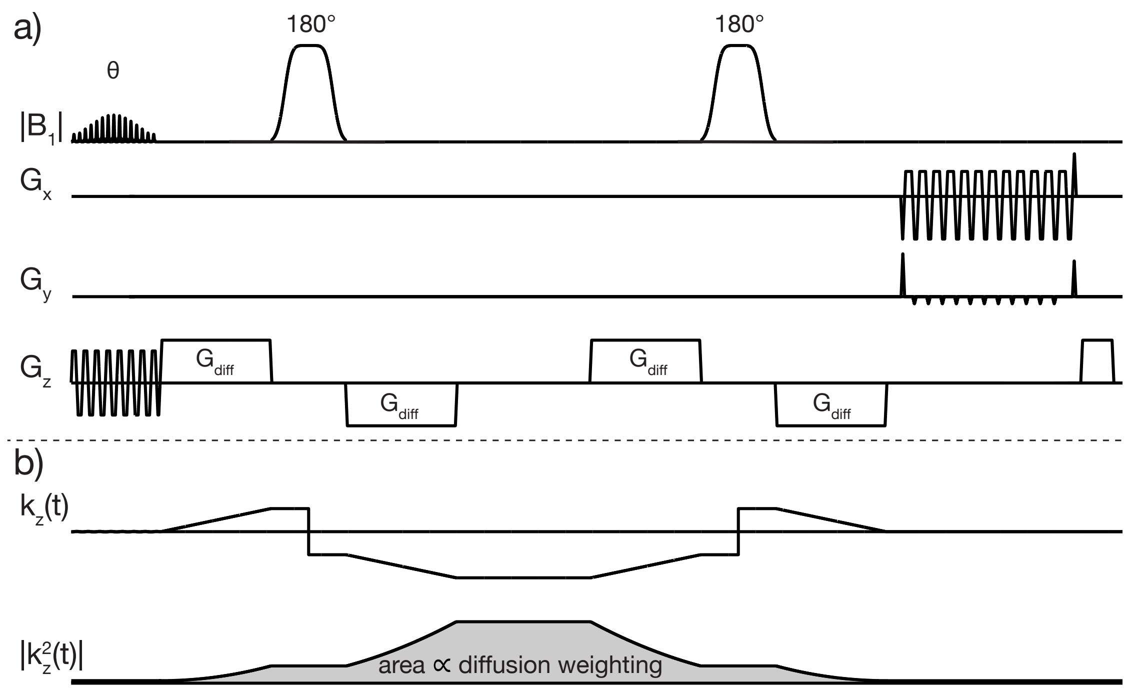


Figure 7.1: (**a**) The bipolar pulsed-gradient double spin echo sequence used for diffusion weighting imaging of hyperpolarized $^{13}C$ metabolites on a clinical 3T MR scanner. The flip angle (θ) of the spectral-spatial excitation pulse is changed according to the variable flip angle (VFA) scheme. A single-shot echo-planar imaging (EPI) readout is followed by a crusher gradient. For these experiments, the slice-select and diffusion gradients were applied on $G_z$, while the EPI readout gradients were applied on the orthogonal axes. (**b**) The bipolar pulsed-gradients can apply diffusion weightings (*b*-values) upwards of 1,000 s mm$^{-2}$ for $^{13}C$, as represented by the shaded area under $|k_z{}^2(t)|$.

Bipolar diffusion gradients pairs surrounding each of the refocusing pulses [Reese *et al.*, 2003] maximized the diffusion-sensitizing period and thereby considerably increased the diffusion weighting achievable with this sequence; $b$-values up to 1,000 s mm$^{-2}$ for $^{13}$C with the parameters used in these studies. All diffusion gradients were applied in the through slice direction. To vary the diffusion weighting between scans, only the gradient amplitudes were changed (0–40 mT m$^{-1}$), while diffusion gradient durations (22 ms each) and TE were kept constant to eliminate $T_2$-weighting differences between scans. The diffusion weighting between scans were changed as a function of the maximum $b$-value, i.e., $b$-values $= b_{max} \cdot$ [1, 0.3125, 0.01, 0.01]. Each hyperpolarized $^{13}$C molecule was scanned four times within a 1 s total acquisition time (Figure 7.2); TE=175 or 180 ms, TR=250 ms. For the experiments where both hyperpolarized $^{13}$C pyruvate and lactate were imaged, the latter was image first.

### 7.3.5 Variable Flip Angle Schemes

All acquisitions made use of a variable flip angle (VFA) scheme that was designed to consume the entire pool of the non-renewable hyperpolarized signal. Unless mentioned otherwise, the flip angles were changed between scans according a standard VFA scheme [Zhao *et al.*, 1996; Nagashima, 2008]

$$\theta = \arctan\left(\frac{1}{\sqrt{N-n}}\right) \tag{7.1}$$

where $N$ represents the total number of scans, while $n$ is each individual scan. For four scans, the flip angles were 30°, 35°, 45° and 90°. In the absence of diffusion gradients and flip angle inaccuracies, all four images have comparable signal-to-noise (SNR). The application of diffusion gradients results in scan-specific signal loss proportional to the $b$-value applied.

A diffusion compensated VFA scheme was designed to improve ADC measurement precision by increasing the SNR at higher $b$-value images and producing constant SNR across all

DW scans. Signal loss due to diffusion weighting for a given diffusion coefficient and $b$-value scheme was compensated for by increased flip angles. Here, the $D = 0.83 \times 10^{-3}$ mm$^2$ s$^{-1}$ and $b_{max} = 1005$ s mm$^{-2}$ give the flip angles 50°, 42°, 45° and 90°.

In all VFA schemes, the effect of longitudinal $T_1$ relaxation was neglected given that the total scan time (1 s) was much less than $T_1$ for the hyperpolarized $^{13}$C molecules.

### 7.3.6 Phantom Experiments

Upon dissolution from the HyperSense, 1 mL of the hyperpolarized compound was thoroughly mixed with 59 mL of room temperature, deionized water. The final temperature of this solution was 22°C $\pm$ 1, as measured with an infrared thermometer. The thoroughly mixed solution was added to a 60 mL syringe and placed into the coil within the scanner. The solution was allowed to settle for 90 s before scanning to minimize non-diffusive motion. Shorter settling intervals produced non-uniform signal loss with DW imaging, indicative of non-diffusion motion. Phantoms were scanned in the coronal plane at 3.3 $\times$ 3.3 mm resolution, 24 $\times$ 12 matrix and one 13 mm slice.

### 7.3.7 Animal Experiments

Animal studies were performed under a protocol approved by the UCSF Institutional Animal Care and Utilization Committee. Animals were anesthetized with an isoflurane/oxygen mixture and placed on a pad heated to 37°C. All anatomic images were acquired in axial and coronal planes with a $T_2$-weighed fast spin echo (FSE), using either the $^{13}$C/$^{1}$H dual-tuned transmit/receive birdcage coils or the MR scanners body coils. Transgenic prostate cancer mouse models (TRAMP) at different stages of tumor progression were used. Hyperpolarized $^{13}$C diffusion images for mice were acquired in the coronal plane at 3.3 $\times$ 3.3 mm resolution,

$24 \times 12$ matrix, one 50 mm slice with bmax = 969 or 1005 s mm$^{-2}$. Hyperpolarized $^{13}$C images of brain tumor bearing rats were acquired in the axial plane at $3.3 \times 3.3$ mm resolution, $12 \times 12$ matrix, one 13 mm slice with bmax = 1005 s mm$^{-2}$. These tumors were induced via intracranial injection of U87 glioblastoma cells ($3 \times 10^5$ cells in 10 μL) on in 5–6week old athymic rats [Chaumeil *et al.*, 2013] and were scanned approximately 30 days later. Whole body hyperpolarized $^{13}$C diffusion image of normal Sprague Dawley rats, using the custom $^{13}$C transmit clamshell coil and receive coil array, were scanned with $8.8 \times 8.8$ mm resolution, $24 \times 12$ matrix, one 20 mm slice with $b_{max}$ = 933 s mm$^{-2}$. The relatively large slices used in all experiments were implemented to achieve sufficient SNR for these DW experiments. For experiments using the diffusion compensated VFA scheme, flip angles were 50°, 42°, 45° and 90°. All animals were imaged 35 s after the start of a 12 s injection.

### 7.3.8 Data Analysis

Proton ADC maps were generated by fitting the signal on a per-voxel basis to the following equation describing the signal response as a function of the diffusion weighting applied ($b$-value):

$$\ln(S_i/S_0) = -b \cdot ADC \tag{7.2}$$

where $S_i$ is the diffusion sensitized signal for a certain $b$, while $S_0$ is the non-diffusion sensitized signal, and the slope represents the ADC

The $b$-values for hyperpolarized $^{13}$C scans were determined from numerical integration according to [Bernstein *et al.*, 2004]:

$$b = \gamma^2 \int_0^{TE} k^2(t)dt \tag{7.3}$$

where

$$k(t) = \frac{\gamma}{2\pi} \int_0^t G(t')dt' \tag{7.4}$$

Encoding and readout gradients each produced $b$-values $\ll 1$ s mm$^{-2}$ and thus were neglected for all ADC measurements. The shaded area in Figure 7.1b shows how diffusion weighting is proportional to $|k^2(t)|$.

Creating ADC maps of the hyperpolarized $^{13}$C molecules with our methodology was a multistep process, summarized with the schematic in Figure 7.2. After acquisition, a $B_1$ map of the sample was created to correct for any errors in the transmit-gain/deviations from the expected flip angle excitations. The final two images were acquired with minimal diffusion weighting, maximizing the sample SNR used to generate the $B_1$ map. Having acquired these images with 45° and 90° flip angles, we used a modified version of the double angle method [Insko and Bolinger, 1993] that accounts for the non-renewable hyperpolarized magnetization. Using the double angle identity

$$\sin(2\theta) = 2\ \sin(\theta)\ \cos(\theta) \tag{7.5}$$

and correcting for use of the non-renewable hyperpolarized magnetization by a factor of $\cos(\theta)$, we can compare the signal ($S$) of images of scans 3 and 4

$$\frac{S_3}{S_4} = \frac{2\ \sin(2\theta_3)\ \cos(\theta_3)}{\sin(\theta_3)} = \frac{2\ \sin(\theta_3)\ \cos(\theta_3)\ \cos(\theta_3)}{\sin(\theta_3)} = 2\ \cos^2(\theta_3) \tag{7.6}$$

where solving for $\theta_3$ on a per-voxel basis gives the true flip angle used in scan 3. Comparison with the expected flip angle for scan 3 (i.e., 45°), gives the error in the flip angles. Performing this calculation on all voxels with SNR $> 4$ results in the $B_1$ map. This map was subsequently used to correct flip angle for each scan and the voxel-wise signal for each scan:

$$S_{n,corr} = \frac{S_{n,acq}}{\sin(\theta_n) \cdot \prod_{k=1}^{n-1} \cos(\theta_k)} \tag{7.7}$$

The ADC map for each hyperpolarized $^{13}$C metabolite was created from the first three images, acquired at three different $b$-values. Note that the VFA schemes are designed for four images, the last two of which are used to create the $B_1$ map while only the first three images were used for generating the ADC maps. Thus, making the ADC maps does not use all the hyperpolarized magnetization. The ADC values were fit according to equation 7.2. For quantification, hyperpolarized $^{13}$C images, $B_1$ maps and ADC maps were kept at the acquired resolution. ADCs in the text are presented as mean ± standard deviation for the number voxels ($N_{vox}$) within a region of interest (ROI). The Mann-Whitney U test for independent observations, which does not require normally distributed data, was used for statistical comparisons of ADCs from different ROIs within the same animal ($\alpha = 0.05$).

Co-registration of $^1$H and $^{13}$C images was done by first interpolating the $^{13}$C images with nearest-neighbor interpolation to the resolution of the corresponding $^1$H image. Since the $^{13}$C images were acquired either on resonance or were shifted according to the frequency offset, the images were overlaid and the ROIs were manually drawn on the $^{13}$C images accordingly. For representation, all hyperpolarized $^{13}$C DW images were interpolated, while $B_1$ and ADC maps were left at the acquired resolution.

Diffusion coefficients of pyruvate and lactate were taken from previously published values [Koelsch *et al.*, 2013b], adjusted for temperature and viscosity using the Stokes-Einstein equation. The diffusion coefficient for HMCP was measured on an NMR spectrometer at 22°C using a previously published method [Koelsch *et al.*, 2013b].

$T_1$ relaxation was neglected from all calculations due to the short TR used. All data analysis was done in Matlab (MathWorks Inc).

### 7.3.9 Simulations

The effects of transmit-gain/excitation flip angle errors on ADC measurement accuracy were assessed with simulations. Diffusion data for a physiologically relevant range of diffusion coefficients (true ADC = 0.2  2.2 × 10-3 mm$^2$ s$^{-1}$) were simulated for the $b$-values scheme presented in Figure 7.2 ($b$-values = [969, 303, 9.7, 9.7] s mm$^{-2}$) with flip angle deviations from the expected flip angles ($\theta$ = [30°, 35°, 45°, 90°]) of ± 20%. ADCs were then fit from these data by fitting points 1–3 to equation 7.2. Each measured ADC was compared with the true ADC to quantify the resulting error in ADC measurements as a result of flip angle errors.

As discussed above, a diffusion compensated VFA scheme was designed to counteract signal loss due to diffusion weighting at different $b$-values. The resulting diffusion compensated VFA scheme produces images with relatively constant SNR across all scans and different $b$-values. Specifically, signal with the expected ADC used to design the specific diffusion compensated VFA will have constant SNR across all images. Signal from molecules with smaller and larger ADCs will experience a slight decrease and increase in SNR, respectively, across the images acquired with the $b$-value scheme used here. All molecules, however, will have improved SNR at the higher $b$-values with the diffusion compensated VFA than with the standard VFA. To assess how this SNR improvement at higher $b$-values improves ADC measurements, a Monte Carlo simulation was run to compare ADCs measured with the standard VFA scheme ($\theta$ = [30°, 35°, 45°, 90°]) and the diffusion compensated VFA scheme ($\theta$ = [50°, 42°, 45°, 90°]). Simulated data was generated for three physiologically relevant diffusion coefficients, true ADC = [0.3, 0.8, 1.3] $\times$ $10^{-3}$ mm$^2$ s$^{-1}$ with $b$-values = [1005, 314, 10, 10] s mm$^{-2}$. Note that while the diffusion compensated VFA was designed for molecules with D = 0.83 $\times$ $10^{-3}$ mm$^2$ s$^{-1}$, simulations were also run on molecules with both smaller and greater ADCs than this D, since this will be the case *in vivo*. Pseudorandom noise with normal distribution and scaled to a specified SNR for the last low $b$-value scan for the standard VFA scheme was added to all simulated data. The simulated diffusion compensated VFA data was flip angle corrected. All ADCs were calculated using equation 7.2. The effect of noise was simulated 5,000 times for each of the two VFA schemes. These data are presented as mean  standard deviation. Levene's test for equality of variances was used to statistically compare the simulated ADC distributions between the standard and the diffusion compensated VFA schemes at each true ADC value and at each specified SNR level ($\alpha = 0.05$). Levenes test does not require data to be normally distributed, which was seen for the distribution of the simulated ADCs at low SNR. A rejection of the null-hypothesis identifies a difference in the variance of the two simulated ADC datasets. All simulations were done in Matlab (MathWorks, Inc.).

## 7.4 Results

### 7.4.1 Improving ADC Mapping Accuracy and Precision

The bipolar pulsed-gradient double spin echo EPI sequence (Figure 7.1) with a VFA and $b$-value scheme (Figure 7.2a) was designed to efficiently generate ADC maps of hyperpolarized $^{13}$C metabolites on a clinical MRI scanner. The $b$-values were chosen to probe the distribution of the hyperpolarized $^{13}$C signal in different environments: the overall signal at a low $v$-value ($\approx$ 10 s mm$^{-2}$), the extravascular signal with the mid $b$-value ($\approx$ 300 s mm$^{-2}$) and the highly restricted signal with a high $b$-value ($\approx$ 1,000 s mm$^{-2}$). In addition to diffusion weighting, long sequence TEs could also contribute to reduced vascular signal where these $^{13}$C molecules have shorter $T_2$s [Kettunen *et al.*, 2013]. ADCs were calculated by using all three of these $b$-values.

MRI studies are prone to transmit-gain miscalibrations, resulting in either an over- or underestimation of the prescribed flip angle. Spatial variations in the transmit $B_1$ field, which can be quite large over human-sized volumes, may cause local excitation flip angle offsets. In the case of hyperpolarized experiments, where all scans draw signal from a non-renewable pool of longitudinal magnetization, $B_1$ errors propagate between scans and lead to quantification inaccuracies. The simulation presented in Figure 7.3a shows how flip angle errors will skew ADC calculations for hyperpolarized $^{13}$C molecules. The magnitude of the error depends on the true ADC of the molecules. For example, the black dotted line represents the true ADC of pyruvate in solution, $0.96 \times 10^{-3}$ mm$^2$ s$^{-1}$ [Koelsch *et al.*, 2013b]. In this case, a -17% flip angle offset results in 13% ADC overestimation. The use of the VFA makes ADC measurement errors resulting from flip angle offsets dependent on the ordering of the $b$-value, where strategic placement of the different $b$-value scans will minimize these errors. Figure 7.3a shows the errors resulting from the $b$-value scheme presented in Figure 7.2a.

Transmit-gain errors can be corrected with a simultaneous acquisition of a $B_1$ map, allowing for flip angle corrections and improved measurement accuracy. The sequence and $B_1$ mapping methodology was validated with hyperpolarized $^{13}$C pyruvate and lactate phantoms. Using two low $b$-value images maximizes the sample SNR used to create the $B_1$ map. For hyperpolarized $^{13}$C pyruvate, the simultaneously acquired $B_1$ map (Figure 7.2b) shows a -17 $\pm$ 1% flip angle offset in the center of the image. The $B_1$ map pattern aligns with our expectations for a birdcage coil, with decreased flip angles at either end of the coil and axially

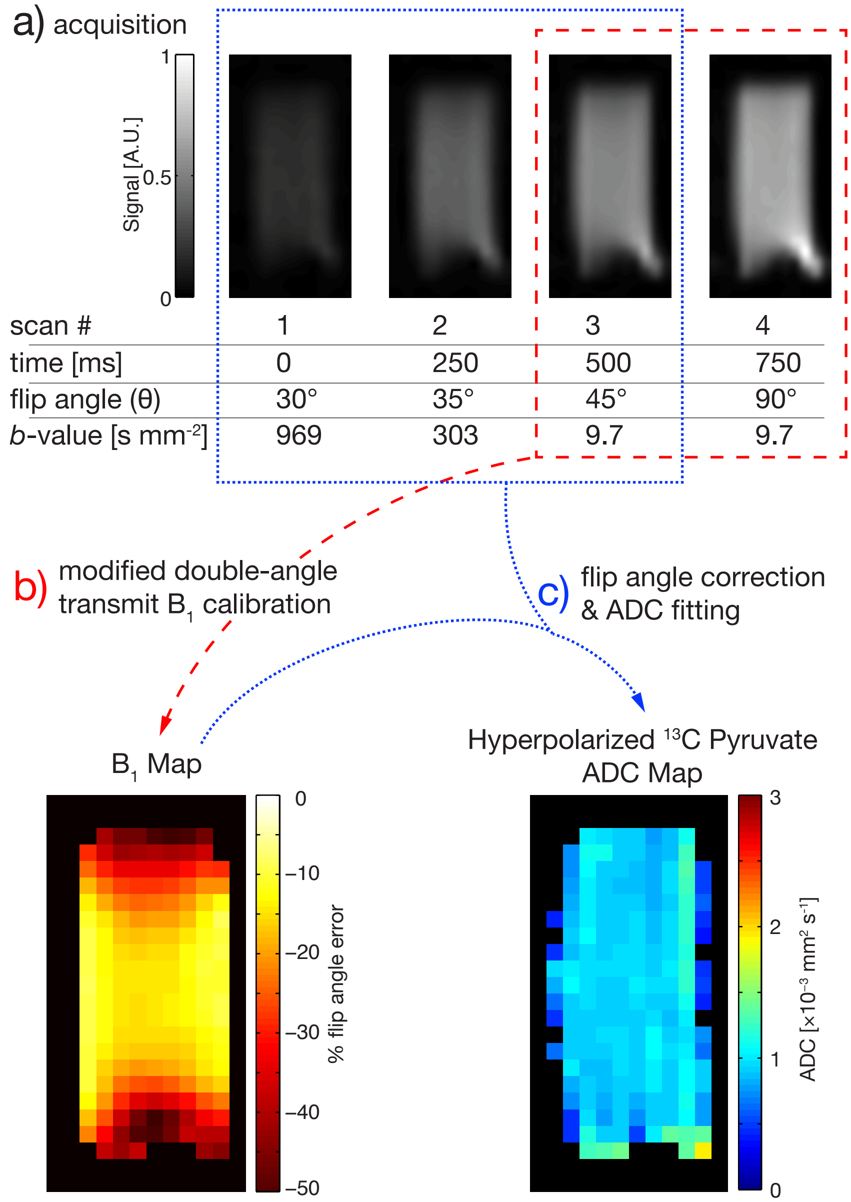


Figure 7.2: A schematic of the methodology presented here for acquiring hyperpolarized $^{13}$C metabolite diffusion weighted (DW) images and generating apparent diffusion coefficient (ADC) maps. The example data shown is a hyperpolarized $^{13}$C pyruvate phantom at 22°C. (**a**) Each metabolite is scanned 4 times within 1 s with varying flip angles and *b*-values. (**b**) The SNR of the last 2 images are compared with a modified double angle method to produce a $B_1$ map. (**c**) The $B_1$ map is used for a voxel-wise flip angle correction of each image. ADC maps are calculated using the first 3 images.

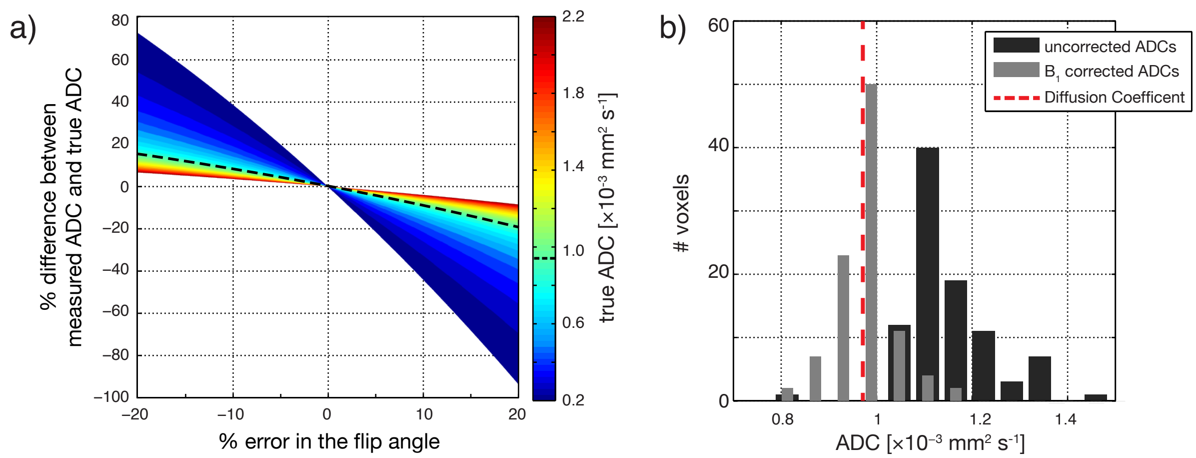


Figure 7.3: Flip angle correction of the images based on the simultaneously acquired $B_1$ map improves ADC measurement accuracy. (**a**) This simulation demonstrates the effect that flip angle errors have on measured ADC, using the parameters presented in Figure 7.2. The black dotted line represents the diffusion coefficient of pyruvate at 22°C. (**b**) The voxel-wise distribution of ADCs for the hyperpolarized $^{13}$C pyruvate phantom presented in Figure 7.2, before (*dark gray*) and after (*light gray*) a flip angle correction based on the $B_1$ map. The mean ADC of the corrected data aligns with the diffusion coefficient for pyruvate (*red dotted line*).

increased flip angles close to the rungs of the coil. Figure 7.3b shows the ADC distribution per voxel from a centered ROI in the hyperpolarized $^{13}$C pyruvate phantom ADC map (Figure 7.2c) both before (uncorrected) and after (corrected) flip angle correction. The mean ADC shifts 13%, from $1.12 \pm 0.05 \times 10^{-3}$ mm$^2$ s$^{-1}$ ($N_{vox} = 83$) to $0.97 \pm 0.05 \times 10^{-3}$ mm$^2$ s$^{-1}$ ($N_{vox} = 83$) (p-value $\ll 0.05$), where the latter agrees with previous diffusion coefficient measurements of pyruvate, $0.97 \times 10^{-3}$ mm$^2$ s$^{-1}$ [Koelsch *et al.*, 2013b]. The ADC measured from a hyperpolarized $^{13}$C lactate phantom was $0.92 \pm 0.10 \times 10^{-3}$ mm$^2$ s$^{-1}$ after the flip angle correction (data not shown), which also agrees with previous measurements, $0.88 \times 10^{-3}$ mm$^2$ s$^{-1}$ [Koelsch *et al.*, 2013b].

VFA schemes have been developed for hyperpolarized molecules to produce a constant signal response and allow for a complete exhaustion of the hyperpolarized magnetization [Zhao *et al.*, 1996; Nagashima, 2008]. DW MR experiments are characterized by signal loss corresponding to increasing $b$-values, which may lead to SNR limited images where noise can skew ADC calculations. To compensate for this effect and improve ADC measurement precision, we have created a diffusion compensated VFA scheme (Figure 7.4). In essence, for a given $b$-value scheme and an expected ADC, the diffusion compensated VFA scheme will produce images with constant SNR. Here, we used $D = 0.8 \times 10^{-3}$ mm$^2$ s$^{-1}$ and $b$-values = [1005, 314, 10, 10] s mm$^{-2}$, resulting in a VFA scheme where $\theta = [50°, 42°, 45°, 90°]$. The Monte Carlo simulation in Figure 7.4a compares the normalized ADCs for both the standard and the diffusion compensated VFA schemes. Signal from molecules with smaller and larger ADCs than that used to design the specific diffusion compensated VFA scheme ($0.3 \times 10^{-3}$ mm$^2$ s$^{-1}$ and $1.3 \times 10^{-3}$ mm$^2$ s$^{-1}$ in Figure 7.4a) will experience a slight signal decrease or increase, respectively, across the DW images with the given b-value scheme. Nevertheless, the diffusion compensated VFA scheme produces higher SNR at the high b-value images for these molecules and thereby also improves their ADC measurement precision. For the range of physiologically relevant ADCs presented and using the same diffusion compensated VFA scheme, tighter standard deviations show significantly improved measurement precision (p-value $< 0.05$ for all plotted pairs using Lavene's test for equality of variances). The greatest improvement in ADC measurement precision is seen at lower SNRs where the effect of noise can considerably skew ADC calculations. Figures 7.4c and 7.4d illustrate the SNR in the DW images of hyperpolarized $^{13}$C pyruvate and lactate with both the standard and the diffusion compensated VFA schemes. Acquired 1 hour apart, these images are from the same TRAMP mouse that had a small, early stage tumor.

### 7.4.2 In vivo ADC Mapping in Tumor Models

In vivo comparison of 1H water and hyperpolarized 13C pyruvate and lactate DW images and ADC maps in a brain tumor-bearing rat (Figure 7.5) shows how each of these may

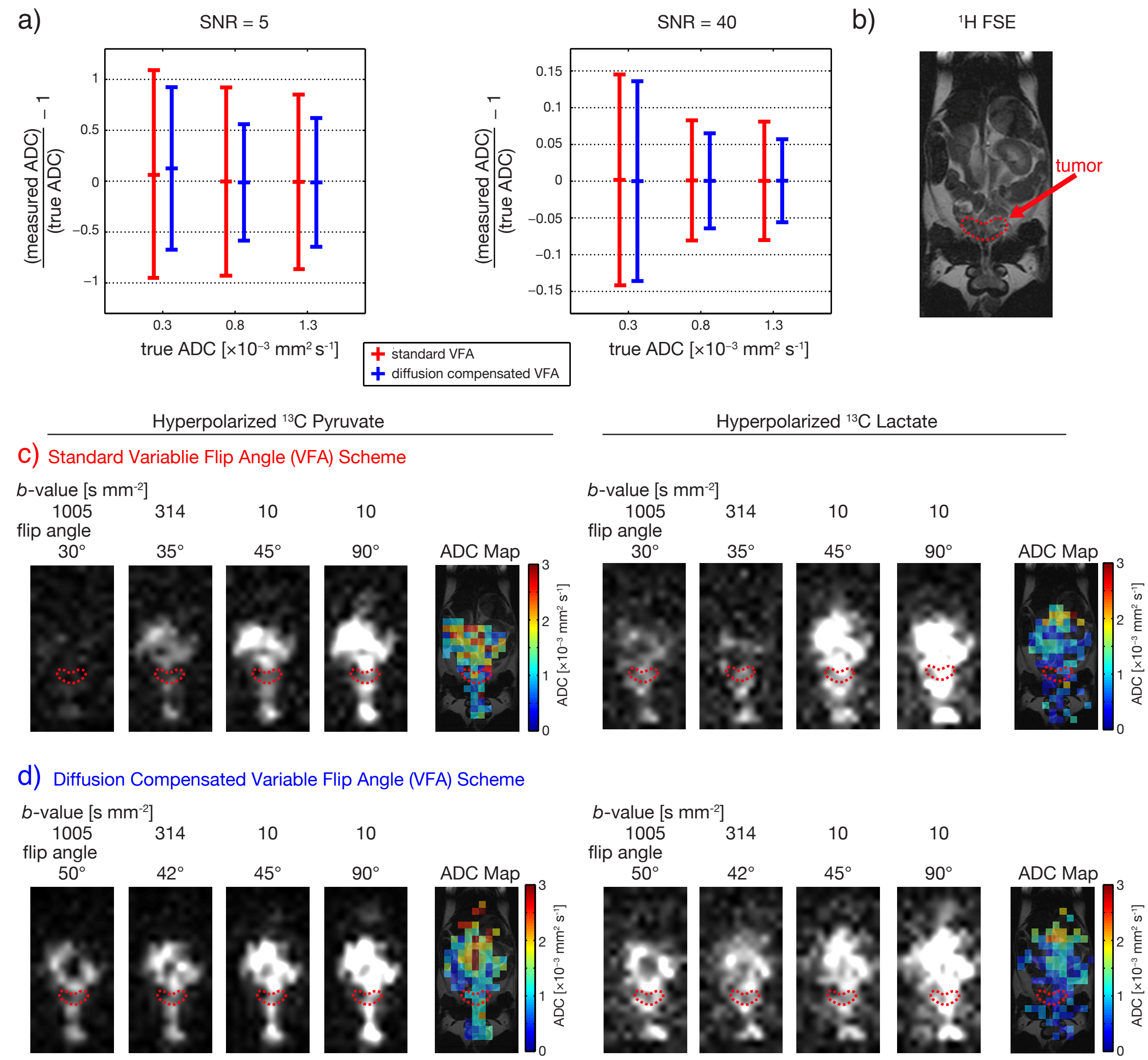


Figure 7.4: Using a VFA scheme that compensates for SNR loss due to diffusion weighting leads to greater ADC measurement precision. (**a**) Simulated DW data demonstrates smaller standard deviations and improved ADC measurement precision achieved with the diffusion compensated VFA scheme (*blue*) rather than the standard VFA scheme (*red*), both with low (*left*) and high (*right*) SNR. (**b**) A TRAMP mouse with a small tumor. (**c**) The DW images acquired with the standard VFA for both hyperpolarized $^{13}$C pyruvate and lactate show significantly decreased SNR at high *b*-values. (**d**) With the diffusion compensated VFA, the DW images of hyperpolarized $^{13}$C pyruvate and lactate have significantly improved SNR at higher *b*-values, which improves the precision of ADC measurements. The DW images in (c) and (d) were windowed to the same SNR for each metabolite to illustrate the SNR differences between the two schemes.

provide unique information. In general, brain tumors are characterized by increased water ADCs relative to the surrounding normal tissue [Kono *et al.*, 2001; Maier *et al.*, 2010]. This phenomenon is seen in the water ADC map (Figure 7.5b) where the mean ADC in the tumor region is $1.28 \pm 0.30 \times 10^{-3}$ mm$^2$ s$^{-1}$ ($N_{vox} = 334$), while the surrounding normal brains ADC is $0.84 \pm 0.18 \times 10^{-3}$ mm$^2$ s$^{-1}$ ($N_{vox} = 847$) (p-value $< 0.05$). Hyperpolarized $^{13}$C DW images were acquired with a standard VFA scheme. In comparison to the water ADC map, that of hyperpolarized $^{13}$C pyruvate (Figure 7.5c) does not show significant contrast between the tumor area, $0.60 \pm 0.36 \times 10^{-3}$ mm$^2$ s$^{-1}$ ($N_{vox} = 3$), and the surrounding normal brain, $0.71 \pm 0.24 \times 10^{-3}$ mm$^2$ s$^{-1}$ ($N_{vox} = 7$) (p-value $= 0.83$). This may be due to the fact that hyperpolarized $^{13}$C pyruvate is injected in large excess relative to how much is taken up by the cell. This means that while the vascular signal from hyperpolarized $^{13}$C pyruvate is reduced by applied diffusion gradients, the extracellular pyruvate signal still dominates the ADC measurements. Hyperpolarized $^{13}$C lactate (Figure 7.5d), however, does show a significant ADC decrease in the tumor, $0.17 \pm 0.03 \times 10^{-3}$ mm$^2$ s$^{-1}$ ($N_{vox} = 3$), in comparison to the surrounding tissue $0.44 \pm 0.14 \times 10^{-3}$ mm$^2$ s$^{-1}$ ($N_{vox} = 7$) (p-value $= 0.02$). These ADC differences between the normal brain and tumor tissue are indicative of microenvironments in which these molecules reside, suggesting that hyperpolarized $^{13}$C lactate resides in a more hindered environment in the tumor relative to normal brain than water. $^1$H and $^{13}$C DW image distortions are due to the single-shot EPI acquisition [Le Bihan *et al.*, 2006].

Hyperpolarized $^{13}$C pyruvate was injected into TRAMP mouse bearing a large prostate tumor. Figure 7.6 shows the low and high $b$-values DW images of hyperpolarized $^{13}$C lactate, acquired with the standard VFA scheme. The high $b$-value image clearly shows increased tumor contrast for lactate. Correspondingly, the ADC map shows decreased ADCs in the tumor region, $0.37 \pm 0.09 \times 10^{-3}$ mm$^2$ s$^{-1}$ ($N_{vox} = 8$), when compared to the immediately surrounding tissue, $0.79 \pm 0.18 \times 10^{-3}$ mm$^2$ s$^{-1}$ ($N_{vox} = 24$) (p-value $< 0.05$). The middle

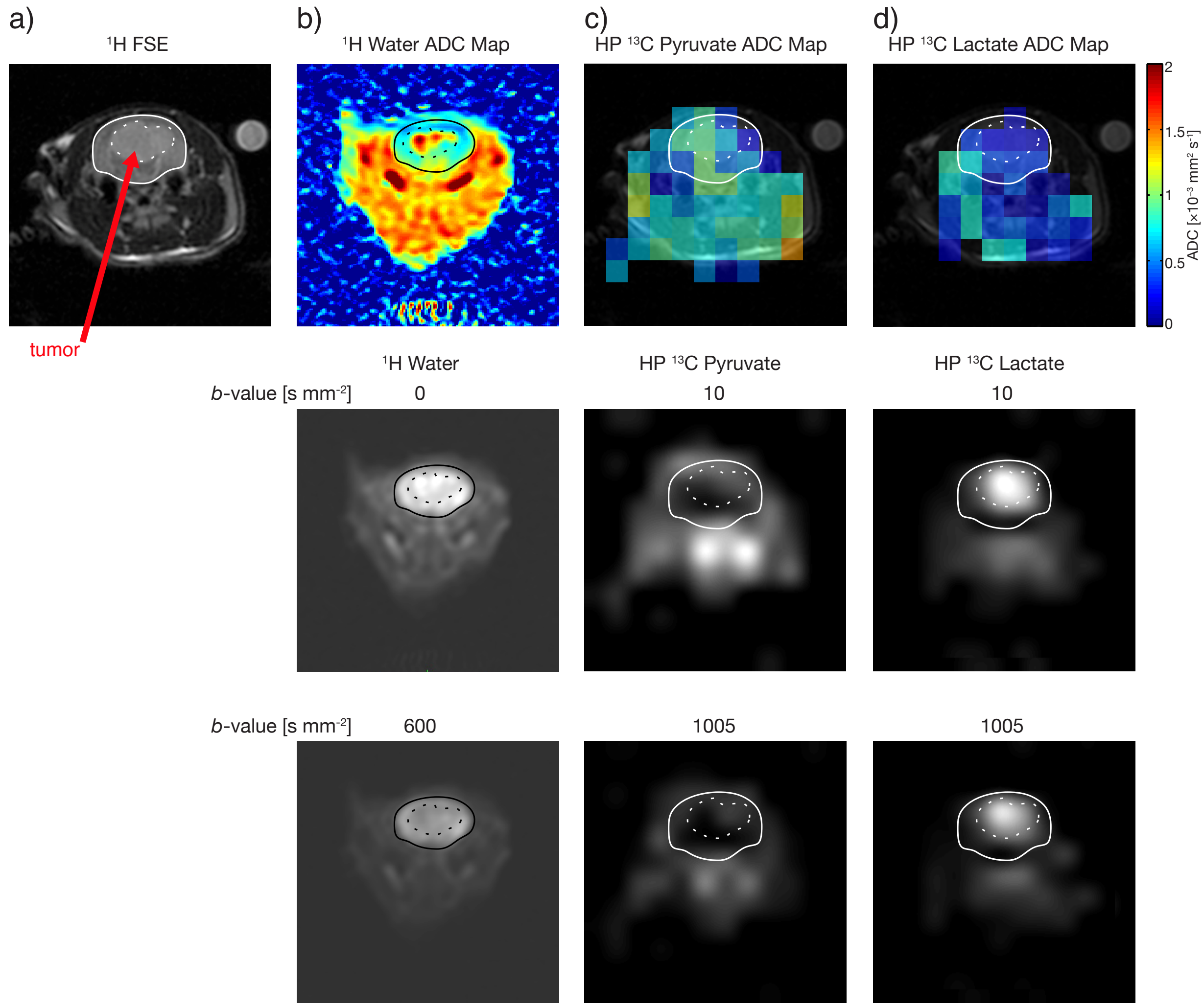


Figure 7.5: The ADC maps for water and hyperpolarized $^{13}$C pyruvate and lactate in a rat brain tumor model. (**a**) The proton FSE image with the brain (*solid line*) and the tumor (*dotted line*) outlined. (**b**) The water ADC map shows the tumor has an increased ADC relative to the surrounding normal brain tissue. Hyperpolarized $^{13}$C images were acquired with the standard VFA scheme. (**c**) The hyperpolarized $^{13}$C pyruvate ADC map showing relatively uniform ADCs across the normal brain and the tumor. (**d**) The ADC map of hyperpolarized $^{13}$C lactate shows a decreased tumor ADC relative to the surrounding tissue. The corresponding low and high *b*-value DW images are shown below.

$b$-value lactate image and all hyperpolarized $^{13}$C pyruvate DW images for this animal were unusable because signal loss due to respiratory motion. Similarly, water DW images were also unusable. Respiratory gating for these DW scans will be essential in future studies in the abdomen.

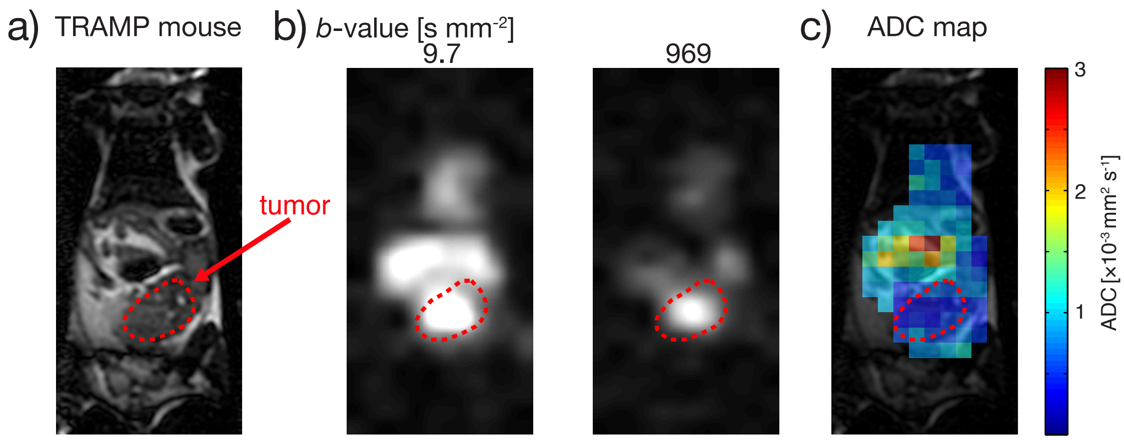


Figure 7.6: The ADC map of hyperpolarized $^{13}$C lactate prostate tumor bearing TRAMP mouse, acquired with the standard VFA scheme. (**a**) The proton FSE image with the tumor outlined. (**b**) The low and high $b$-value DW images of hyperpolarized $^{13}$C lactate. Improved tumor contrast can be seen with a high $b$-value. (**c**) The ADC map clearly shows a decreased ADC in the tumor region in comparison to the surrounding tissue in the abdomen.

### 7.4.3 ADC Mapping on Clinical-Ready Hardware

All experiments discussed henceforth used the $^{13}$C/$^{1}$H dual-tuned transmit/receive birdcage coil. The clamshell $^{13}$C transmit coil used in the recent clinical trial [Nelson *et al.*, 2013], however, is limited by its peak transmitter power and hence a low bandwidth stretched hyperbolic secant (HS$n$) refocusing pulse was employed. Figure 7.7 demonstrates the hyperpolarized $^{13}$C DW imaging and ADC mapping methodology developed here on clinical trial ready hardware. We injected a normal rat with hyperpolarized $^{13}$C HMCP and used the $^{13}$C clamshell transmit coil with the 8-channel array $^{13}$C receive coil. To ensure that the adiabatic pulses would fully refocus the transverse magnetization, the transmitter power was intentionally set higher than the adiabatic threshold. This also resulted in over-flipping with the spectral-spatial excitation pulses. While use of the diffusion compensated VFA scheme should produce relatively constant SNR for the acquired DW images, the decreasing DW image SNR with decreasing $b$-values (Figure 7.7b) shows the result of using larger than desired excitation pulses. The $B_1$ map (Figure 7.7c) confirms this over-excitation and shows a flip angle error of $22 \pm 2\%$ across the entire animal, where such a slowly varying distribution is expected for the clamshell transmit coil. Figure 7.7d shows the DW images after flip angle correction with the $B_1$ map. The ADC map of hyperpolarized $^{13}$C HMCP (Figure 7.7e) shows an average tissue ADC of $0.73 \pm 0.08 \times 10^{-3}$ mm$^2$ s$^{-1}$ ($N_{vox} = 70$) in the abdominal region. The regions of increased ADC appear in the center of the rat at the descending aorta and in a portion of the intestine on the right. For comparison, the solution ADC of HMCP at 22°C is $0.83 \pm 0.01 \times 10^{-3}$ mm$^2$ s$^{-1}$. We expect that HMCP resides only in vasculature and extracellular spaces, where it would have an ADC more similar to that in solution.

## 7.5 Discussion

### 7.5.1 Challenges of Hyperpolarized $^{13}$C ADC Mapping

Several factors limit the generation of quantitatively reliable ADC maps of hyperpolarized $^{13}$C molecules on a clinical MR scanner: 1) the small gyromagnetic ratio of $^{13}$C, 2) the limited maximum gradient amplitudes, 3) the highly dynamic nature of these signals due to metabolism and flow, 4) the non-renewable hyperpolarized magnetization and 5) the difficulty in accurately calibrating transmit $B_1$ powers.

The first two limitations can be overcome with the bipolar pulsed-gradient double spin echo sequence (Figure 7.1) that can produce $b$-values up to 1,000 s mm$^{-2}$, using 40 mT m$^{-1}$ gradient amplitudes and TE = 175–180 ms. The relatively long (0.2–1+ s) *in vivo* $T_2$s of the

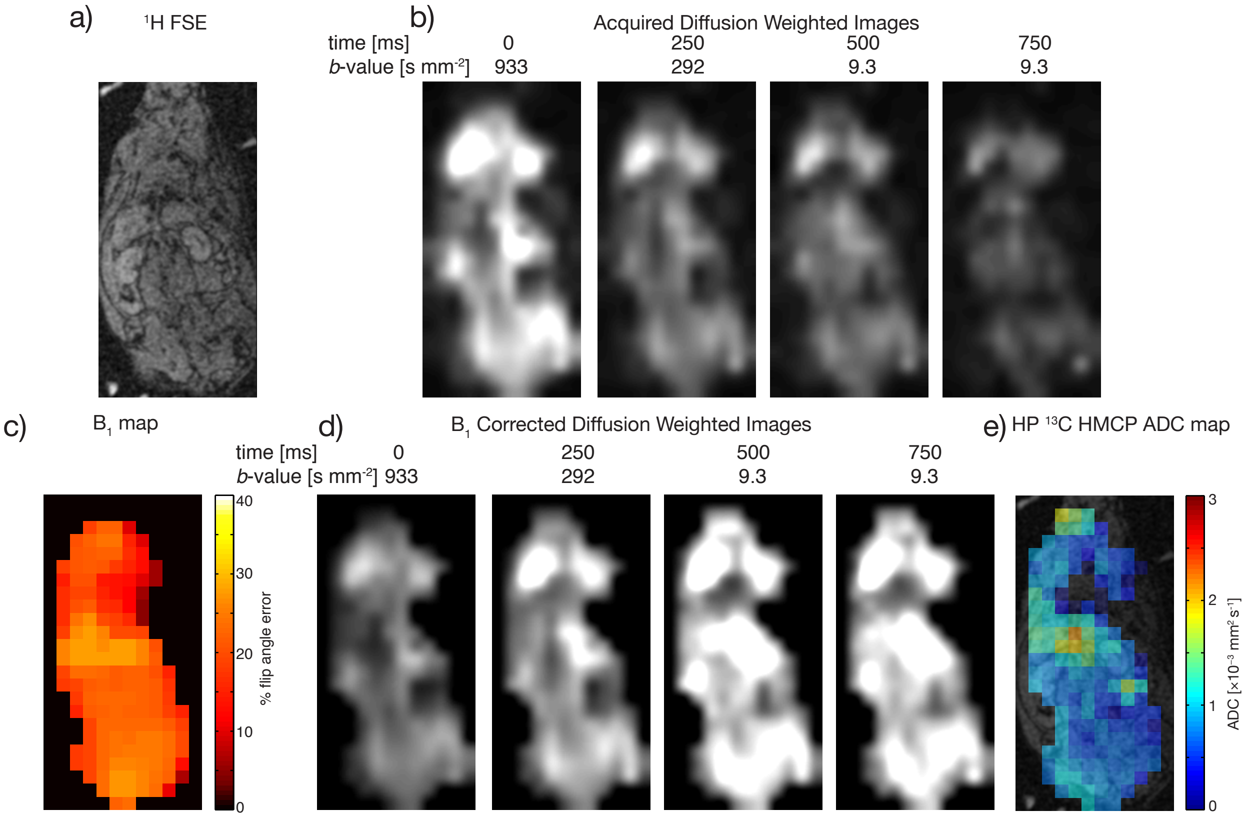


Figure 7.7: ADC mapping of hyperpolarized $^{13}$C HMCP in a normal rat using clinical trial-ready hardware. (**a**) The proton localizer image of the rat. (**b**) Having used a diffusion compensated VFA scheme and expecting constant SNR for all DW images, decreasing image SNR with decreasing *b*-values indicates that the transmitter power was too high. (**c**) The $B_1$ map reveals an average 22% $\pm$ 2 error in the flip angles and is use to correct the SNR in the DW images (**d**). (**e**) The resulting ADC map shows a homogeneous ADC in the abdomen with increased ADCs seen at the descending aorta and portion of the intestine.

$^{13}$C nuclei generally used for hyperpolarized studies [Kettunen *et al.*, 2013; Yen *et al.*, 2010; Reed *et al.*, 2014] allow for the long sequence TEs required in these studies to achieve sufficient diffusion weighting without resulting in significant $T_2$-weighting.

The third challenge, highly dynamic signals, is overcome by acquiring all diffusion images within a time period that is short relative to $T_1$, metabolism and flow effects (1 s per metabolite in our methodology), and thereby minimizing signal changes not due to diffusion.

The use of a VFA scheme overcomes the fourth and fifth limitations. By design, the VFA scheme maximizes total scan SNR by utilizing the entire pool of hyperpolarized magnetization over all acquisitions. The final two scans taken at 45° and 90° can be compared with a modified version of the double angle $B_1$ calibration method to correct for transmit power offsets. This simultaneously acquired $B_1$ map is subsequently used to flip angle correct the DW images and thereby improved the accuracy of the ADC calculations. With low SNR images, $B_1$ map accuracy will suffer. But, given that $B_1$ fields spatially vary slowly, spatial filters can be applied to the images to improve estimation of flip angle errors. Of course, where reliable $B_1$ maps have been previously measured, acquisition of only one low $b$-value image is necessary and redistribution of the non-renewable hyperpolarized magnetization will increase SNR in the other images. Finally, the diffusion compensated VFA scheme (Figure 7.4) increases image SNR at high $b$-values and improves the precision of ADC calculations. The optimal diffusion compensated VFA scheme depends on the scan parameters, such as the $b$-values and acquisition ordering, and the ADCs in the system under study.

ADC mapping of hyperpolarized $^{13}$C metabolites share several challenges with the hyperpolarized gas field. These include the difficulty in measuring transmit $B_1$ fields to implement accurate flip angles [Sogaard *et al.*, 2014] and the use of a VFA scheme to maximize image SNR of the non-renewable magnetization [Zhao *et al.*, 1996; Nagashima, 2008]. Yet, hyperpolarized gas ADC values are several orders of magnitude greater than those of tissue metabolites, for example $\approx 15$ mm$^2$ s for $^3$H in the normal lung [Chen *et al.*, 1999]. Correspondingly, $b$-values are merely 0.6 s mm$^{-2}$ and easily achievable with clinical gradient amplitudes and a simple pulsed gradient diffusion sequence [Yablonskiy *et al.*, 2002].

### 7.5.2 General Considerations for Hyperpolarized $^{13}$C ADC Mapping

ADC mapping of hyperpolarized $^{13}$C metabolites provides a means for understanding the local microstructure in which these molecules reside. The differences between the water and the hyperpolarized $^{13}$C pyruvate and lactate ADCs in the rat brain tumor model (Figure 7.5) indicate that these may provide unique information about diseased tissue. Understanding how the ADCs of hyperpolarized $^{13}$C metabolites change with tumor progression may prove to have a unique diagnostic value for cancer identification and characterization and monitoring of treatment response. In particular, hyperpolarized $^{13}$C lactate distribution between the extra- and intracellular may give information about tumor aggressiveness and metastatic potential, given that many metastatic tumors overexpress MCT4s, which rapidly transports lactate and its associated proton out of the cell [Gerlinger *et al.*, 2012; Gallagher *et al.*, 2007; Stock and Schwab, 2009].

The *in vivo* hyperpolarized $^{13}$C pyruvate and lactate values measured here are similar to those previously measured *in vivo* using hyperpolarized $^{13}$C spectroscopy on pre-clinical MR scanners [Kettunen *et al.*, 2013; Sogaard *et al.*, 2014]. Lactate generated from pyruvate had lower ADC values most likely because it has a larger intracellular fraction.

Additionally, the hyperpolarized $^{13}$C lactate ADCs in the rat brain tumor ($0.17 \pm 0.03 \times 10^{-3}$ mm$^2$ s$^{-1}$) and the TRAMP prostate tumor ($0.37 \pm 0.09 \times 10^{-3}$ mm$^2$ s$^{-1}$), acquired in 1 s, are similar to previous $^{1}$H spectroscopy measurements of thermally polarized lactate in tumors, acquired over several minutes: $0.23 \times 10^{-3}$ mm$^2$ s$^{-1}$ for steady-state $^{1}$H lactate using a double-quantum coherence-transfer technique [Sotak, 1991] and $0.13 \times 10^{-3}$ mm$^2$ s$^{-1}$ for [3-$^{13}$C] lactate using a $\{^{1}\text{H}–^{13}\text{C}\}$ editing technique [Pfeuffer *et al.*, 2005]. Differences between the ADC values measured here and those previously published could be due to unaccounted for anisotropic effects, incomplete compensation of non-diffusive signal changes, different tissue structure or higher intra-voxel fractions of extracellular or vascular hyperpolarized $^{13}$C lactate. The studies presented here foremost demonstrate the feasibility of rapidly measuring the ADCs of hyperpolarized $^{13}$C metabolites *in vivo*, while future studies will confirm the reproducibility of these measurements and correlate ADCs with disease states. Future studies are required to confirm the reproducibility of these measurements and more fully understand the biological/pathological underpinnings of the observed hyperpolarized $^{13}$C lactate ADC changes and how they relate to tumor grade.

ADC maps only show the effect of molecular motion in the directions that diffusion gradients have been applied. Clinically, diffusion gradients are applied in anywhere from 1 to 6 or more directions [Padhani *et al.*, 2009; Sugahara *et al.*, 1999; Nagarajan *et al.*, 2012], where more directions provide information about anisotropic tissue structure. In the work here, diffusion gradients were only applied in the through slice direction to maximize image SNR with the non-renewable hyperpolarized $^{13}$C signal. Future studies will explore the effects of tissue anisotropy on ADCs of hyperpolarized $^{13}$C molecules.

The $b$-values used clinically vary depending on the organ under study. For cancer applications, three $b$-values are recommended: a low $b$-value $\approx 0$ s mm$^{-2}$, a mid $b$-value $\geq 100$ s mm$^{-2}$ and a high $b$-value $\geq 500$ s mm$^{-2}$ [Padhani *et al.*, 2009]. With this in mind, the studies here used three $b$-values in these ranges to generate the ADC maps. Given differences in their distribution, however, the DW signal response of hyperpolarized $^{13}$C metabolites may not mirror that of water and depend on whether scans are of the injected hyperpolarized $^{13}$C molecule (e.g., pyruvate) or of a molecule that has been generated in cells via a metabolic pathway (e.g., lactate). Therefore, further studies must explore the optimal $b$-values needed for measuring hyperpolarized $^{13}$C metabolite ADCs.

Many studies have assessed the compartmentalization of molecules in tissue with multi-exponential fitting of the DW signal response, including for water [Clark and Le Bihan, 2000] and lactate [Pfeuffer *et al.*, 2005]. These approaches generally use $b$-values $\gg$ 1,000 s mm$^{-2}$ and bi-exponential fitting to measure fast and slow ADC values, attributed to extra- and intracellular fractions, respectively. Clinically, however, mono-exponential (or log-linear) fitting are most commonly used with high $b$-values $\approx$ 1,000 s mm$^{-2}$, as we have done here. In this case, ADCs show whether restricted or unrestricted environments dominate. Along with future studies on determining the optimal $b$-values for DW imaging, multi-exponential fitting will be implemented to explore the multiple diffusion compartments.

### 7.5.3 Translation to Humans

This study demonstrated that sufficiently high $b$-values can be obtained on a clinical MRI scanner for ADC measurements of hyperpolarized $^{13}$C metabolites. Moreover, techniques were developed for improving ADC measurement accuracy and precision using clinical RF coils and low-power pulses suitable for use in humans; see Figure 7.7.

The first human studies using hyperpolarized $^{13}$C pyruvate showed the production of hyperpolarized $^{13}$C lactate in regions of cancer with a SNR $\approx$ 5–15 [Nelson *et al.*, 2013]. This hyperpolarized $^{13}$C lactate SNR is similar to that observed in these studies when using minimal diffusion weighting: SNR $\approx$ 8–45. Additionally, the preliminary animal studies demonstrated significantly different tumor ADCs from surrounding tissues. Taken together, these results suggest that the SNR in humans will be sufficient to measure significantly different hyperpolarized $^{13}$C lactate ADCs in tumor regions. The techniques developed here to improve the ADC measurement accuracy and precision will also improve the test-retest reliability of the first in human hyperpolarized $^{13}$C ADC measurements.

## 7.6 Conclusion

In this study, we discussed a methodology for generating quantitatively reliable ADC maps of hyperpolarized $^{13}$C molecules. To our knowledge, these are the first *in vivo* ADC maps of hyperpolarized $^{13}$C metabolites on a commercial MRI system, which represents the first step towards clinical translation of this technique. To achieve sufficient diffusion weighting for the $^{13}$C molecules on a clinical MRI scanner, we employed a bipolar pulsed-gradient double spin echo sequence, generating $b$-values upwards of 1,000 s mm$^{-2}$ on a clinical MR scanner. ADC accuracy was improved with flip angle correction based on a simultaneously acquired $B_1$ map. ADC precision was improved with a diffusion compensated VFA scheme. Here we studied the ADCs of hyperpolarized $^{13}$C pyruvate, lactate and HMCP *in vivo*. ADC changes in these metabolites gives an indication of their microenvironment. In the case of hyperpolarized $^{13}$C lactate, ADC changes may provide useful information for the differentiation of indolent and metastatic tumors. Of course, these techniques can be used for any hyperpolarized $^{13}$C molecules to study their *in vivo* distribution between different microenvironments.

## 7.7 Supplemental Content

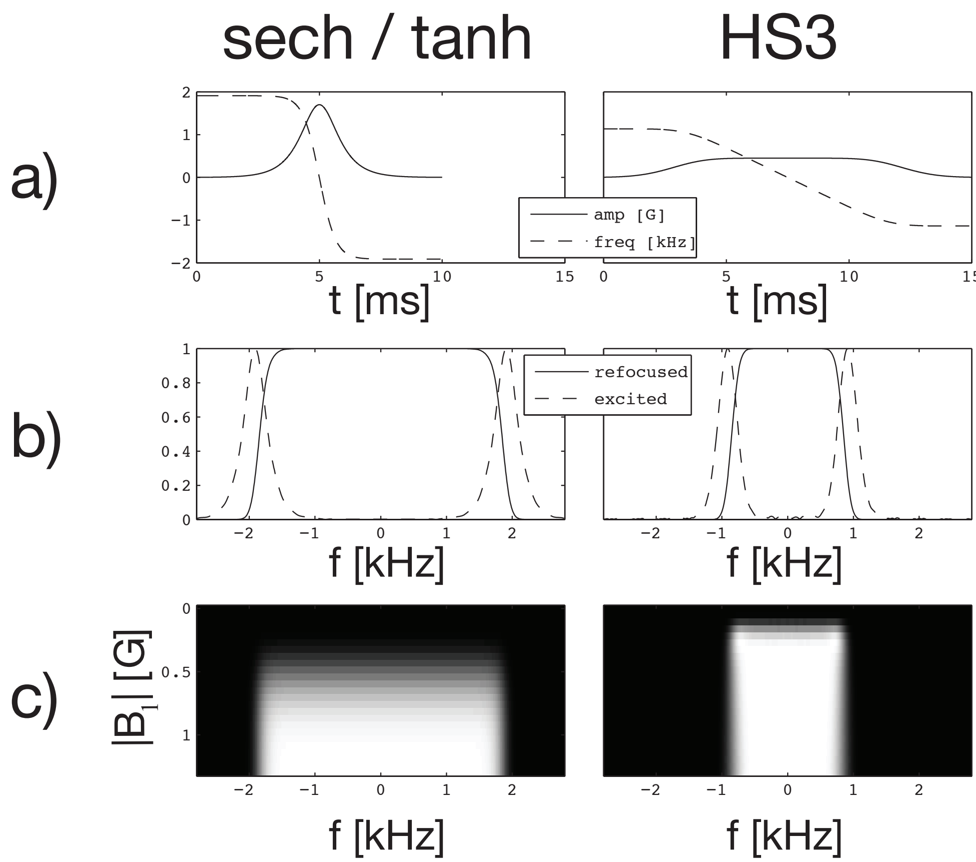


Figure 7.8: The two different adiabatic refocusing pulses used for diffusion weighting of hyperpolarized $^{13}$C molecules. The sech/tanh pulse (**left**) was used on the $^{13}$C/$^{1}$H dual-tuned transmit/receive birdcage coil, while the HS3 (*right*) was used on the clinical $^{13}$C transmit clamshell coil. (*a*) Amplitude and frequency modulation waveforms for the pulses. (**b**) The transverse refocused profile ($M_{xy} \rightarrow M_{xy}$) of both pulses above the adiabatic threshold. (**c**) The spin echo profile as a function of the $|B_1|$ amplitude variation.

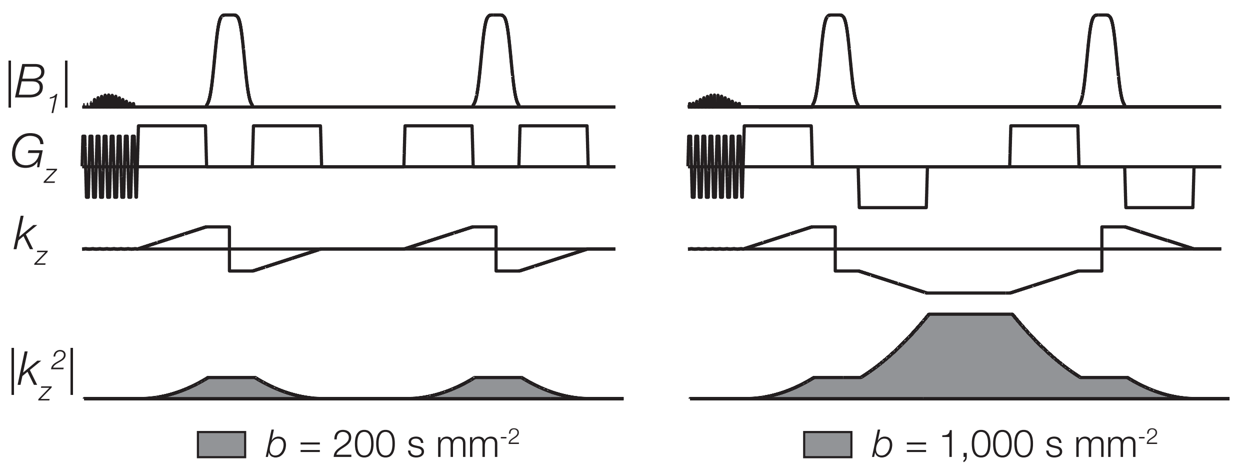


Figure 7.9: A comparison of the diffusion weighting (*b*-value) achievable with unipolar and bipolar pulsed gradient pairs using a double spin echo sequence. The small maximum gradient amplitudes on clinical MRI scanners (e.g., 4 G cm$^{-1}$) and the small $\gamma$ for $^{13}$C limits the ability to achieve large diffusion weightings with the hyperpolarized $^{13}$C metabolites. For the parameters used here (see Section 7.3.4), a 5× increase in the *b*-value is achieved by merely using bipolar gradients and thereby extending the diffusion sensitizing period, represented by the shaded area under $|k_z{}^2|$.

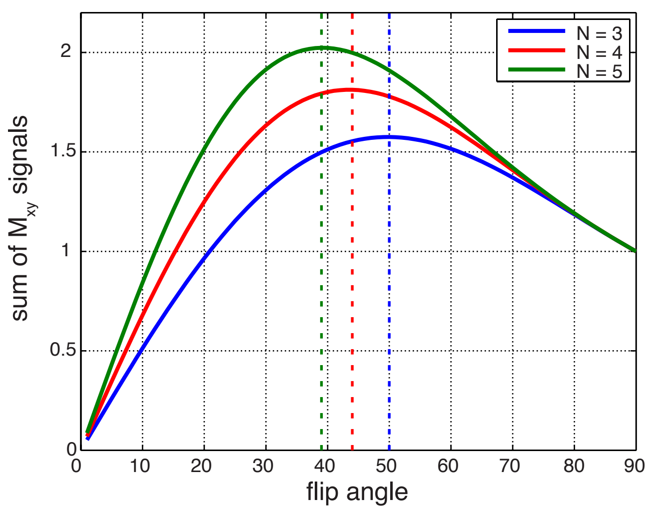


Figure 7.10: The optimal flip angle to use with a constant flip angle scheme that maximizes the total SNR for a hyperpolarized $^{13}C$ acquisition. While we use a variable flip angle scheme for all diffusion-weighted hyperpolarized $^{13}C$ acquisitions (Figure 7.2), this graph shows what flip angles would be necessary to maximize the total acquisition SNR if one were to use a constant flip angle scheme for the same number diffusion weighted images ($N = 3$–$5$). The graph shows the sum of all transverse signals ($M_{xy}$) for a small number (N) of excitations produced with a constant flip angle. The maximum for each curve (marked by the *dotted vertical line*) shows the optimal flip angle the will produce the maximum total SNR for all acquisitions: for $N = 3$, $\theta = 50°$; for $N = 4$, $\theta = 44°$; for $N = 5$, $\theta = 39°$.

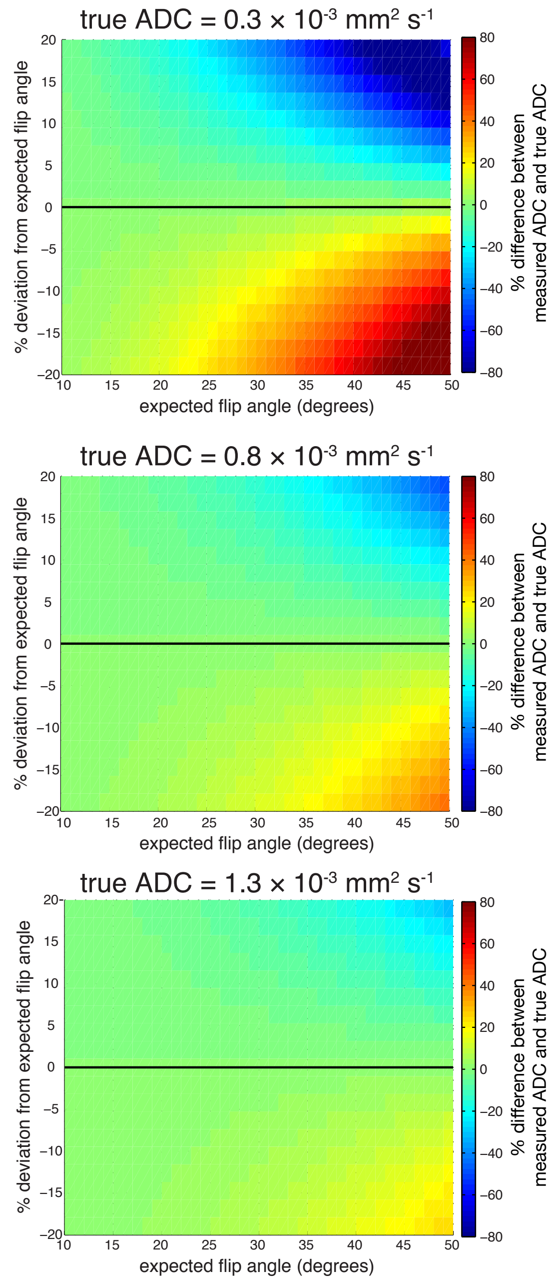


Figure 7.11: These graphs show the ADC measurement error that results from flip angle errors (up to $\pm$ 20%) using a constant flip angle scheme. Shown are the results for three different true ADCs that could be found *in vivo* for hyperpolarized $^{13}$C metabolites. Notice that at small flip angles (e.g., $\theta < 25°$) the ADC measurement error will be within $\pm$ 10%. But, at larger flip angles (e.g., $\theta > 40°$), the ADC measurements errors can exceed $\pm$ 40%, depending on the true ADC of the molecule being measured. The graphs show that molecules with smaller ADCs are more sensitive to flip angle errors. Recall from Figure 7.10 that for 4 excitations, the optimal flip angle is 44°.

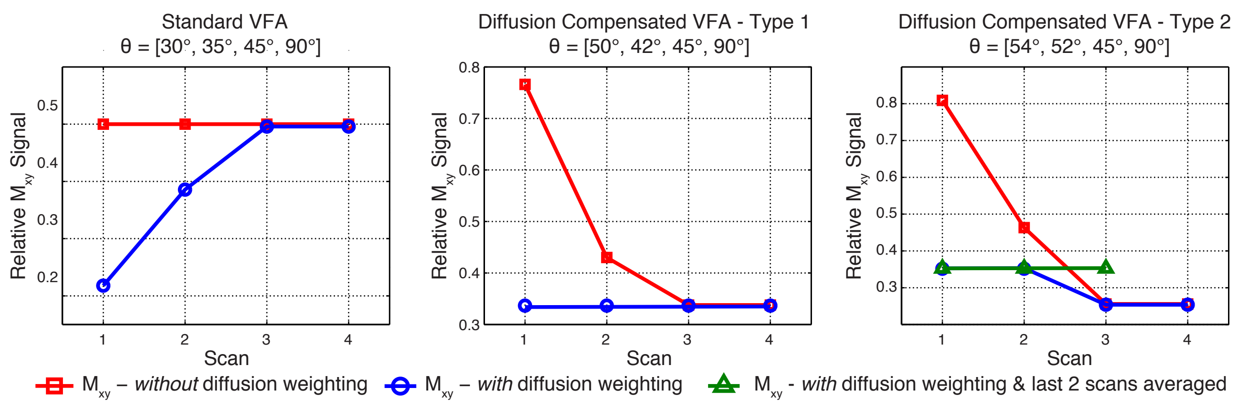


Figure 7.12: A comparison of the $M_{xy}$ signal for three different variable flip angle (VFA) schemes. The diffusion compensated VFA scheme, discussed in section 7.4.1, was designed produce constant SNR for four diffusion weighted images; here labeled diffusion compensated VFA-type 1 (*center*). The diffusion compensated VFA-type 2 (*left*) is designed for three scans and thus provides more SNR to each scan, relative to the diffusion compensated VFA-type 1. The SNR of the 3$^{rd}$ scan is distributed between two, low *b*-value scans (3 and 4) and thus still allows for the generation of a $B_1$ map. When these last two scans are averaged, the diffusion compensated VFA-type 2 produces a constant signal for all diffusion weighted images (*green line*). The signal for both the diffusion compensated VFA schemes must be flip angle corrected before ADCs are calculated.

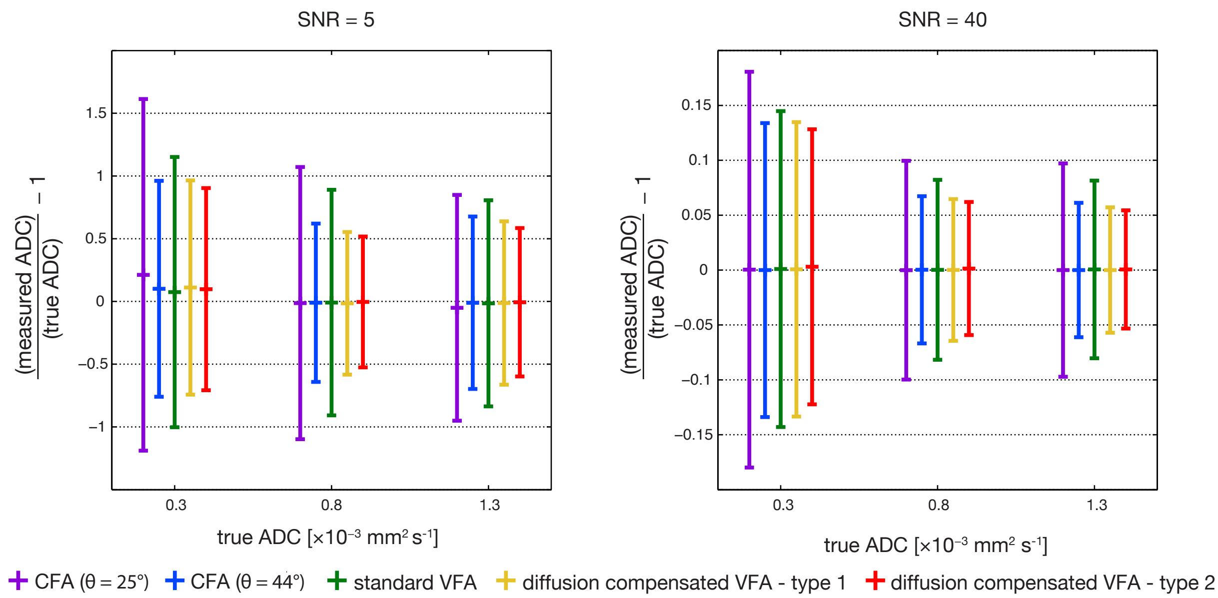


Figure 7.13: A Monte Carlo simulation showing that ADC measurement precision improves with high SNR for all diffusion weighted scans. These simulation were run with the same parameters as those in Figure 7.4. The constant flip angle (CFA) was run with both a commonly used flip angle (25°) and the optimal flip angle for 4 scans (44°), as defined in Figure 7.10. The standard variable flip angle (VFA) scheme has flip angles 30°, 35°, 45° and 90°. The diffusion compensated VFA-type 1, has flip angles 50°, 42°, 45° and 90°. The diffusion compensated VFA-type 2, as defined in Figure 7.12, has flip angles 54°, 52°, 45° and 90°. For the *b*-value scheme used here, high SNR for at the high *b*-value scans improves ADC measurement precision.

# Chapter 8

# Conclusion and Future Outlook

This dissertation presented the some of the first work on diffusion weighting of hyperpolarized $^{13}$C metabolites. In fact, the first three papers in this area were published within one month of one-another: one presenting studies in solution [Koelsch *et al.*, 2013b], one in cells [Schilling *et al.*, 2013] and one with *in vivo* work [Kettunen *et al.*, 2013]. Since then, several more papers and abstracts that use the technique have been published, all of which are trying to understand the extra- and intracellular distribution of the hyperpolarized $^{13}$ metabolites.

In Chapter 4 we presented a study demonstrating that highly aggressive, metastatic renal cell carcinoma cells actively transport hyperpolarized $^{13}$C lactate out of the cytoplasm through MCT4s. This study served as a motivation of developing diffusion weighted acquisition techniques for hyperpolarized $^{13}$C metabolites to study the extra- and intracellular distribution of these molecules. In Chapter 5 we developed and evaluated diffusion weighting of hyperpolarized $^{13}$C molecules in solution. Comparison with previously published values shows that these measurements can be done with high accuracy despite rapid loss characteristic of hyperpolarized molecules. These techniques were extended in Chapter 6 to study the molecules extra- and intracellularly. First, we measured the diffusion coefficients of these molecules in these two environments, where particularly the intracellular diffusion coefficients may be valuable for future *in vivo* studies that asses the tissue distribution of these molecules. Then, we used diffusion weighting to assess the dynamic extra- and intracellular distribution of several hyperpolarized $^{13}$C metabolites in metastatic renal cell carcinoma cells, showing that MCT4 inhibitors would increase the relative intracellular hyperpolarized $^{13}$C lactate. Finally, in Chapter 7 we present a methodology for acquiring diffusion weighted images of hyperpolarized $^{13}$C metabolites on a clinical MRI scanner. Using various novel acquisition techniques, we improve the accuracy and precision of these ADC maps. This work lays the foundation for clinical translation of diffusion weighting of hyperpolarized $^{13}$C metabolites. Ultimately, these techniques will enhance the characterization of tumors using hyperpolarized $^{13}$C metabolites by not allowing for metabolic flux measurements, but also the tissue distribution of these metabolites.

While this dissertation presents the technique development of diffusion weighting of hyperpolarized $^{13}$C metabolites and several validation experiments that these metabolites, like hyperpolarized $^{13}$C lactate, are actively transported during these experiments, much work remains to be done. Future studies, much of which will continue at UCSF, will compare ADC maps of these hyperpolarized $^{13}$C metabolites with those of water and use this information to characterize the influence of the tissue microenvironments on these various ADCs. Additionally, pre-clinical animal models of various forms of cancer, such as transgeneic TRAMP mice bearing prostate tumors, will be used to study the ADCs of hyperpolarized $^{13}$C metabolites with varying tumor aggressiveness. Of course, there are several technical aspects that can also be improved upon.

Thinking more broadly, it will be interesting to see how the role of hyperpolarized $^{13}$C will grow in the clinical setting. As of this writing, several university hospitals worldwide have purchased SpinLab polarizers for human studies. One thing is certain, there are plenty of projects that remain for researchers to explore, in order to identify the most powerful applications and techniques of hyperpolarized $^{13}C$.

# Bibliography


[Albers *et al.*, 2008] MJ Albers, R Bok, AP Chen, CH Cunningham, ML Zierhut, VY Zhang, SJ Kohler, J Tropp, RE Hurd, and YF Yen. Hyperpolarized 13C lactate, pyruvate, and alanine: noninvasive biomarkers for prostate cancer detection and grading. *Cancer Research*, 68(20):8607, 2008.

[Ardenkjær-Larsen *et al.*, 2003] JH Ardenkjær-Larsen, B Fridlund, A Gram, G Hansson, L Hansson, MH Lerche, R Servin, M Thaning, and K Golman. Increase in signal-to-noise ratio of¿ 10,000 times in liquid-state NMR. *Proceedings of the National Academy of Sciences of the United States of America*, 100(18):10158, 2003.

[Benga *et al.*, 1993] Gheorghe Benga, Bogdan E Chapman, Clifford H Gallagher, Desmond Cooper, and Philip W Kuchel. NMR studies of diffusional water permeability of red blood cells from macropodid marsupials (kangaroos and wallabies). *Comparative Biochemistry and Physiology Part A: Physiology*, 104(4):799–803, April 1993.

[Bernstein *et al.*, 2004] M A Bernstein, K F King, and X J Zhou. *Handbook of MRI Pulse Sequences*. Elsevier Science, 2004.

[Bhujwalla *et al.*, 2002] Z M Bhujwalla, D Artemov, P Ballesteros, S Cerdan, R J Gillies, and M Solaiyappan. Combined vascular and extracellular pH imaging of solid tumors. *NMR in Biomedicine*, 15(2):114–119, 2002.

[Bird *et al.*, 2002] R B Bird, W E Stewart, and E N Lightfoot. *Transport Phenomena*. John Wiley & Sons, 2 edition, 2002.

[Bloch, 1946] Felix Bloch. Nuclear induction. *Physical Review*, 70(7-8):460, 1946.

[Callaghan, 2011] P T Callaghan. *Translational Dynamics and Magnetic Resonance: Principles of Pulsed Gradient Spin Echo NMR*. Oxford University Press, New York, 2011.

[Carver and Slichter, 1953] T R Carver and C P Slichter. Polarization of nuclear spins in metals. *Physical Review*, 92(1):212, 1953.

[Chandrasekaran *et al.*, 2006] Prakash Chandrasekaran, Chris Seagle, Lisa Rice, Jeff Macdonald, and David A Gerber. Functional Analysis of Encapsulated Hepatic Progenitor Cells. *Tissue Engineering*, 12(7):2001–2008, July 2006.

[Chatham and Forder, 1996] J C Chatham and J R Forder. Metabolic compartmentation of lactate in the glucose-perfused rat heart. *American Journal of Physiology - Heart and Circulatory Physiology*, 270(1):H224–H229, January 1996.

[Chaumeil *et al.*, 2013] Myriam M Chaumeil, Peder E Z Larson, Hikari A I Yoshihara, Olivia M Danforth, Daniel B Vigneron, Sarah J Nelson, Russell O Pieper, Joanna J Phillips, and Sabrina M Ronen. Non-invasive in vivo assessment of IDH1 mutational status in glioma. *Nature Communications*, 4:2429, 2013.

[Chen and Shapiro, 1998] A Chen and M J Shapiro. NOE Pumping: A Novel NMR Technique for Identification of Compounds with Binding Affinity to Macromolecules. *Journal of the American Chemical Society*, 120(39):10258–10259, 1998.

[Chen and Shapiro, 1999] A Chen and M Shapiro. Nuclear Overhauser effect on diffusion measurements. *Journal of the American Chemical Society*, 121(22):5338–5339, 1999.

[Chen *et al.*, 1995] A Chen, D Wu, and C S Johnson Jr. Determination of molecular weight distributions for polymers by diffusion-ordered NMR. *Journal of the American Chemical Society*, 117(30):7965–7970, 1995.

[Chen *et al.*, 1999] X J Chen, H E Möller, M S Chawla, G P Cofer, B Driehuys, L W Hedlund, and G A Johnson. Spatially resolved measurements of hyperpolarized gas properties in the lung in vivo. Part I: diffusion coefficient. *Magnetic Resonance in Medicine*, 42(4):721–728, October 1999.

[Chen *et al.*, 2007] Albert P Chen, Mark J Albers, Charles H Cunningham, Susan J Kohler, Yi-Fen Yen, Ralph E Hurd, James Tropp, Robert Bok, John M Pauly, Sarah J Nelson, John Kurhanewicz, and Daniel B Vigneron. Hyperpolarized C-13 spectroscopic imaging of the TRAMP mouse at 3T-initial experience. *Magnetic Resonance in Medicine*, 58(6):1099–1106, December 2007.

[Chen *et al.*, 2008] Albert P Chen, John Kurhanewicz, Robert Bok, Duan Xu, David Joun, Vickie Zhang, Sarah J Nelson, Ralph E Hurd, and Daniel B Vigneron. Feasibility of using hyperpolarized [1-13C]lactate as a substrate for in vivo metabolic 13C MRSI studies. *Magnetic Resonance Imaging*, 26(6):721–726, July 2008.

[Chen *et al.*, 2012] Albert P Chen, Ralph E Hurd, and Charles H Cunningham. Spin tagging for hyperpolarized C metabolic studies. *Journal of magnetic resonance (San Diego, Calif. : 1997)*, 214(1):319–323, January 2012.

[Chow and Devesa, 2008] Wong-Ho Chow and Susan S Devesa. Contemporary Epidemiology of Renal Cell Cancer. *The Cancer Journal*, 14(5):288–301, September 2008.

[Clark and Le Bihan, 2000] C A Clark and D Le Bihan. Water diffusion compartmentation and anisotropy at high b values in the human brain. *Magnetic Resonance in Medicine*, 44(6):852–859, December 2000.

[Codd and Callaghan, 1999] SL Codd and PT Callaghan. Spin Echo Analysis of Restricted Diffusion under Generalized Gradient Waveforms: Planar, Cylindrical, and Spherical Pores with Wall Relaxivity. *Journal of magnetic resonance (San Diego, Calif. : 1997)*, 137(2):358–372, April 1999.

[Conolly *et al.*, 1989] S Conolly, D Nishimura, and A Macovski. A selective adiabatic spin-echo pulse. *Journal of Magnetic Resonance*, 1989.

[Cooperberg *et al.*, 2008] Matthew R Cooperberg, Katherine Mallin, Jamie Ritchey, Jacqueline D Villalta, Peter R Carroll, and Christopher J Kane. Decreasing size at diagnosis of stage 1 renal cell carcinoma: analysis from the National Cancer Data Base, 1993 to 2004. *The Journal of Urology*, 179(6):2131–2135, June 2008.

[Costello and Franklin, 2005] L C Costello and R B Franklin. 'Why do tumour cells glycolyse?': From glycolysis through citrate to lipogenesis - Springer. *Molecular and Cellular Biochemistry*, 2005.

[Crispen *et al.*, 2009] Paul L Crispen, Rosalia Viterbo, Stephen A Boorjian, Richard E Greenberg, David Y T Chen, and Robert G Uzzo. Natural history, growth kinetics, and outcomes of untreated clinically localized renal tumors under active surveillance. *Cancer*, 115(13):2844–2852, July 2009.

[Cunningham *et al.*, 2007] Charles H Cunningham, Albert P Chen, Mark J Albers, John Kurhanewicz, Ralph E Hurd, Yi-Fen Yen, John M Pauly, Sarah J Nelson, and Daniel B

Vigneron. Double spin-echo sequence for rapid spectroscopic imaging of hyperpolarized 13C. *Journal of Magnetic Resonance*, 187(2):357–362, August 2007.

[Curi *et al.*, 1988] R Curi, P Newsholme, and E A Newsholme. Metabolism of pyruvate by isolated rat mesenteric lymphocytes, lymphocyte mitochondria and isolated mouse macrophages. *The Biochemical Journal*, 250(2):383–388, March 1988.

[Day *et al.*, 2007] SE Day, MI Kettunen, FA Gallagher, DE Hu, M Lerche, J Wolber, K Golman, JH Ardenkjaer-Larsen, and KM Brindle. Detecting tumor response to treatment using hyperpolarized 13C magnetic resonance imaging and spectroscopy. *Nature Medicine*, 13(11):1382–1387, 2007.

[DeBerardinis *et al.*, 2008] Ralph J DeBerardinis, Julian J Lum, Georgia Hatzivassiliou, and Craig B Thompson. The biology of cancer: metabolic reprogramming fuels cell growth and proliferation. *Cell Metabolism*, 7(1):11–20, 2008.

[Dimmer *et al.*, 2000] K S Dimmer, B Friedrich, F Lang, J W Deitmer, and S Bröer. The low-affinity monocarboxylate transporter MCT4 is adapted to the export of lactate in highly glycolytic cells. *The Biochemical Journal*, 350 Pt 1:219–227, August 2000.

[Eggener *et al.*, 2006] Scott E Eggener, Ofer Yossepowitch, Joseph A Pettus, Mark E Snyder, Robert J Motzer, and Paul Russo. Renal cell carcinoma recurrence after nephrectomy for localized disease: predicting survival from time of recurrence. *Journal of clinical oncology: official journal of the American Society of Clinical Oncology*, 24(19):3101–3106, July 2006.

[Einstein, 1956] Albert Einstein. *Investigations on the Theory of the Brownian Movement*. Courier Dover Publications, 1956.

[Eliyahu *et al.*, 2007] Galit Eliyahu, Tamar Kreizman, and Hadassa Degani. Phosphocholine as a biomarker of breast cancer: molecular and biochemical studies. *International journal of cancer. Journal international du cancer*, 120(8):1721–1730, April 2007.

[Fielding, 2007] L Fielding. NMR methods for the determination of protein-ligand dissociation constants. *Progress in Nuclear Magnetic Resonance Spectroscopy*, 51(4):219–242, 2007.

[Gabellieri *et al.*, 2008] C Gabellieri, S Reynolds, A Lavie, GS Payne, MO Leach, and TR Eykyn. Therapeutic target metabolism observed using hyperpolarized 15N choline. *Journal of the American Chemical Society*, 130(14):4598–4599, 2008.

[Gallagher *et al.*, 2007] Shannon M Gallagher, John J Castorino, Dian Wang, and Nancy J Philp. Monocarboxylate transporter 4 regulates maturation and trafficking of CD147 to the plasma membrane in the metastatic breast cancer cell line MDA-MB-231. *Cancer Research*, 67(9):4182–4189, May 2007.

[Gallagher *et al.*, 2008] Ferdia A Gallagher, Mikko I Kettunen, Sam E Day, De-En Hu, Jan Henrik Ardenkjaer-Larsen, René in 't Zandt, Pernille R Jensen, Magnus Karlsson, Klaes Golman, Mathilde H Lerche, and Kevin M Brindle. Magnetic resonance imaging of pH in vivo using hyperpolarized 13C-labelled bicarbonate. *Nature*, 453(7197):940–943, June 2008.

[Gao *et al.*, 2008] Hongchang Gao, Baijun Dong, Xia Liu, Hanqing Xuan, Yiran Huang, and Donghai Lin. Metabonomic profiling of renal cell carcinoma: high-resolution proton nuclear magnetic resonance spectroscopy of human serum with multivariate data analysis. *Analytica chimica acta*, 624(2):269–277, August 2008.

[Gatenby and Gillies, 2004] RA Gatenby and RJ Gillies. Why do cancers have high aerobic glycolysis? *Nature Reviews Cancer*, 4(11):891–899, 2004.

[Gatenby and Gillies, 2008] Robert A Gatenby and Robert J Gillies. A microenvironmental model of carcinogenesis. *Nature Reviews Cancer*, 8(1):56–61, January 2008.

[Gatenby *et al.*, 2006] Robert A Gatenby, Edward T Gawlinski, Arthur F Gmitro, Brant Kaylor, and Robert J Gillies. Acid-mediated tumor invasion: a multidisciplinary study. *Cancer Research*, 66(10):5216–5223, May 2006.

[Gerlinger *et al.*, 2012] Marco Gerlinger, Claudio R Santos, Bradley Spencer-Dene, Pierre Martinez, David Endesfelder, Rebecca A Burrell, Marcus Vetter, Ming Jiang, Rebecca E Saunders, Gavin Kelly, Karl Dykema, Nathalie Rioux-Leclercq, Gordon Stamp, Jean-Jacques Patard, James Larkin, Michael Howell, and Charles Swanton. Genome-wide RNA interference analysis of renal carcinoma survival regulators identifies MCT4 as a Warburg effect metabolic target. *The Journal of Pathology*, 227(2):146–156, April 2012.

[Gillies and Gatenby, 2007a] Robert J Gillies and Robert A Gatenby. Adaptive landscapes and emergent phenotypes: why do cancers have high glycolysis? *Journal of Bioenergetics and Biomembranes*, 39(3):251–257, June 2007.

[Gillies and Gatenby, 2007b] Robert J Gillies and Robert A Gatenby. Hypoxia and adaptive landscapes in the evolution of carcinogenesis. *Cancer Metastasis Reviews*, 26(2):311–317, June 2007.

[Golman and Petersson, 2006] Klaes Golman and J Stefan Petersson. Metabolic imaging and other applications of hyperpolarized 13C1. *Academic radiology*, 13(8):932–942, August 2006.

[Golman *et al.*, 2001] K Golman, O Axelsson, H J hannesson, S M nsson, C Olofsson, and J S Petersson. Parahydrogen-induced polarization in imaging: Subsecond13C angiography. *Magnetic Resonance in Medicine*, 46(1):1–5, 2001.

[Golman *et al.*, 2006] Klaes Golman, René in t Zandt, and Mikkel Thaning. Real-time metabolic imaging. *Proceedings of the National Academy of Sciences of the United States of America*, 103(30):11270–11275, July 2006.

[Gordon *et al.*, 2013] Jeremy W Gordon, David J Niles, and Sean B Fain. Improved Measures of Renal Pyruvate-to-Lactate Conversion using Diffusion Gradients. *In Proceedings of the 21st Annual Meeting of ISMRM, Salt Lake City, Utah, USA*, 653, April 2013.

[Gosting and Akeley, 1952] L.J. Gosting and D.F. Akeley. A Study of the Diffusion of Urea in Water at 25 with the Gouy Interference Method1. *Journal of the American Chemical Society*, 74(8):2058–2060, 1952.

[Grossman *et al.*, 1985] H B Grossman, G Wedemeyer, and L Q Ren. Human renal carcinoma: characterization of five new cell lines. *Journal of surgical oncology*, 28(3):237–244, March 1985.

[Hahn, 1950] Erwin L Hahn. Spin echoes. *Physical Review*, 80(4):580, 1950.

[Halestrap and Price, 1999] A P Halestrap and N T Price. The proton-linked monocarboxylate transporter (MCT) family: structure, function and regulation. *The Biochemical Journal*, 343 Pt 2:281–299, October 1999.

[Hanahan and Weinberg, 2000] D Hanahan and R Weinberg. The Hallmarks of Cancer. *Cell*, 2000.

[Hanahan and Weinberg, 2011] Douglas Hanahan and Robert A Weinberg. Hallmarks of cancer: the next generation. *Cell*, 144(5):646–674, March 2011.

[Hill *et al.*, 2013] Deborah K Hill, Matthew R Orton, Erika Mariotti, Jessica K R Boult, Rafal Panek, Maysam Jafar, Harold G Parkes, Yann Jamin, Maria Falck Miniotis, Nada M S Al-Saffar, Mounia Beloueche-Babari, Simon P Robinson, Martin O Leach, Yuen-Li Chung, and Thomas R Eykyn. Model free approach to kinetic analysis of real-time hyperpolarized 13C magnetic resonance spectroscopy data. *PloS one*, 8(9):e71996, 2013.

[Holz *et al.*, 2000] Manfred Holz, Stefan R Heil, and Antonio Sacco. Temperature-dependent self-diffusion coefficients of water and six selected molecular liquids for calibration in accurate 1H NMR PFG measurements. *Physical Chemistry Chemical Physics*, 2(20):4740–4742, 2000.

[Hu *et al.*, 2008] Simon Hu, Michael Lustig, Albert P Chen, Jason Crane, Adam Kerr, Douglas A C Kelley, Ralph Hurd, John Kurhanewicz, Sarah J Nelson, John M Pauly, and Daniel B Vigneron. Compressed sensing for resolution enhancement of hyperpolarized 13C flyback 3D-MRSI. *Journal of Magnetic Resonance*, 192(2):258–264, June 2008.

[Hu *et al.*, 2009] Simon Hu, Peder E Z Larson, Adam B Kerr, D A Kelly, James Tropp, John M Pauly, John Kurhanewicz, and Daniel B Vigneron. Application of HSn Low Peak B1 Adiabatic Refocusing Pulse to Hyperpolarized 13C Spectoscopic Imaging. *In Proceedings of the 17th Annual Meeting of ISMRM, Honolulu, Hawaii, USA*, 333, January 2009.

[Inglis *et al.*, 2001] B A Inglis, E L Bossart, D L Buckley, E D Wirth, and T H Mareci. Visualization of neural tissue water compartments using biexponential diffusion tensor MRI. *Magnetic Resonance in Medicine*, 45(4):580–587, April 2001.

[Insko and Bolinger, 1993] E K Insko and L Bolinger. Mapping of the Radiofrequency Field. *Journal of Magnetic Resonance Series A*, 103(1):82–85, 1993.

[Jewett *et al.*, 2011] Michael A S Jewett, Kamal Mattar, Joan Basiuk, Christopher G Morash, Stephen E Pautler, D Robert Siemens, Simon Tanguay, Ricardo A Rendon, Martin E Gleave, Darrel E Drachenberg, Raymond Chow, Hannah Chung, Joseph L Chin, Neil E Fleshner, Andrew J Evans, Brenda L Gallie, Masoom A Haider, John R Kachura, Ghada Kurban, Kimberly Fernandes, and Antonio Finelli. Active surveillance of small renal masses: progression patterns of early stage kidney cancer. *European Urology*, 60(1):39–44, July 2011.

[Jones, 2011] D K Jones, editor. *Diffusion MRI: Theory, Methods, and Applications*. Oxford University Press, New York, 2011.

[Josan *et al.*, 2011] Sonal Josan, Yi-Fen Yen, Ralph Hurd, Adolf Pfefferbaum, Daniel Spielman, and Dirk Mayer. Application of double spin echo spiral chemical shift imaging to rapid metabolic mapping of hyperpolarized [113C]-pyruvate. *Journal of Magnetic Resonance*, 209(2):332–336, April 2011.

[Keshari and Wilson, 2014] Kayvan R Keshari and David M Wilson. Chemistry and biochemistry of 13C hyperpolarized magnetic resonance using dynamic nuclear polarization. *Chemical Society Reviews*, 43(5):1627, 2014.

[Keshari *et al.*, 2009] Kayvan R Keshari, David M Wilson, Albert P Chen, Robert Bok, Peder E Z Larson, Simon Hu, Mark Van Criekinge, Jeffrey M Macdonald, Daniel B Vigneron, and John Kurhanewicz. Hyperpolarized [2-13C]-fructose: a hemiketal DNP substrate for in vivo metabolic imaging. *Journal of the American Chemical Society*, 131(48):17591–17596, December 2009.

[Keshari *et al.*, 2010] KR Keshari, J Kurhanewicz, RE Jeffries, DM Wilson, BJ Dewar, M Van Criekinge, M Zierhut, DB Vigneron, and JM Macdonald. Hyperpolarized 13C spectroscopy and an NMRcompatible bioreactor system for the investigation of realtime cellular metabolism. *Magnetic Resonance in Medicine*, 63(2):322–329, 2010.

[Keshari *et al.*, 2011] Kayvan R Keshari, John Kurhanewicz, Robert Bok, Peder E Z Larson, Daniel B Vigneron, and David M Wilson. Hyperpolarized 13C dehydroascorbate as an endogenous redox sensor for in vivo metabolic imaging. *Proceedings of the National Academy of Sciences of the United States of America*, 108(46):18606–18611, November 2011.

[Keshari *et al.*, 2013] Kayvan R Keshari, Renuka Sriram, Bertram L Koelsch, Mark Van Criekinge, David M Wilson, John Kurhanewicz, and Zhen J Wang. Hyperpolarized 13C-pyruvate magnetic resonance reveals rapid lactate export in metastatic renal cell carcinomas. *Cancer Research*, 73(2):529–538, January 2013.

[Kettunen *et al.*, 2013] Mikko I Kettunen, Brett W C Kennedy, De-En Hu, and Kevin M Brindle. Spin echo measurements of the extravasation and tumor cell uptake of hyperpolarized [1-(13) C]lactate and [1-(13) C]pyruvate. *Magnetic Resonance in Medicine*, 70(5):1200–1209, November 2013.

[Kida and Uedaira, 1977] J. Kida and H. Uedaira. Selective measurements of the self-diffusion coefficients in acetic acid-water and methanol-water systems by pulsed-gradient fourier-transform NMR. *Journal of Magnetic Resonance*, 27(2):253–259, 1977.

[Koelsch *et al.*, 2013a] Bertram L Koelsch, Kayvan R Keshari, Tom H Peeters, Peder E Z Larson, David M Wilson, and John Kurhanewicz. Complete Separation of Extra- and Intracellular Hyperpolarized 13C Metabolite Signal with Diffusion Weighted MR. *In*

*Proceedings of the 21st Annual Meeting of ISMRM, Salt Lake City, Utah, USA*, 567, April 2013.

[Koelsch *et al.*, 2013b] Bertram L Koelsch, Kayvan R Keshari, Tom H Peeters, Peder E Z Larson, David M Wilson, and John Kurhanewicz. Diffusion MR of hyperpolarized 13C molecules in solution. *Analyst*, 138(4):1011, 2013.

[Koh *et al.*, 2007] Dow Mu Koh, Taro Takahara, Yutaka Imai, and David J Collins. Practical aspects of assessing tumors using clinical diffusion-weighted imaging in the body. *Magnetic resonance in medical sciences : MRMS : an official journal of Japan Society of Magnetic Resonance in Medicine*, 6(4):211–224, 2007.

[Kono *et al.*, 2001] K Kono, Y Inoue, K Nakayama, M Shakudo, M Morino, K Ohata, K Wakasa, and R Yamada. The role of diffusion-weighted imaging in patients with brain tumors. *AJNR. American journal of neuroradiology*, 22(6):1081–1088, June 2001.

[Koukourakis *et al.*, 2003] Michael I Koukourakis, Alexandra Giatromanolaki, and Efthimios Sivridis. Lactate Dehydrogenase Isoenzymes 1 and 5: Differential Expression by Neoplastic and Stromal Cells in Non-Small Cell Lung Cancer and Other Epithelial Malignant Tumors. *Tumor Biology*, 24(4):199–202, 2003.

[Kroemer and Pouyssegur, 2008] Guido Kroemer and Jacques Pouyssegur. Tumor cell metabolism: cancer's Achilles' heel. *Cancer Cell*, 13(6):472–482, June 2008.

[Kurhanewicz and Jurch, 1987] John Kurhanewicz and George R Jurch. Carbon-13 CIDNP investigation of the thermal decomposition of tert-butyl phenylperacetate. *Journal of the American Chemical Society*, 109(16):5038–5039, August 1987.

[Kurhanewicz *et al.*, 2008] John Kurhanewicz, Robert Bok, Sarah J Nelson, and Daniel B Vigneron. Current and potential applications of clinical 13C MR spectroscopy. *Journal of Nuclear Medicine*, 49(3):341–344, March 2008.

[Kurhanewicz *et al.*, 2011] J Kurhanewicz, D Vigneron, and K Brindle. Analysis of Cancer Metabolism by Imaging Hyperpolarized Nuclei: Prospects for Translation to Clinical Research. *Neoplasia*, 2011.

[Lam *et al.*, 2005] John S Lam, Oleg Shvarts, John T Leppert, Robert A Figlin, and Arie S Belldegrun. Renal cell carcinoma 2005: new frontiers in staging, prognostication and targeted molecular therapy. *The Journal of Urology*, 173(6):1853–1862, June 2005.

[Langbein *et al.*, 2008] Sigrun Langbein, Wilma M Frederiks, Axel zur Hausen, Juljane Popa, Jan Lehmann, Christel Weiss, Peter Alken, and Johannes F Coy. Metastasis is promoted by a bioenergetic switch: new targets for progressive renal cell cancer. *International journal of cancer. Journal international du cancer*, 122(11):2422–2428, June 2008.

[Larson *et al.*, 2012] Peder E Z Larson, Adam B Kerr, Galen D Reed, Ralph E Hurd, John Kurhanewicz, John M Pauly, and Daniel B Vigneron. Generating super stimulated-echoes in MRI and their application to hyperpolarized C-13 diffusion metabolic imaging. *IEEE Transactions on Medical Imaging*, 31(2):265–275, February 2012.

[Lau *et al.*, 2010] Angus Z Lau, Albert P Chen, Nilesh R Ghugre, Venkat Ramanan, Wilfred W Lam, Kim A Connelly, Graham A Wright, and Charles H Cunningham. Rapid multislice imaging of hyperpolarized 13C pyruvate and bicarbonate in the heart. *Magnetic Resonance in Medicine*, 64(5):1323–1331, November 2010.

[Lauterbur, 1973] Paul C Lauterbur. Image formation by induced local interactions: examples employing nuclear magnetic resonance. *Nature*, 242(5394):190–191, 1973.

[Le Bihan *et al.*, 1986] D Le Bihan, E Breton, D Lallemand, P Grenier, E Cabanis, and M Laval-Jeantet. MR imaging of intravoxel incoherent motions: application to diffusion and perfusion in neurologic disorders. *Radiology*, 161(2):401–407, November 1986.

[Le Bihan *et al.*, 2006] Denis Le Bihan, Cyril Poupon, Alexis Amadon, and Franck Lethimonnier. Artifacts and pitfalls in diffusion MRI. *Journal of Magnetic Resonance Imaging*, 24(3):478–488, September 2006.

[Levitt, 2008] M H Levitt. *Spin Dynamics: Basics of Nuclear Magnetic Resonance*. John Wiley & Sons, 2 edition, 2008.

[Longsworth, 1953] LG Longsworth. Diffusion Measurements, at 25 , of Aqueous Solutions of Amino Acids, Peptides and Sugars. *Journal of the American Chemical Society*, 75(22):5705–5709, 1953.

[Lundberg and Kuchel, 1997] P Lundberg and P W Kuchel. Diffusion of solutes in agarose and alginate gels: 1H and 23Na PFGSE and 23Na TQF NMR studies. *Magnetic Resonance in Medicine*, 37(1):44–52, January 1997.

[Maier *et al.*, 2010] Stephan E Maier, Yanping Sun, and Robert V Mulkern. Diffusion imaging of brain tumors. *NMR in Biomedicine*, 23(7):849–864, September 2010.

[Mayer *et al.*, 2012] Dirk Mayer, Yi-Fen Yen, Sonal Josan, Jae Mo Park, Adolf Pfefferbaum, Ralph E Hurd, and Daniel M Spielman. Application of hyperpolarized [1-13C]lactate for the in vivo investigation of cardiac metabolism. *NMR in Biomedicine*, 25(10):1119–1124, January 2012.

[Meyer *et al.*, 1990] C H Meyer, J M Pauly, A Macovski, and D G Nishimura. Simultaneous spatial and spectral selective excitation. *Magnetic Resonance in Medicine*, 15(2):287–304, August 1990.

[Millet *et al.*, 2011] Ingrid Millet, Fernanda Curros Doyon, Denis Hoa, Rodolphe Thuret, Samuel Merigeaud, Isabelle Serre, and Patrice Taourel. Characterization of small solid renal lesions: can benign and malignant tumors be differentiated with CT? *AJR. American journal of roentgenology*, 197(4):887–896, October 2011.

[Mills, 1973] R. Mills. Self-diffusion in normal and heavy water in the range 1-45. deg. *The Journal of Physical Chemistry*, 77(5):685–688, 1973.

[Miyake and Parsons, 2012] T Miyake and S J Parsons. Functional interactions between Choline kinase $\alpha$, epidermal growth factor receptor and c-Src in breast cancer cell proliferation. *Oncogene*, 31(11):1431–1441, March 2012.

[Möller *et al.*, 2002] Harald E Möller, X Josette Chen, Brian Saam, Klaus D Hagspiel, G Allan Johnson, Talissa A Altes, Eduard E de Lange, and Hans-Ulrich Kauczor. MRI of the lungs using hyperpolarized noble gases. *Magnetic Resonance in Medicine*, 47(6):1029–1051, June 2002.

[Montcourrier *et al.*, 1997] P Montcourrier, I Silver, R Farnoud, I Bird, and H Rochefort. Breast cancer cells have a high capacity to acidify extracellular milieu by a dual mechanism. *Clinical & Experimental Metastasis*, 15(4):382–392, July 1997.

[Nagarajan *et al.*, 2012] Rajakumar Nagarajan, Daniel Margolis, Steven Raman, Ke Sheng, Christopher King, Robert Reiter, and M Albert Thomas. Correlation of Gleason Scores with Diffusion-Weighted Imaging Findings of Prostate Cancer. *Advances in Urology*, 2012(2):1–5, 2012.

[Nagashima, 2008] Kaz Nagashima. Optimum pulse flip angles for multi-scan acquisition of hyperpolarized NMR and MRI. *Journal of Magnetic Resonance*, 190(2):183–188, February 2008.

[Nakanishi and Burg, 1989] T Nakanishi and M B Burg. Osmoregulation of glycerophosphorylcholine content of mammalian renal cells. *The American journal of physiology*, 257(4 Pt 1):C795–801, October 1989.

[Nelson *et al.*, 2008] S J Nelson, D Vigneron, J Kurhanewicz, A Chen, R Bok, and R Hurd. DNP-Hyperpolarized C Magnetic Resonance Metabolic Imaging for Cancer Applications. *Applied Magnetic Resonance*, 34(3-4):533–544, 2008.

[Nelson *et al.*, 2013] Sarah J Nelson, John Kurhanewicz, Daniel B Vigneron, Peder E Z Larson, Andrea L Harzstark, Marcus Ferrone, Mark Van Criekinge, Jose W Chang, Robert Bok, Ilwoo Park, Galen Reed, Lucas Carvajal, Eric J Small, Pamela Munster, Vivian K Weinberg, Jan Henrik Ardenkjaer-Larsen, Albert P Chen, Ralph E Hurd, Liv-Ingrid Odegardstuen, Fraser J Robb, James Tropp, and Jonathan A Murray. Metabolic imaging of patients with prostate cancer using hyperpolarized [1-C]pyruvate. *Science Translational Medicine*, 5(198):198ra108, August 2013.

[Nicolay *et al.*, 2001] Klaas Nicolay, Kees P J Braun, Robin A de Graaf, Rick M Dijkhuizen, and Marijn J Kruiskamp. Diffusion NMR spectroscopy. *NMR in Biomedicine*, 14(2):94–111, 2001.

[Nilsson *et al.*, 2008] Lina M Nilsson, Wendy E Thomas, Evgeni V Sokurenko, and Viola Vogel. Beyond Induced-Fit Receptor-Ligand Interactions: Structural Changes that Can Significantly Extend Bond Lifetimes. *Structure*, 16(7):1047–1058, July 2008.

[Ohliger *et al.*, 2013] Michael A Ohliger, Peder E Z Larson, Robert A Bok, Peter Shin, Simon Hu, James Tropp, Fraser Robb, Lucas Carvajal, Sarah J Nelson, John Kurhanewicz, and Daniel B Vigneron. Combined parallel and partial fourier MR reconstruction for accelerated 8-channel hyperpolarized carbon-13 in vivo magnetic resonance Spectroscopic imaging (MRSI). *Journal of Magnetic Resonance Imaging*, 38(3):701–713, January 2013.

[Overhauser, 1953] Albert W Overhauser. Polarization of nuclei in metals. *Physical Review*, 92(2):411, 1953.

[Padhani *et al.*, 2009] Anwar R Padhani, Guoying Liu, Dow Mu Koh, Thomas L Chenevert, Harriet C Thoeny, Taro Takahara, Andrew Dzik-Jurasz, Brian D Ross, Marc Van Cauteren, David Collins, Dima A Hammoud, Gordon J S Rustin, Bachir Taouli, and Peter L Choyke. Diffusion-weighted magnetic resonance imaging as a cancer biomarker: consensus and recommendations. In *Neoplasia (New York, N.Y.)*, pages 102–125. Mount Vernon Cancer Centre, London, UK., February 2009.

[Park *et al.*, 2006] Jang-Yeon Park, Lance DelaBarre, and Michael Garwood. Improved gradient-echo 3D magnetic resonance imaging using pseudo-echoes created by frequency-swept pulses. *Magnetic Resonance in Medicine*, 55(4):848–857, April 2006.

[Park *et al.*, 2010] Ilwoo Park, Peder E Z Larson, Matthew L Zierhut, Simon Hu, Robert Bok, Tomoko Ozawa, John Kurhanewicz, Daniel B Vigneron, Scott R Vandenberg, C David James, and Sarah J Nelson. Hyperpolarized 13C magnetic resonance metabolic imaging: application to brain tumors. *Neuro-oncology*, 12(2):133–144, February 2010.

[Patard, 2009] Jean-Jacques Patard. Incidental renal tumours. *Current opinion in urology*, 19(5):454–458, September 2009.

[Patrick *et al.*, 2014] P Stephen Patrick, Mikko I Kettunen, Sui-Seng Tee, Tiago B Rodrigues, Eva Serrao, Kerstin N Timm, Sarah McGuire, and Kevin M Brindle. Detection of transgene expression using hyperpolarized (13) C urea and diffusion-weighted magnetic resonance spectroscopy. *Magnetic Resonance in Medicine*, April 2014.

[Patyal *et al.*, 1997] B R Patyal, J H Gao, R F Williams, J Roby, B Saam, B A Rockwell, R J Thomas, D J Stolarski, and P T Fox. Longitudinal relaxation and diffusion measurements using magnetic resonance signals from laser-hyperpolarized 129Xe nuclei. *Journal of Magnetic Resonance*, 126(1):58–65, May 1997.

[Pfeuffer *et al.*, 1998] J Pfeuffer, W Dreher, E Sykova, and D Leibfritz. Water signal attenuation in diffusion-weighted 1 H NMR experiments during cerebral ischemia: influence of intracellular restrictions, extracellular tortuosity, and exchange. *Magnetic Resonance Imaging*, 16(9):1023–1032, 1998.

[Pfeuffer *et al.*, 2005] Josef Pfeuffer, Joseph C Lin, Lance DelaBarre, Kâmil Uğurbil, and Michael Garwood. Detection of intracellular lactate with localized diffusion 1H–13C-spectroscopy in rat glioma in vivo. *Journal of Magnetic Resonance*, 177(1):129–138, November 2005.

[Pilatus *et al.*, 1997] U Pilatus, H Shim, D Artemov, D Davis, P C Van Zijl, and J D Glickson. Intracellular volume and apparent diffusion constants of perfused cancer cell cultures, as measured by NMR. *Magnetic Resonance in Medicine*, 37(6):825–832, June 1997.

[Pinheiro *et al.*, 2012] Céline Pinheiro, Adhemar Longatto-Filho, João Azevedo-Silva, Margarida Casal, Fernando C Schmitt, and Fátima Baltazar. Role of monocarboxylate transporters in human cancers: state of the art. *Journal of Bioenergetics and Biomembranes*, 44(1):127–139, February 2012.

[Pollard *et al.*, 2005] P J Pollard, J J Brière, N A Alam, J Barwell, E Barclay, N C Wortham, T Hunt, M Mitchell, S Olpin, S J Moat, I P Hargreaves, S J Heales, Y L Chung, J R Griffiths, A Dalgleish, J A McGrath, M J Gleeson, S V Hodgson, R Poulsom, P Rustin, and I P M Tomlinson. Accumulation of Krebs cycle intermediates and over-expression of HIF1alpha in tumours which result from germline FH and SDH mutations. *Human molecular genetics*, 14(15):2231–2239, August 2005.

[Price *et al.*, 1999] William S Price, Hiroyuki Ide, and Yoji Arata. Self-Diffusion of Supercooled Water to 238 K Using PGSE NMR Diffusion Measurements. *The Journal of Physical Chemistry A*, 103(4):448–450, January 1999.

[Price *et al.*, 2002] William S Price, Fredrik Elwinger, C cile Vigouroux, and Peter Stilbs. PGSE-WATERGATE, a new tool for NMR diffusion-based studies of ligand-macromolecule binding. *Magnetic Resonance in Chemistry*, 40(6):391–395, 2002.

[Price, 2009] W S Price. *NMR Studies of Translational Motion: Principles and Applications* . Cambridge University Press, New York, 2009.

[Purcell *et al.*, 1946] E M Purcell, N Bloembergen, and R V Pound. Resonance Absorption by Nuclear Magnetic Moments in a Single Crystal of Ca F 2. *Physical Review*, 70(11-12):988, 1946.

[Rabi *et al.*, 1938] I I Rabi, J R Zacharias, S Millman, and P Kusch. A New Method of Measuring Nulcear Magnetic Moment. *Physical Review*, 53(2):318, February 1938.

[Reed *et al.*, 2014] Galen Reed, Cornelius von Morze, Robert Bok, Bertram Koelsch, Mark Van Criekinge, Kenneth Smith, Hong Shang, Peder Larson, John Kurhanewicz, and Daniel Vigneron. High Resolution C-13 MRI With Hyperpolarized Urea: In Vivo T2 Mapping and N-15 Labeling Effects. *IEEE Transactions on Medical Imaging*, 22(2), February 2014.

[Reese *et al.*, 2003] T G Reese, O Heid, R M Weisskoff, and V J Wedeen. Reduction of eddy-current-induced distortion in diffusion MRI using a twice-refocused spin echo. *Magnetic Resonance in Medicine*, 49(1):177–182, January 2003.

[Ryan *et al.*, 1994] M J Ryan, G Johnson, J Kirk, S M Fuerstenberg, R A Zager, and B Torok-Storb. HK-2: an immortalized proximal tubule epithelial cell line from normal adult human kidney. *Kidney International*, 45(1):48–57, 1994.

[Schilling *et al.*, 2013] Franz Schilling, Stephan Düwel, Ulrich Köllisch, Markus Durst, Rolf F Schulte, Steffen J Glaser, Axel Haase, Angela M Otto, and Marion I Menzel. Diffusion of hyperpolarized (13) C-metabolites in tumor cell spheroids using real-time NMR spectroscopy. *NMR in Biomedicine*, 26(5):557–568, May 2013.

[Schulte *et al.*, 2013] Rolf F Schulte, Jonathan I Sperl, Eliane Weidl, Marion I Menzel, Martin A Janich, Oleksandr Khegai, Markus Durst, Jan Henrik Ardenkjaer-Larsen, Steffen J Glaser, Axel Haase, Markus Schwaiger, and Florian Wiesinger. Saturation-recovery metabolic-exchange rate imaging with hyperpolarized [1-13C] pyruvate using spectral-spatial excitation. *Magnetic Resonance in Medicine*, 69(5):1209–1216, May 2013.

[Semenza, 2003] Gregg L Semenza. Targeting HIF-1 for cancer therapy. *Nature Reviews Cancer*, 3(10):721–732, 2003.

[Semenza, 2007] Gregg L Semenza. HIF-1 mediates the Warburg effect in clear cell renal carcinoma. *Journal of Bioenergetics and Biomembranes*, 39(3):231–234, June 2007.

[Shah *et al.*, 2010] Tariq Shah, Flonne Wildes, Marie-France Penet, Paul T Winnard, Kristine Glunde, Dmitri Artemov, Ellen Ackerstaff, Barjor Gimi, Samata Kakkad, Venu Raman, and Zaver M Bhujwalla. Choline kinase overexpression increases invasiveness and drug resistance of human breast cancer cells. *NMR in Biomedicine*, 23(6):633–642, July 2010.

[Shannon *et al.*, 2008] Beverley A Shannon, Ronald J Cohen, Hildemarie de Bruto, and Robert J Davies. The value of preoperative needle core biopsy for diagnosing benign lesions among small, incidentally detected renal masses. *The Journal of Urology*, 180(4):1257–61–discussion 1261, October 2008.

[Sickmann *et al.*, 2005] Helle M Sickmann, Arne Schousboe, Keld Fosgerau, and Helle S Waagepetersen. Compartmentation of lactate originating from glycogen and glucose in cultured astrocytes. *Neurochemical research*, 30(10):1295–1304, October 2005.

[Siegel *et al.*, 2012] Rebecca Siegel, Deepa Naishadham, and Ahmedin Jemal. Cancer statistics, 2012. *CA: a cancer journal for clinicians*, 62(1):10–29, January 2012.

[Slichter, 1990] C P Slichter. *Principles of Magnetic Resonance*. Springer, 1990.

[Sogaard *et al.*, 2014] Lise Vejby Sogaard, Franz Schilling, Martin A Janich, Marion I Menzel, and Jan Henrik Ardenkjaer-Larsen. In vivo measurement of apparent diffusion coefficients of hyperpolarized C-labeled metabolites. *NMR in Biomedicine*, 27(5):561–569, May 2014.

[Sotak, 1991] C H Sotak. Multiple quantum NMR spectroscopy methods for measuring the apparent self-diffusion coefficient of in vivo lactic acid. *NMR in Biomedicine*, 4(2):70–72, April 1991.

[Stejskal and Tanner, 1965] EO Stejskal and JE Tanner. Spin diffusion measurements: spin echoes in the presence of a time-dependent field gradient. *The Journal of Chemical Physics*, 42(1):288, 1965.

[Stock and Schwab, 2009] Christian Stock and Albrecht Schwab. Protons make tumor cells move like clockwork. *Pflügers Archiv : European journal of physiology*, 458(5):981–992, September 2009.

[Sudarshan *et al.*, 2009] Sunil Sudarshan, Carole Sourbier, Hye-Sik Kong, Karen Block, Vladimir A Valera Romero, Youfeng Yang, Cynthia Galindo, Mehdi Mollapour, Bradley Scroggins, Norman Goode, Min-Jung Lee, Campbell W Gourlay, Jane Trepel, W Marston Linehan, and Len Neckers. Fumarate Hydratase Deficiency in Renal Cancer Induces Glycolytic Addiction and Hypoxia-Inducible Transcription Factor 1 alpha Stabilization by Glucose-Dependent Generation of Reactive Oxygen Species. *Molecular And Cellular Biology*, 29(15):4080–4090, 2009.

[Sugahara *et al.*, 1999] T Sugahara, Y Korogi, M Kochi, I Ikushima, Y Shigematu, T Hirai, T Okuda, L Liang, Y Ge, Y Komohara, Y Ushio, and M Takahashi. Usefulness of diffusion-weighted MRI with echo-planar technique in the evaluation of cellularity in gliomas. *Journal of Magnetic Resonance Imaging*, 9(1):53–60, January 1999.

[Sun *et al.*, 2011] Maxine Sun, Shahrokh F Shariat, Christopher Cheng, Vincenzo Ficarra, Masaru Murai, Stéphane Oudard, Allan J Pantuck, Richard Zigeuner, and Pierre I Karakiewicz. Prognostic factors and predictive models in renal cell carcinoma: a contemporary review. *European Urology*, 60(4):644–661, October 2011.

[Swietach *et al.*, 2007] Pawel Swietach, Richard D Vaughan-Jones, and Adrian L Harris. Regulation of tumor pH and the role of carbonic anhydrase 9. *Cancer Metastasis Reviews*, 26(2):299–310, June 2007.

[Tanner and Stejskal, 1968] JE Tanner and EO Stejskal. Restricted SelfDiffusion of Protons in Colloidal Systems by the PulsedGradient, SpinEcho Method. *The Journal of Chemical Physics*, 49:1768, 1968.

[Torrey, 1956] H.C. Torrey. Bloch equations with diffusion terms. *Physical Review*, 104(3):563, 1956.

[Ullah *et al.*, 2006] Mohammed S Ullah, Andrew J Davies, and Andrew P Halestrap. The plasma membrane lactate transporter MCT4, but not MCT1, is up-regulated by hypoxia through a HIF-1alpha-dependent mechanism. *Journal Of Biological Chemistry*, 281(14):9030–9037, April 2006.

[Unwin *et al.*, 2003] Richard D Unwin, Rachel A Craven, Patricia Harnden, Sarah Hanrahan, Nick Totty, Margaret Knowles, Ian Eardley, Peter J Selby, and Rosamonde E Banks. Proteomic changes in renal cancer and co-ordinate demonstration of both the glycolytic and mitochondrial aspects of the Warburg effect. *Proteomics*, 3(8):1620–1632, August 2003.

[Van Zijl *et al.*, 1991] P C Van Zijl, C T Moonen, P Faustino, J Pekar, O Kaplan, and J S Cohen. Complete separation of intracellular and extracellular information in NMR spectra of perfused cells by diffusion-weighted spectroscopy. *Proceedings of the National Academy of Sciences of the United States of America*, 88(8):3228–3232, April 1991.

[Vander Heiden *et al.*, 2009] Matthew G Vander Heiden, Lewis C Cantley, and Craig B Thompson. Understanding the Warburg effect: the metabolic requirements of cell proliferation. *Science*, 324(5930):1029–1033, May 2009.

[Volpe *et al.*, 2008] Alessandro Volpe, Kamal Mattar, Antonio Finelli, John R Kachura, Andrew J Evans, William R Geddie, and Michael A S Jewett. Contemporary results of percutaneous biopsy of 100 small renal masses: a single center experience. *The Journal of Urology*, 180(6):2333–2337, December 2008.

[von Morze *et al.*, 2013] Cornelius von Morze, Robert A Bok, Galen D Reed, Jan Henrik Ardenkjaer-Larsen, John Kurhanewicz, and Daniel B Vigneron. Simultaneous multiagent hyperpolarized (13) C perfusion imaging. *Magnetic Resonance in Medicine*, December 2013.

[Warburg, 1956] O Warburg. On the origin of cancer cells. *Science*, 123(3191):309–314, February 1956.

[Webb *et al.*, 2011] Bradley A Webb, Michael Chimenti, Matthew P Jacobson, and Diane L Barber. Dysregulated pH: a perfect storm for cancer progression. *Nature Reviews Cancer*, 11(9):671–677, September 2011.

[Wilson *et al.*, 2009] David M Wilson, Ralph E Hurd, Kayvan Keshari, Mark Van Criekinge, Albert P Chen, Sarah J Nelson, Daniel B Vigneron, and John Kurhanewicz. Generation of hyperpolarized substrates by secondary labeling with [1,1-C-13] acetic anhydride. *Proceedings of the National Academy of Sciences of the United States of America*, 106(14):5503–5507, 2009.

[Wilson *et al.*, 2010] David M Wilson, Kayvan R Keshari, Peder E Z Larson, Albert P Chen, Simon Hu, Mark Van Criekinge, Robert Bok, Sarah J Nelson, Jeffrey M Macdonald, Daniel B Vigneron, and John Kurhanewicz. Multi-compound polarization by DNP allows simultaneous assessment of multiple enzymatic activities in vivo. *Journal of Magnetic Resonance*, 205(1):141–147, July 2010.

[Wise and Thompson, 2010] David R Wise and Craig B Thompson. Glutamine addiction: a new therapeutic target in cancer. *Trends in biochemical sciences*, 35(8):427–433, August 2010.

[Witney *et al.*, 2010] T H Witney, M I Kettunen, D-e Hu, F A Gallagher, S E Bohndiek, R Napolitano, and K M Brindle. Detecting treatment response in a model of human breast adenocarcinoma using hyperpolarised [1-13C]pyruvate and [1,4-13C2]fumarate. *British Journal of Cancer*, 103(9):1400–1406, October 2010.

[Yablonskiy *et al.*, 2002] Dmitriy A Yablonskiy, Alexander L Sukstanskii, Jason C Leawoods, David S Gierada, G Larry Bretthorst, Stephen S Lefrak, Joel D Cooper, and Mark S Conradi. Quantitative in vivo assessment of lung microstructure at the alveolar level with hyperpolarized 3He diffusion MRI. *Proceedings of the National Academy of Sciences of the United States of America*, 99(5):3111–3116, March 2002.

[Yang *et al.*, 2010] Youfeng Yang, Vladimir A Valera, Hesed M Padilla-Nash, Carole Sourbier, Cathy D Vocke, Manish A Vira, Mones S Abu-Asab, Gennady Bratslavsky, Maria Tsokos, Maria J Merino, Peter A Pinto, Ramaprasad Srinivasan, Thomas Ried, Len Neckers, and W Marston Linehan. UOK 262 cell line, fumarate hydratase deficient (FH-/FH-) hereditary leiomyomatosis renal cell carcinoma: in vitro and in vivo model of an aberrant energy metabolic pathway in human cancer. *Cancer Genetics and Cytogenetics*, 196(1):45–55, 2010.

[Yen *et al.*, 2010] Yi-Fen Yen, Patrick Le Roux, Dirk Mayer, Randy King, Daniel Spielman, James Tropp, Kim Butts Pauly, Adolf Pfefferbaum, Shreyas Vasanawala, and Ralph Hurd. T(2) relaxation times of (13)C metabolites in a rat hepatocellular carcinoma model measured in vivo using (13)C-MRS of hyperpolarized [1-(13)C]pyruvate. *NMR in Biomedicine*, 23(4):414–423, May 2010.

[Zhao *et al.*, 1996] L Zhao, R Mulkern, CH Tseng, D Williamson, S Patz, R Kraft, RL Walsworth, FA Jolesz, and MS Albert. Gradient-Echo Imaging Considerations for

Hyperpolarized 129Xe MR. *Journal of magnetic resonance. Series B*, 113(2):179–183, November 1996.

[Zierhut *et al.*, 2010] ML Zierhut, YF Yen, AP Chen, R Bok, MJ Albers, V Zhang, J Tropp, I Park, DB Vigneron, and J Kurhanewicz. Kinetic modeling of hyperpolarized 13C1-pyruvate metabolism in normal rats and TRAMP mice. *Journal of Magnetic Resonance*, 202(1):85–92, 2010.

# Publishing Agreement

It is the policy of the University to encourage the distribution of all theses, dissertations, and manuscripts. Copies of all UCSF theses, dissertations, and manuscripts will be routed to the library via the Graduate Division. The library will make all theses, dissertations, and manuscripts accessible to the public and will preserve these to the best of their abilities, in perpetuity.

I hereby grant permission to the Graduate Division of the University of California, San Francisco to release copies of my thesis, dissertation, or manuscript to the Campus Library to provide access and preservation, in whole or in part, in perpetuity.

Bertram L. Koelsch

18. July 2014